Controlling CRUD Vapor Chimney Formation in LWRs Through Surface Modification

by

Leigh Lin

B.S. Nuclear, Plasma, and Radiological Engineering
University of Illinois at Urbana-Champaign, 2012

SUBMITTED TO THE DEPARTMENT OF NUCLEAR SCIENCE AND ENGINEERING IN PARTIAL FULFILLMENT OF THE REQUIREMENTS FOR THE DEGREE OF

MASTER OF SCIENCE IN NUCLEAR SCIENCE AND ENGINEERING
AT THE
MASSACHUSETTS INSTITUTE OF TECHNOLOGY

SEPTEMBER 2014

Signature redacted

Signature of Author: _____

Leigh Lin
Department of Nuclear Science and Engineering
August 21, 2014

Signature redacted

Certified by: _____

Michael P. Short
Assistant Professor, Nuclear Science and Engineering
Thesis Supervisor

Signature redacted

Certified by: _____

Jacopo Buongiorno
Associate Professor, Nuclear Science and Engineering
Thesis Reader

Signature redacted

Accepted by: _____

Mujid S. Kazimi
TEPCO Professor of Nuclear Engineering
Chair, Department Committee on Graduate Students

Controlling CRUD Vapor Chimney Formation in LWRs Through Surface Modification

by

Leigh Lin

Submitted to the Department of Nuclear Science and Engineering
on August 21, 2014, in Partial Fulfillment of the
Requirements for the Degree of Master of Science in
Nuclear Science and Engineering

Abstract

Fouling has been a persistent problem for fluid-solid interfaces, varying from heat exchangers to ship hulls. In nuclear power plants, buildup of CRUD can accelerate corrosion, increase pressure drops, cause axial power shifts, and increase radiation dose to workers. In this experiment, we studied the effect of induced microcavity and micropost patterns on CRUD morphology at atmospheric pressure. Samples with various pitches of microcavities and microposts were boiled in simulated PWR coolant. The effect of heat flux on CRUD formation was also examined.

The experiments support previous theories that subcooled nucleate boiling is enhanced at microcavities, and that CRUD deposition is promoted at those sites. A thin ring of particles, less than a micrometer in width, was seen around most microcavities even when the surrounding areas were crudded. However, some of the samples with microcavity pitches 50 μm and smaller experienced a pattern of clean and crudded areas, with the region around the microcavities free of CRUD more often than not. A theory is put forth that this is caused by interfering forces due to bubbles collapsing. The micropost samples showed substantial CRUD growth, particularly for the sample subjected to a high heat flux. The results of this experiment could have major implications for development of a self-cleaning material for heated surfaces.

Thesis Supervisor: Michael P. Short
Title: Assistant Professor, Nuclear Science and Engineering

Thesis Reader: Jacopo Buongiorno
Title: Associate Professor, Nuclear Science and Engineering

Acknowledgments

I wish to thank Professor Michael Short for being my advisor and providing me with vital insight and support I could not have done without. I have learned an incredible amount under his guidance in terms of both lab experience and life experience. I also wish to thank Professor Jacopo Buongiorno, whose expertise and feedback was crucial to this project's success.

I wish to acknowledge Ekaterina Paramonova and Gabrielle Ledoux, from whom I inherited this project. Without them taking the first steps into this experiment, I may not be here today.

Special thanks goes to Sangtae Kim, who prepared substrates for me over the entire year. Thanks also goes to Solomon Adera, who prepared the micropost substrates.

I would like to extend my gratitude and thanks to my colleague Pavlina Karafillis, without whose tireless help I would not have been able to work as efficiently or accomplish as much as I have. I owe special thanks to Vikash Mishra, who helped me greatly with data analysis and was always available for trading ideas. I am grateful to have been a part of the Short lab, which provided me with a great collaborative working environment, and would like to thank Daniel Schumaker in particular for his help.

I wish to thank my family and friends for their support in all that I do. I know I can count on them if I ever have any problems, large or small.

This work was performed in part at the Center for Nanoscale Systems (CNS), a member of the National Nanotechnology Infrastructure Network (NNIN), which is supported by the National Science Foundation under NSF award no. ECS-0335765. CNS is part of Harvard University.

Contents

List of Figures

List of Tables

List of Abbreviations and Symbols

Abbreviations

APS	Average Particle Size
BWR	Boiling Water Reactor
CHF	Critical Heat Flux
CIPS	CRUD-Induced Power Shift
CNS	Center for Nanoscale Systems
CRUD	Chalk River Unidentified Deposits
EDS	Energy Dispersive X-ray Analysis
EHT	Extra High Voltage
FAC	Flow-Assisted Corrosion
FESEM	Field Emission Scanning Electron Microscope
FIB	Focused Ion Beam
LWR	Light Water Reactor
MIT	Massachusetts Institute of Technology
ppm	parts per million
PWR	Pressurized Water Reactor
SEM	Scanning Electron Microscope
TC	Thermocouple

Symbols

a	particle radius
C_b	precursor conc. in fluid
C_bf	foulant conc. in the fluid
C_s	precursor conc. at the fluid/solid interface
C_{sf}	foulant conc. in the fluid/solid interface
d	distance
D	pipe diameter
e	electron charge
E	activation energy
F	shear stress
F_HYD	hydration force
F_L	lift force
h	surface-surface sep. between particles
J_t	mass flux of precursor
k_B	Boltzmann's constant
k_t	mass transfer coefficient for precursor
k_tf	mass transfer coefficient for foulant
K	hydrophobic repulsion force
l	pipe length
l_o	orientational correlation length
n_∞	ion density
R	universal gas constant
S	sticking probability
t	time
T	temperature
T_s	surface temperature
u	velocity
U_p	flow velocity at particle
v	friction velocity
v_min	saltation friction velocity
V_A	van der Waals force
V_R	electrostatic double-layer force
y_f	fouling deposit thickness
z	electron number
γ	reduced surface potential
κ	Debye-Huckel-reciprocal length
η	viscosity
ρ	fluid density
ρ_f	deposit density
τ	wall shear stress
ψ	potential

Chapter 1

Introduction

1.1 Effects of Fouling

Many systems with fluid-solid interfaces, both engineered and natural, persistently suffer from the effects of fouling. Fouling occurs when particles or microbes build up as solid or porous deposits in unwanted areas, causing problems by enhancing corrosion of the surface, increasing the pressure drop or completely blocking flow in the system, and affecting heat transfer. A study by Garrett-Price estimated that the overall cost of fouling for the US was $9 billion/year in 1985 dollars [1]. Van Nostrand, Leach, and Haluska performed a study on the economic impact of fouling in heat transfer equipment in refineries and estimated that the expenses from energy cost, production losses, and maintenance and cleaning costs was around $1,300 million/year in 1981 dollars [6].

The problems due to fouling can increase capital costs if components need to be made larger or more complex to offset deleterious effects. Sometimes backup components are desirable to keep the process on-line while parts are cleaned, and those increase the capital cost as well. Additional piping may be necessary if the component needs to be moved to a different location for easy access due to more frequent maintenance. Operating costs increase from needing more power to get the same quality product, should heat transfer or coolant flow be reduced by fouling. Maintenance costs also increase due to a higher replacement frequency of components and cleaning. Another major factor to consider is the loss of production when the process has to shut down for cleaning or replacement of fouled components, for example, when crude oil refineries must remove and replace a heat exchanger due to fouling. Much effort has been spent on finding ways to prevent fouling or mitigate the the effects of fouling and some remedial actions have been found to be cost-effective [1, 6].

In the nuclear industry in particular, a major concern has been the deposition of corrosion products on cladding surfaces, known as Chalk River Unidentified Deposits (CRUD) from its discovery in the Chalk River research reactor. These deposits are mainly made up of iron and nickel oxide particles about 0.1 to 2 μm in diameter [7, 8], carried by the coolant from the steam generator tubes, from other stainless steel reactor internals, or from the grid spacers holding the fuel rods in place [9, 10]. In pressurized water reactors (PWRs), most deposits are nickel ferrites ($Ni_xFe_{3-x}O_4$) with a small amount of cobalt, NiO, Ni metal, and some iron and nickel chromites ($FeCr_2O_4$, $NiCr_2O_4$, and $Ni_xFe_{1-x}Cr_2O_4$) [11]. In boiling water reactors (BWRs), the predominate form of the CRUD is hematite (Fe_2O_3) and non-stoichiometric nickel ferrite spinels [7]. Generally, the CRUD consists of an inner, tightly adherent layer that has relatively higher amounts of chromium from the base metal, and is depleted in iron and nickel. The outer layer is mostly nickel ferrite, which is more soluble and easily affected by chemistry variations (e.g., during shutdown) [11, 12, 8].

CRUD in reactors has been observed to grow as thick as 100 μm [13]. It can locally increase cladding temperatures, accelerate corrosion, and lead to undesired axial power shifts. Alternatively, CRUD deposits have the potential to increase heat transfer from the fuel cladding to the water coolant through enhanced boiling, under the right conditions. Increased heat transfer efficiency is desirable in nuclear reactors because it delays when the critical heat flux (CHF) occurs, thereby increasing the thermal margins and the safety of the reactor[14].

1.1.1 Fouling-Accelerated Corrosion

Fouling in systems can lead to or accelerate corrosion of the surface, resulting in failures of major equipment and components. Corrosion occurs when there is an electrochemical oxidation, and uniform corrosion tends to speed up with increasing temperature. When different metals are in solution, there is an exchange of electrons due to a difference in electrochemical potential. Corrosion and corrosion rates are also affected by heat flux, alloy impurities, solute size and composition, surface material microstructure, and fluid chemistry.

Fouling can enhance corrosion by increasing the surface temperature, due to additional thermal resistance, and by bringing together dissimilar materials [15]. Under certain conditions, some metal cations will undergo hydrolysis when in the presence of water, reducing pH locally, and resulting in an autocatalytic mechanism for local corrosion. Fouling can enhance pitting corrosion because corrosion deposits like cop-

per, iron, and nickel oxides are electrically conductive and serve as the cathode for the corrosion reaction. The fouling layer is rough, providing more bubble nucleation sites and a higher pressure drop as the fluid flows across it. This, combined with high temperatures, can increase cavitation, where bubbles collapsing on the surface erode it [5].

Increased corrosion due to fouling is a problem in chemical processing industries, particularly in welded areas; the oil and gas industry, where sulfate-reducing bacteria are a large problem; water treatment plants; and underground pipelines, which have to deal with decaying organic matter in the soil [5]. Biological fouling can increase corrosion by depleting oxygen at the surface and by producing carbon dioxide (which becomes carbonic acid), hydrogen sulfide, or other corrosive organic acids. Biofilms catalyze the reduction of oxygen, increasing corrosion potential. Macrofouling can create a differential aeration cell where there is free charge transfer, but limited mass transfer, causing polarization differences [5]. Sometimes the areas covered by microorganisms are actually more protected from corrosion by preventing oxygen from reaching the surface, though the exposed areas may then be in conditions that accelerate corrosion [16, 6].

In nuclear power plants, CRUD increases local temperature, thereby promoting local corrosion and can damage the fuel cladding to the point of rupture, releasing radioactive material into the coolant. The percentage of failures due to corrosion from CRUD in PWRs is low, but CRUD induced localized corrosion (CILC) was a major cause of fuel failures in BWRs [9]. This was, in part, due to the copper present in the brass condenser tubes in BWRs, which resulted in a dense, tightly adherent CRUD, as well as vapor chimneys being blocked by high amounts of copper and zinc in the coolant. There were especially high failure rates in 1998 and 2003 from corrosion and CRUD, accounting for as much as 45% of the total fuel failures in BWRs. Since limiting the amount of copper concentration, heat treating the cladding for better corrosion resistance, and through careful water chemistry monitoring, there have been no further failures from CILC. In comparison, the corrosion in PWRs is more uniform and CILC is less of a problem [9].

1.1.2 Blockage

Buildup of deposits in systems can increase the pressure drop in the system or result in a complete blockage of passageways in the most severe cases (see Figure 1-1). Fouling layers decrease the available surface area for flow and also tend to be rougher

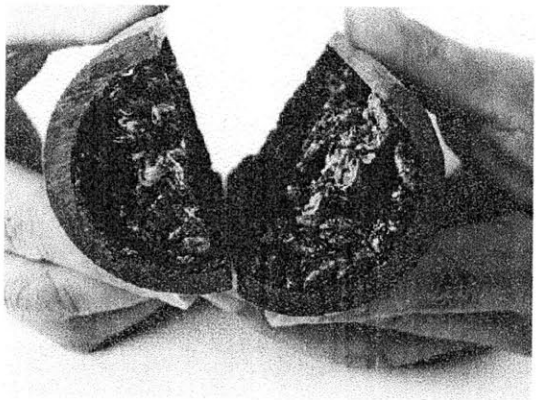

(a) Zebra mussels completely clogging a pipe [17].

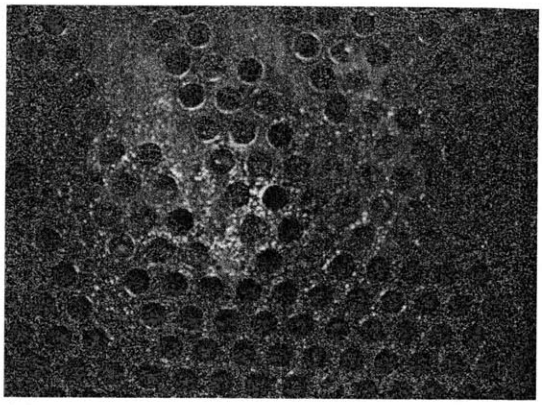

(b) Calcium carbonate deposits in condenser tubes at South Texas Project nuclear power plant [18].

Figure 1-1: Blockage due to fouling.

than the clean surface, both of which contribute to an increased pressure drop [6]. Systems that need a certain fluid flow need to make up for this pressure drop by increasing the pumping power, which costs energy and money. If the fouling layer is not removed, fluid flow could ultimately be completely blocked.

Some PWR plants suffered a pressure drop in the secondary-side steam generator that resulted in a 4-5% reduction in electrical generating capacity. San Onofre Unit 2 experienced a cumulative pressure drop of 0.41 MPa due to fouling in the 1990's until chemical cleaning of the steam generators took place. The average CRUD thickness was approximately 0.25 mm before cleaning [19]. In one plant with air inleakage, heavy CRUD deposition increased the differential pressure in the core by 15% [11]. Macbeth performed experiments on pressure drop due to CRUD buildup using an annular test section with water at 69 bar (6.9 MPa). He found a frictional pressure drop of 0.46-1.72 bar (0.046-0.172 MPa) for CRUD thicknesses of 30-150 μm [20].

1.1.3 Heat Transfer

Heat transfer is a major element in power generation and many chemical and manufacturing processes. A thick layer of deposits adds thermal resistance to the system, increasing local temperatures and reducing the efficiency of the system. The fouling layer usually has a lower thermal conductivity than the surface material. Table1.1 lists some thermal conductivites for CRUD and common construction materials found in PWRs and BWRs. In the past, boilers have exploded due to scaling reducing the

Material	Thermal Conductivity (W/m-K)	Ref.
CRUD	1.2-4.5	[21, 22, 23]
CRUD with 66.6% porosity[1]	0.7-0.9	[21, 22, 24]
Alloy 600	15-19[2]	[25, 26]
Alloy 690	13.5-17.3[2]	[25, 26]
Alloy 800	11.5-16.3[2]	[25, 26]
Stainless Steel 304 and 316	15-16	[27, 28]

[1]This is the effective thermal conductivity.

[2]Lower value is at 20°C and higher value is at 300 °C.

Table 1.1: Thermal conductivites for base metals and fouling deposits in LWRs.

heat transfer coefficient and leading to overheating, but pressure vessel codes have since been implemented to prevent this [6].

The presence of a thick CRUD layer can increase temperature gradients, but if it is porous and thin enough (less than 20-30 μm), its thermal resistance will be negligible, and it may actually improve heat transfer and delay CHF [14, 22, 29]. The liquid in the CRUD layer experiences higher temperatures and can evaporate before the bulk coolant temperature reaches its boiling point. If vapor chimneys are present in the CRUD layer, the vapor can escape through these channels. There have been several studies and models developed on enhanced heat transfer through the wick boiling phenomenon [22, 30, 13].

One of the most efficient modes of heat transfer is through subcooled nucleate boiling, before the critical heat flux (CHF) is reached. The onset of nucleate boiling (ONB) for water at atmospheric pressure occurs around a heat flux of 10^4 W/m^2 and the CHF occurs at 2×10^6 W/m^2 for pool boiling [31]. Thermal power plants would ideally operate as close to the CHF as possible to transfer the maximum amount of heat, but there are safety margins imposed to ensure the plant stays below the CHF. In PWRs, the departure from nucleate boiling ratio is required to be greater than 1.3, and in BWRs, the critical power ratio must be greater than 1.2 in the US. Dryout is more significant if thick CRUD is present since CRUD has a lower thermal conductivity than the cladding. Under PWR conditions, a CRUD thickness greater than 75 microns is in danger of dryout [29].

1.2 Research Objectives

The objective of this thesis is to evaluate the effect of induced microcavities and induced microposts on the formation of vapor chimneys in the CRUD layer. The bulk of the silicon substrate surfaces were lithographically etched with regular arrays of micrometer-sized holes, and a couple of the silicon substrates had micropillars deposited on them. The pitches between the microcavities and microposts were varied to determine what role, if any, the density of these sites have on CRUD formation and chimney density in a heated system. Besides pitch, nickel oxide and iron oxide concentrations were changed and boiling time was changed to see their effects on CRUD growth. Fouling has been identified as one of the major problems in heat exchangers and other systems for a long time, but still remains a problem today. If introducing defects, like microcavities, onto a surface is shown to promote boiling chimney formation, it will have important implications on controlling the formation of fouling layers and enhancing heat transfer efficiency.

1.3 Sections

Chapter 2 presents background information on the problems that arise from fouling, the types of fouling, and some of the potential solutions to prevent or mitigate fouling and its effects. The forces behind fouling and the effects of fluid velocity, heat flux, and coolant chemistry on fouling rate are described. Various types of fouling are discussed, including crystallization, particulate, biological, chemical, and corrosion fouling. Different models of fouling are covered and fouling in both heated and unheated systems are discussed, with a focus on CRUD in nuclear power plants. Prevention of fouling, through elimination of its percursors or inhibiting adhesion of the precursors to the surface, is discussed. Mitigating the detrimental effects of fouling is covered, including methods to remove the fouling layer, reduce corrosion, and counteract decreased heat transfer and pressure drop.

Chapter 3 describes the experimental methods for preparing the samples, the experimental setup, the procedure for artificially growing CRUD, and the tools and methods for analyzing the samples. The microfabrication process for preparing the grid of microcavities or microposts on the surface of silicon substrates is explained. A description of the boiling facility, electronic controls, and data logging system is given. The tools used for analysis are briefly described, which include the scanning electron microscope (SEM) and the focused ion beam (FIB). Lastly, the methods of

analyzing the effect of microcavities on the fouling layer are presented.

Chapter 4 contains the results of the experiment. SEM images of samples with induced microcavities and microposts both before and after CRUD growth are shown. Runs with different parameters, including defect pitch, particle concentration in the coolant, and boiling time, are presented for comparison. Elemental Dispersive X-ray Analysis (EDS) results are shown alongside the SEM images. A cross-sectional view of samples that were milled using the FIB is also presented.

Chapter 5 discusses the results of the surface texturing on the formation of vapor chimneys on the substrates. The amount of CRUD deposition depending on microcavity pitch and micropost height and pitch is discussed in terms of the results seen using the SEM and FIB. The role of heat flux on boiling and vapor chimney formation are be discussed. The limitations of this experiment and potential improvements to the process are given. The effect these results have on nuclear reactor performance is also examined.

Chapter 6 contains a brief summary and the conclusions of the study. The key findings from this experiment are reviewed. Future work for evaluating and optimizing surface texturing for anti-fouling purposes in nuclear reactors are also considered. Further testing and changes in test conditions for examining vapor chimney formation and CRUD growth are discussed.

Chapter 2

Background

2.1 Occurrence of Fouling

Fouling occurs when particles or microorganisms are carried to the surface and then accumulate or adhere to the surface. The adhesion of particles depends on London-van der Waals forces, electrostatic forces, and contact area. Other factors affecting the deposition of particles are particle sizes and amounts, pH, gravitational forces, hydrodynamic interactions, surface hydration and reactions, fluid velocity, and heat flux.

The mass flux of a foulant precursor J_t (in units of kg/m^2/s) to the surface is given by [6]:

$$J_t = k_t (C_b - C_s) \tag{2.1}$$

where k_t is the mass transfer coefficient for the foulant precursor, C_b is the concentration of the precursor in the fluid, and C_s is the concentration of the precursor at the fluid/solid interface. The mass flux of the foulant back to the fluid is [6]:

$$J_f = k_{tf} (C_{sf} - C_{bf}) \tag{2.2}$$

where k_{tf} is the mass transfer coefficient for foulant convection, C_{sf} is the concentration of the foulant in the fluid, and C_{bf} is the concentration of the foulant in the fluid. The complete mass transfer of the foulant $\frac{dy_f}{dt}$ (in units of m/s) is given by [6]:

$$\frac{dy_f}{dt} = \frac{(J_t - J_f)}{\rho_f} \tag{2.3}$$

where ρ_f is the deposit density.

The fouling layer tends to increase with increasing flow rate for laminar flow since more particles are transported to the surface, but decreases when there is turbulent flow. Studies have shown that turbulent flow, which results in non-uniform shear stresses at the surface, is better at removing fouling layers than uniform flow [32]. Rougher surfaces experience more fouling due to increased turbulence near the fluid/solid interface, but also due to more surface area being available for bonding and foulants in valleys being harder to remove [33, 34]. The ratio of adhesion to shear stress can be represented by the sticking probability S [6]:

$$S = \frac{\exp\left(-E/RT_s\right)}{\left(v/v_{min}\right)^2} \tag{2.4}$$

where E is the activation energy, R is the universal gas constant, T_s is the surface temperature, v is the friction velocity, and v_{min} is the saltation friction velocity. The saltation velocity is the minimum velocity needed to maintain particle flow, just before the particles begin to fall out of suspension [35]. The shear stress F on the wall of a pipe is given by [1]:

$$F = \tau \pi D l \tag{2.5}$$

where τ is the wall shear stress per unit length, D is the pipe diameter, and l is the length of the pipe.

Repulsive van der Waals and electrostatic double-layer forces limit deposition and can be controlled, to some extent, through the choice of fluid, use of surface coatings, or by increasing the pH [7, 36, 1]. The van der Waals interaction force V_A between two spherical particles is [37, 38]:

$$V_A(d) = -\frac{A_H}{6}\left[\frac{2a^2}{d^2+4ad} + \frac{2a^2}{(d+2a^2)} + \ln\left(1 - \frac{4a^2}{(d+2a)^2}\right)\right] \tag{2.6}$$

where d is the interparticle distance and a is the particle radius. The Hamaker constant A_H is a material property that describes the forces between bodies. A material that is more electron-dense has a higher Hamaker constant [6]. The van der Waals forces between a spherical particle and a plane is [37, 38]:

$$V_A(d) = -\frac{A_H}{6}\left[\frac{a}{d} + \frac{a}{d+2a} + ln\left(\frac{d}{d+a}\right)\right] \tag{2.7}$$

Materials in aqueous solutions become charged due to dissociation of molecules or preferential adsorption of ions [1]. When two identical particles approach each other, they repel each other due to their surface charges. The electrostatic double-layer force

V_R is given by [39, 37]:

$$V_R = \frac{128\pi a_1 a_2 n_\infty k_B T}{(a_1 + a_2)\kappa^2}\gamma_1\gamma_2 \exp(-\kappa h) \tag{2.8}$$

where a_1 and a_2 are the radii of the first and second particle, n_∞ is the ion density in the bulk coolant, k_B is Boltzmann's constant, T is the absolute temperature, and h is the surface-surface separation between particles. The Debye-Huckel-reciprocal length κ is the inverse length of the range of influence of the ion atmosphere. The reduced surface potentials, denoted as γ_1 and γ_2, is defined by [39, 37]:

$$\gamma = \tanh\left(\frac{ze\psi}{4\kappa T}\right) \tag{2.9}$$

where z is the electron number, e is the electron charge, and ψ is the potential.

Hydration forces F_{HYD} also effect the attraction or repulsion between particles and surfaces, given by the following [40, 37]:

$$F_{HYD}(d) = K\exp\left(-\frac{d}{l_o}\right) \tag{2.10}$$

where $K > 0$ are hydrophilic repulsion forces and $K<0$ are hydrophobic attraction forces, d is the separation distance, and l_o is the orientational correlation length of water molecules (which describes how many of the molecules nearby have the same orientation due to intermolecular forces). Hydrophilic surfaces enhances rewetting of the surface and tends to increase adhesion of species to the surface whereas hydrophobic surfaces decreases wettability [33]. Greater contact area also increases the adhesion probability of particles.

Surface reactions can also be suppressed through changing the pH, temperature, or fluid velocity. If heat flux is increased so that boiling occurs, deposition increases as precipitates concentrate at the edges of the bubbles (see Figure 2-1). The amount of foulant deposited, in most cases, increases as pH decreases and as heat flux increases due to higher dissolution rates and higher solubility limits. Figure 2-2 shows a pH-potential diagram for iron. As can be seen from the figure, at a lower pH, iron is more likely to be an anion. On the other hand, under basic conditions, iron is more likely to precipitate out as an oxide.

Fluid flow exerts a lift force F_L on particles perpendicular to the flow direction which can be calculated in the following way [41]:

$$F_L = 1.615\eta d_p^2\left(\frac{\rho}{\eta}\frac{\partial u}{\partial y}\right)^{1/2} U_p \tag{2.11}$$

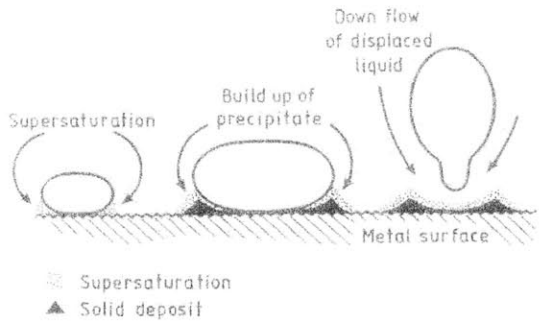

Figure 2-1: Deposition under bubble [1].

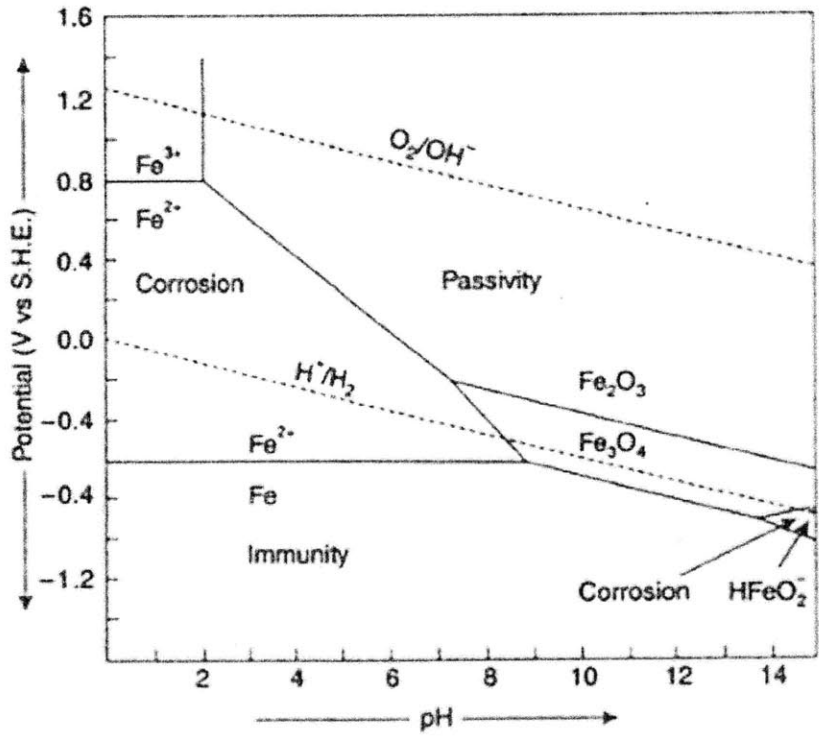

Figure 2-2: Simplified Pourbaix Diagram for iron in solution at 25 °C [2]. Iron tends to be in solution as anions naturally below a pH of 6-7. At a higher pH, iron oxides are the most stable form.

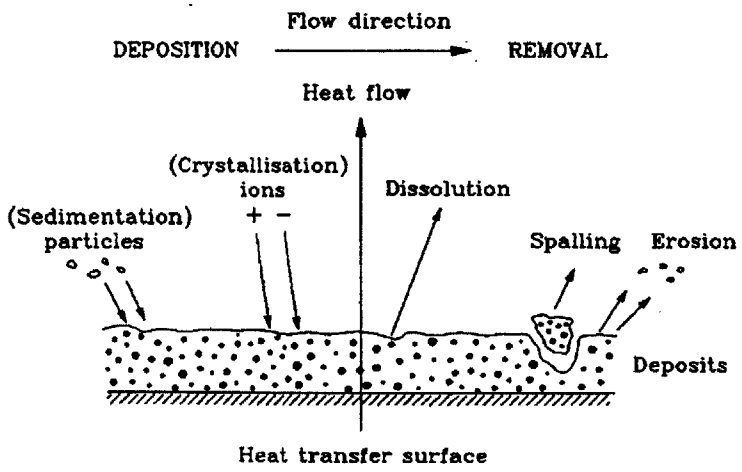

Figure 2-3: Various fouling deposition and removal mechanisms [3].

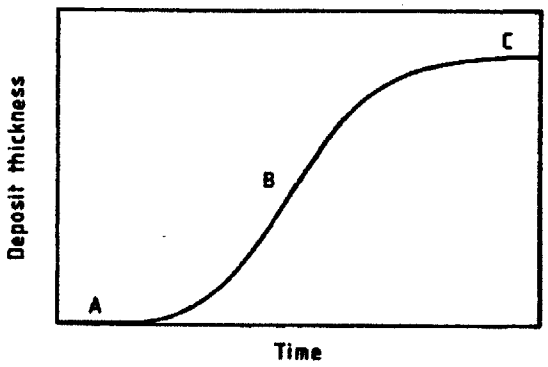

Figure 2-4: Deposit thickness over time [3].

where η is the viscosity, d_p is the particle diameter, ρ is the fluid density, $\frac{\partial u}{\partial y}$ is the velocity gradient in the y-direction, and U_p is the flow velocity at the particle location. As can be seen, increasing fluid velocity increases the lift force. The particle will be removed from the surface if the lift force is greater than the sum of the adhesive van der Waals force and gravity force, assuming the particle has not bonded with material on the surface. The deposition and removal process during fouling is shown in Figure 2-3 .

Fouling thickness with time follows an S-curve. There is an induction period before deposition occurs, and deposit thickness increases until equilibrium between the deposition and removal rate is reached (see Figure 2-4). Studies have shown that fouling can occur fairly rapidly. One shell and tube oil heater reported a heat transfer coefficient decrease of 40% in just 3 months [6]. A typical oil refinery preheater chain

was found to have a 42% drop in heat transfer after a year, though using antifoulants decreased this to 18% [6]. Depending on the environment in which the fouling layer occurs and the participating species, it can be tenacious or flaky, dense or sparse, with varying colors and thicknesses.

2.1.1 Types of Fouling

Fouling can be categorized into five types: crystallization, particulate, biological, chemical, and corrosion fouling.

- **Crystallization fouling**, which includes precipitation and solidification, is from deposition or formation of small particles on the surface that grow into crystal structures, many times from heating or freezing of fluid on the surface (see Figure 2-3). CRUD growth in nuclear reactors is a form of precipitation fouling. Crystallization fouling is affected by the amount of nuclei, impurities, solubility limit, how quickly solution is cooled, and if phase changes are present. Cooling quickly results in smaller crystals. On heated surfaces, it was seen that when boiling occurs, rings of particles are deposited. One theory is that when the water evaporates and the bubble grows, the particles are left behind at the bubble's edges [42, 43].

- **Particulate fouling** is the accumulation of particles on a surface. The main transport mechanisms for deposition are diffusion, inertial impaction, and gravitational settling. Heavier particles will settle onto horizontal surfaces from gravity, and finer particles will stick to inclined surfaces due to suction. A common problem is with gas-side fouling present in dryers, gas lines, reactors, combustion systems, and heat exchangers [6].

- **Biological fouling** is the growth of organisms, including animals, plants, bacteria, etc., on surfaces. Fluid flow brings nutrients to surfaces where they can accumulate, and organisms that can attach to the surface will be close to a food source. In addition to the effects of physical transport and physicochemical interactions that are a part of deposition of other types of fouling, biological rate processes also affect the accumulation of biofilms on surfaces [6].

- **Chemical reaction fouling** is when the fouling layer is a result of chemical reactions in the fluid. Electrochemical reactions take place where metal atoms become ions in solution, and the surface is left with excess electrons. An ex-

ample of chemical fouling is coke formation in coal plants, autoxidation, and polymerization [6].

- **Corrosion fouling** occurs when the surface itself suffers corrodes and those particles form the fouling layer. Often the most important parameter for corrosion rates is the amount of oxygen available since it is usually the cathodic reactant. In most cases, more oxygen means more corrosion. However, sometimes passivating oxide layers are formed, impeding further corrosion of the surface. If the passivating layer is weakly adhered to the surface though, layers that form can be torn off through shear forces, continuously exposing the surface to further corrosion. Even for tightly adherent passivating layers, if the oxide cracks, such as through mechanical forces or thermal expansion, the exposed surface will experience corrosion again. Corrosive salts such as chlorides and sulfates can prevent the development of protective layers so that corrosion of the surface continues uninhibited [6].

In many situations, there are several mechanisms that contribute to fouling and not just one. For example, industrial heat exchangers usually experience particulate, corrosion, and biological or chemical reaction fouling. Wastewater treatment and desalination systems usually experience both inorganic and biological fouling [1, 6, 36, 33].

2.1.2 Fouling in Nuclear Power Plants

Some studies on CRUD from nuclear reactors have described it has having an inner layer that is adherent and dense, while the outer layer is looser and more porous. In BWRs, the main phases of CRUD are hematite and non-stoichiometric nickel ferrite spinels. In PWRs, CRUD is mainly made up of nickel ferrite, nickel metal, or nickel oxide [7]. The upper regions of PWR fuel rods tend to have thicker CRUD, unlike in BWRs, since this is where subcooled nucleate boiling is more likely to occur. The boric acid and lithium hydroxide in the coolant can also build up in the pores of the CRUD layer, precipitating out as $LiBO_2$, $Li_2B_4O_7$, Ni_2FeBO_5, and other similar forms [44, 10]. This leads to the CIPS phenomenon in PWRs, mentioned in the previous section. Prevention and mitigation techniques for CRUD will be covered later.

CRUD on fuel rods are found to be reddish, grey, or black in color in current LWRs. The red color comes from Fe_2O_3, whereas Fe_3O_4 and nickel ferrite is black. The fuel rods can also look grey or white from the presence of zirconium oxide [45]. The thickness of the CRUD layer can vary from very thin to over 100 μm after one

Property	Typical Values	References
Average CRUD thickness (μm)	20-60	[4, 22, 13, 47]
CRUD porosity (%)	30-80	[4, 22, 13]
Pore size (μm)	0.1-0.5	[4]
Chimney density (chimneys/mm^2)	3000-5000	[4, 13]
Chimney diameter (μm)	2.5-5	[4, 13, 48]

Table 2.1: General charactersitics of CRUD and vapor chimneys under sub-cooled boiling conditions.

reactor cycle [7, 46]. The thermal properties of the CRUD depend on its thickness, density, porosity, and the size, shape, and density of vapor chimneys [14]. Vapor chimneys are tunnels that go through, or partway through, the CRUD layer. The liquid in the CRUD layer will experience high temperatures and evaporate, and the vapor can then exit from the chimneys, taking heat away from the surface of the cladding. Table 2.1 lists general characteristics of CRUD.

Bubble nucleation sites are more likely to occur when the surface has a lot of microcavities [14, 49, 50]. A larger cavity radius lowers required superheat for nucleation, though only a certain range of sizes will be active nucleation sites. Bubble size depends on the balance between buoyancy, surface tension, and inertial forces. For a constant superheat, increasing cavity diameter increases the bubble departure diameter. With a higher superheat, the bubble departure frequency increases [51]. A study by Shi, Jones, and Pan found that there is an optimum CRUD porosity, particle diameter, chimney density and radius for increasing CHF. A porous CRUD with high chimney population density or larger chimney radii will have a lower wall superheat in most cases, though this reduction is not as significant as the increase in CHF [52].

Hysteresis is an important factor to where boiling occurs when increasing or decreasing heat flux. When increasing the wall superheat, heat flux increases along a certain curve up to the CHF, but does not follow the same curve down [53]. This is due to some nucleation sites, once initiated, staying active even after the wall superheat has decreased below the temperature required for initiating subcooled boiling. Subcooled boiling is enhanced in high duty cores, which have higher coolant temperatures and surface heat fluxes, and in turn promotes bubble nucleation. Due to power uprates in reactors, CRUD growth is becoming more of a problem in these nuclear plants. In addition, the change to longer cycle lengths means more CRUD can build up, and more boron compounds will deposit in them due to the higher boron concentraions needed at the beginning of the cycle [42].

In addition to increasing corrosion rate, pressure drop, and thermal resistance, fouling in nuclear power plants can negatively affect production and safety. In PWRs, CRUD tends to form near the top of the fuel rods where nucleate boiling occurs [7, 9]. Since PWR coolant has boric acid and lithium hydroxide added to it, some boron compounds precipitates out of the coolant and stay in the pores of the CRUD layer, mostly in the form of lithium tetraborate ($Li_2B_4O_7$). Boron is a neutron poison, and it acts to depress the power at the top of the core for most of the cycle where CRUD tends to grow. This leads to what is known as CRUD induced power shift (CIPS), or axial offset anomaly. CIPS is usually defined as when the axial power distribution varies by more than 3% from expected values, and is observed when the CRUD is 20 μm thick or more [42, 44].

Enough CRUD can be present for CIPS to occur as soon as 4 months into the cycle. When CIPS occurs, the plant may have to operate at lower power to provide extra shutdown margin, which decreases the efficiency of the plant. CIPS effects shutdown margin because the boron deposits at the top of the core burns at a slower rate than then bottom of the core. The axial offset at the end of the cycle will actually shift upwards since there is more unburned fuel near the top of the fuel rods. Therefore, during operations, the control rods (which come down from the top in PWRs) have less worth near the top of the core than anticipated because of the smaller neutron population there. If the reactor is brought up to full power from zero power with crudded fuel assemblies, the control rod worth is higher due to the top of the fuel rods having more fissionable material left. This also makes criticality calculations more difficult [42]. In one plant, CRUD shifted the power distribution downward and radially inward near the top of the core with a 0.45% loss in reactivity and increased the axial peaking factor by 10% [11]. In Cycle 9 of the Callaway plant, the power was reduced to 70% due to CIPS for the last third of the cycle [42, 54].

An additionals problem is that CRUD particles that deposit on cladding surfaces become activated over time. When part of these activated products redeposit on other surfaces in the system that workers access during maintenance, personnel can become exposed to higher radiation fields than expected. Cobalt-60 is the main activated product of interest in Light Water Reactors (LWRs) and has a relatively long half-life. There are also minor contributions to worker dose from cobalt-58 (an important short-term source), manganese-54, and zinc-65 [55, 11].

2.1.3 Fouling of Other Heated Surfaces

Fouling is also a large problem in other combustion systems, chemical and refining operations, and food processing. In 1987, a survey by EPRI found that 37% of US coal utilities had frequent fouling and 77% had occasional to frequent problems [56]. Fouling in coal plants cause losses in efficiency in the furnace, economizer, superheater, and reheaters. In addition, steam temperatures are harder to control with furnace slagging.

Geothermal plants suffer from crytallization fouling as after water flashes to steam, the residue water has a high concentration of dissolved salts. When extracting the remaining energy, the heat recovery system experiences fouling problems. Many chemical processes use catalysts to speed up reactions, but these can become deactivated due to fouling. This occurs when catalysts suffer from site blockage, mainly caused by carbon [6].

In the food and beverage industry, fouling problems occur from protein deposition in heat exchangers, biofilm growth on surfaces, ice buildup in freezers, accumulation of material in low-velocity areas, etc. and lead to increased matinenance and fuel cost as well as lower quality products or production losses. Some processes depend on heat transfer, such as boiling, sterilizng, and cooking food. Fouling is especially problematic for thermosensitive compounds, such as milk products [36, 6].

2.1.4 Fouling of Non-heated Surfaces

Fouling can occur in systems without any applied heat as well. The growth of animals and plants (e.g., barnacles, tube worms, tunicates, hydroids, bryozoan, mussels, algae) on submerged objects decreases the efficiency of propulsion on ships, can lead to failure of flying boats to get off the water, reduces the efficacy of underwater acoustic devices, and destroys corrosion-resistant coatings. Fouling of ships is mainly dependent on how much time in spent in port since many fouling organisms have a harder time attaching to the surface when water is moving across the surface at higher velocities. Microbial growth also depends on the water temperature, being most prominent when the water temperature is 70-100 °F, and nonexistent above 150 °F or below 60 °F. Sound equipment can experience decreased transmission due to reflection, scattering, and absorption from fouling, and background noise can be larger due to cavitation. Fouling of salt water pipe systems (e.g., fire mains) interferes with flow, and are difficult to break down for cleaning [16].

Cooling water systems also suffer from biological, particle, and corrosion fouling.

Unless the water is purified, scale deposits can be left behind when the water evaporates. Pressure-driven membrane processes are used in many water treatment plants where natural organic matter is the main foulant, and is also used in biotechnology, medicine, and food industries where proteins are the main foulant. Techniques using reverse osmosis, nanofiltration, ultrafiltration, or microfiltration suffer from deposits left behind as the liquor moves through the membranes. Fouling of membranes not only decreases the fluid flux due to hydraulic resistance, but may also suffer from concentration polarization inside the foulant layer that further contributes to flux loss [37, 57, 58]. Some systems suffer from solidification fouling, such as ice in freezers or wax hydrocarbons in the oil industry that deposit on cool surfaces when they are being transported through pipelines. Fouling is an important problem in boiling cryogenic fluids, such as liquid hydrogen, helium, nitrogen, or argon. For cooling superconducting magnets, very small deposits can greatly reduce heat transfer and can lead to burnout [6].

2.2 Fouling Models

The models here focus on precipitation fouling, which is the main type of fouling in heat exchangers. There are two main drivers of deposition: degree of supersaturation and mass diffusion. The removal rate is dependent on the fluid flow. Fouling models dependent on supersaturation by Kern and Seaton, and Ebert and Panchal to calculate the thermal resistance, which is proportional to fouling layer thickness, are in the following form [59]:

$$\frac{dR_f}{dt} = \alpha \left(C_{sup} - C_{sat}\right) - \gamma \tau R_f \tag{2.12}$$

where R_f fouling resistance, α is the deposition constant, C_{sup} is the supersaturated concentration of the fluid, C_{sat} is the saturated concentration of the fluid, γ is the removal constant, and τ is the shear stress. Models that were dependent on mass diffusion used a similar equation:

$$\frac{dR_f}{dt} = \alpha \left(C_b - C_s\right) - \gamma \tau R_f \tag{2.13}$$

where C_b is the saturated concentration in the bulk fluid and C_s is the saturated concentration at the surface. For chemical reaction fouling, the $(C_{sup} - C_{sat})$ can be replaced with the Arrhenius relationship $\exp\left(-E/RT\right)$ [60].

For nuclear reactors, many studies have examined CRUD growth through sim-

ulating thermal hydraulic and chemistry conditions. The CRUD Chemistry Model proposed by Dickinson et al. combined wick boiling, radiolysis of water, nickel and iron dissolution and hydrolysis, and boric acid chemistry to predict the heat flux, fluid flow, and chemical reactions in the CRUD layer in PWRs. The model found that at a CRUD thickness of 10-20 μm, lithium metaborate begins to precipitates out, which also lowers the pH and results in formation of zircaloy oxides. The CRUD was rich in NiO due to conditions that allow for nickel release from steam generator tubing [61].

Wang proposed a four-regime model for conditions in CRUD. The flooding model simulated the conditions of liquid filling CRUD chimneys and pores, which is present at low power conditions. The mixture model assumed vapor and liquid mixing in CRUD chimneys and pores, which is what occurs during normal operating conditions in a nuclear reactor. The third regime is the dryout model, which simulates conditions at high power when the CHF is reached. Lastly, the particle model is for CRUD pores that are filled with solid particles, which may occur due to significant impurities in the reactor coolant system [29].

Due to the importance of fouling on heat transfer in nuclear power plants, several models have focused on boiling conditions in the CRUD layer. Studies by Cohen and by Macbeth suggested that wick boiling is the primary mechanism of heat transfer through porous media after noticing that the temperature difference across the CRUD layer was smaller than expected. Wick boiling occurs when liquid is brought to the heated surface through feed capillaries where they evaporate close to the lower part of the chimney, and the vapor then escapes through the chimney (see Figure 2-5). If the material (CRUD in this case) is not constrained, the boiling process will arrange vapour escape channels itself. Macbeth found that dryout values with CRUD is 5-10% lower than on clean surfaces, perhaps due to the continuous liquid film being interrupted by vapor emission through the chimneys [4].

Models of CRUD in PWRs using MAMBA-BDM by Short et al. indicated that the temperature distribution is lower at the chimneys due to wick boiling, and peaks away from the chimney. The study also found that as the pitch between vapor chimneys decreased, fluid convection became increasingly important since it contributes to heat transfer more than the conduction term. A vapor chimney pitch of 5 μm gives a reduction of 2 K in peak cladding temperature, which is estimated to reduce corrosion rate by 10-15% [62].

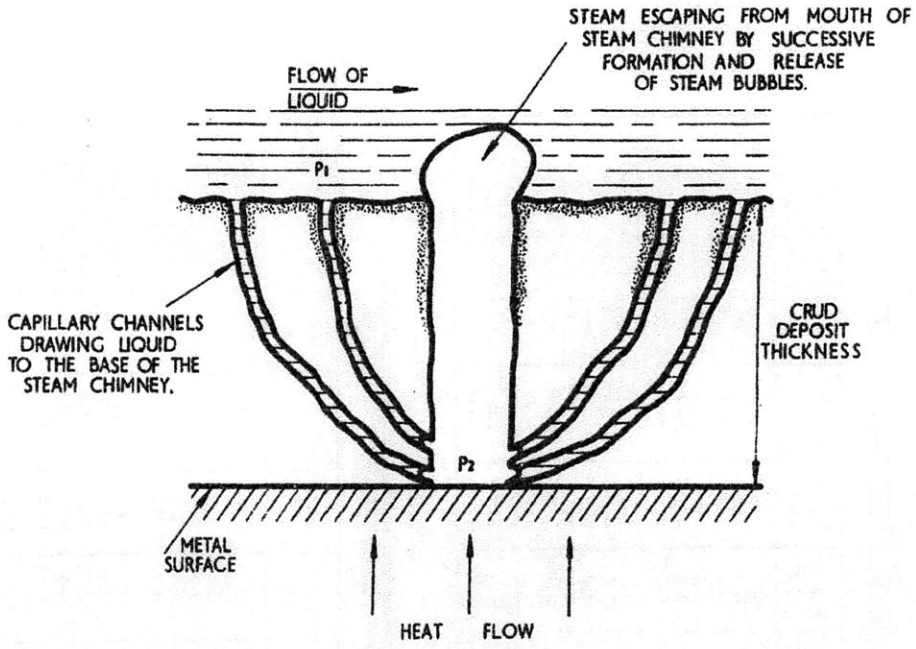

FIG. 1 PROPOSED MODEL OF 'WICK BOILING' IN A MAGNETITE CRUD DEPOSIT.

Figure 2-5: Wick boiling phenomena in CRUD layer [4].

2.3 Prevention and Mitigation

There are several methods to prevent or mitigate the negative effects of fouling. One approach is to control the operating conditions of the system to limit foulant precursors, such as by preventing corrosion. The second is to choose conditions and materials that make it difficult for particles to deposit on surfaces. The third approach is to remove the fouling layer after it has deposited, such as through regular cleaning using chemical or mechanical methods. Choosing construction materials that are resistant to fouling, corrosion-resistant, or will make up for the corrosion and thermal resistance of the layer of deposits can prevent or mitigate the negative effects. Alternatively, rather than changing the bulk material, a coating can be applied to the surface that is resistant to corrosion or adhesion. Another method, which is the focus of this thesis, is on physically modifying the surface geometry of the material to decrease or change the growth of the fouling layer.

2.3.1 Fouling Mitigation by Controlling Operating Conditions

2.3.1.1 Controlling Fluid Chemistry

One of the most important factors of how the fouling layer forms is the fluid chemistry. Higher pH has been found to result in less deposition due to the stable passivating oxide layer that forms on the surface [11]. The amount of hydrogen and oxygen in the coolant has a large effect on fouling and is closely related to the pH. For example, high levels of oxygen in the water promotes corrosion of surfaces unless a tenacious passivating oxide layer forms.

Another form of chemistry control is to add antifoulants to the fluid to decrease fouling of surfaces. Different types of antifoulants are shown in Table 2.2. An example of commonly used antifoulants are oxidizing biocides, such as chlorine, sodium hypochlorite, and ozone, which are effective in preventing biological fouling. Adding impurities can also retard fouling in one of two ways: 1) if they are adsorbed onto the crystal surface, they can prevent further growth at that location or, 2) if they remain in solution, impurities can impede crystallizing species from getting to the surface [6]. Suspended particles can either promote or retard fouling depending on whether they have a scrubbing effect or act as nucleation sites for crystallization. If the concentration of metallic ions is increased, the deposition will generally increase due to there being more particles available for deposition.

In the nuclear industry, many plants now inject zinc, limited to 6 ppb, into their

Anitfoulant	Description	Example
Dispersant	prevents agglomeration and encourages disintegration	sodium stearate used in soap
Corrosion inhibitor	usually film-forming compounds that decreases the corrosion rate of a material	hydrazine used in power plants
Metal chelate	deactivates metal ions, which could otherwise lead to polymerization	citric acid used in boilers
Antioxidant	reacts with free radicals and prevents autoxidation	N,N'-Di-sec-butyl-benzene-1,4-diamine used in oils
Detergent	encourages mixing of compounds with the fluid, similar to dispersnats but more polar	alkylbenzenesulfonates used in laundry detergent
Neutralizer	undergoes chemical reactions with fouling precursors	methoxypropylamine used in petrochemicals
Biocide	protects against biological growth by rendering organisms harmless chemically or biologically	sodium dichloro-s-triazinetrione used in water purification filters

Table 2.2: Antifoulant descriptions and examples of their use.

coolant, resulting in as much as a five times decrease in corrosion products. Zinc reduces corrosion by forming a protective oxide film on the steam generator tubes, especially for those made of alloy 600 [44, 11]. The corrosion film preferentially forms with the zinc, forming a denser, more adherent, and thinner corrosion scale. $ZnCr_2O_4$ and $Zn(Fe_xCr_{1-x})_2O_4$ are more stable than the other iron and nickel oxides, decreasing the thickness of those oxide films. Zinc injection can decrease corrosion rates for alloy 600, alloy 690, and stainless steels (typical LWR construction materials) from around 1 mg/dm^2/month to around 0.1-0.3 mg/dm^2/month. Zinc also replaces cobalt in oxides on surfaces, which could decrease the worker dose by 10-15% [12].

In PWRs, boric acid (H_3BO_3) is used as a neutron poison to control reactivity, and lithium hydroxide (LiOH) is added to lower the acidity of the water. Typical boric acid concentrations are 1400-1800 ppm at the beginning of the fuel cycle, with recent increases due to increased cycle length. Lithium concentrations of 2.2-3.5 ppm (increased from past concentrations due to increased boron) on startup [11, 9]. EPRI's PWR Primary Water Chemistry Guidelines recommend that a minimum pH of 6.9 be maintained, and also has guidelines for chemistry control during startup and shutdown operations [11]. Adding more lithium hydroxide to reactor coolant

increases the pH, which decreases the corrosion deposits solubility. This is both a benefit and a drawback: higher solubility increases the amount of corrosion particles in the coolant and enables the coolant to more easily carry corrosion particles from the steam generator tubes to the fuel rods, but it also reduces the likelihood of deposition on the fuel rods. A high pH can result in more of the corrosion deposits being removed through the reactor cleaning system rather than depositing on the fuel rods and being irradiated, thus reducing the radiation fields. However, higher lithium concentrations accelerates cladding corrosion. In a low pH environment, the acidic conditions can dissolve the outer CRUD layer, though it is not as effective at dissolving the more tenacious inner layer [11]. Another way to increase the pH is to use less boric acid. By enriching boric acid with boron-10, the main isotope that absorbs neutrons, the amount of boric acid needed for reactivity control is decreased [42].

In LWRs, increasing the amount of dissolved hydrogen in the water increases the decomposition of nickel ferrite, minimizes the formation of oxidizing species, and helps prevent stress corrosion cracking. Adding hydrogen to the fluid can decrease corrosion rates by counteracting radiolytic decomposition of water into oxidizing compounds [55, 11]. However, adding hydrogen can promote hydrogen induced cracking, which can lead to brittle fracture, especially in body-centered cubic iron alloys [5].

2.3.1.2 Flow Conditions and Heat Flux

Higher flow velocities can create a more turbulent flow that makes deposition difficult, and it can also increase the shear stresses to the point of pulling off the fouling layer. However, there is a competing effect with the higher flow velocity bringing more particles, microorganisms and their nutrients, and oxygen in contact with the surface, which can promote fouling and corrosion. Increasing flow will increase the fouling layer until the shear stresses remove the foulants faster than their deposition rate. Higher flow rates can also bring more oxygen to the surface, enhancing or impeding corrosion depending on whether a stable, passivating layer is formed [16, 6].

Another effect of higher flow velocities is enhancement of flow-assisted corrosion (FAC), which would increase the corrosion deposits source term. The passivating oxide layer that forms on metal surfaces can be dissolved when subjected to turbulent, fast-flowing fluid. This exposes fresh material for corrosion, and since the oxide layer is continuously removed, the metal continues to corrode. Figure 2-6 shows this process for different types of flow. During laminar flow, the oxide dissolution rate is low, but thermal power plants generally operate in the turbulet regime where FAC is a problem. Besides fluid velocity and surface material, FAC is also affected by pH,

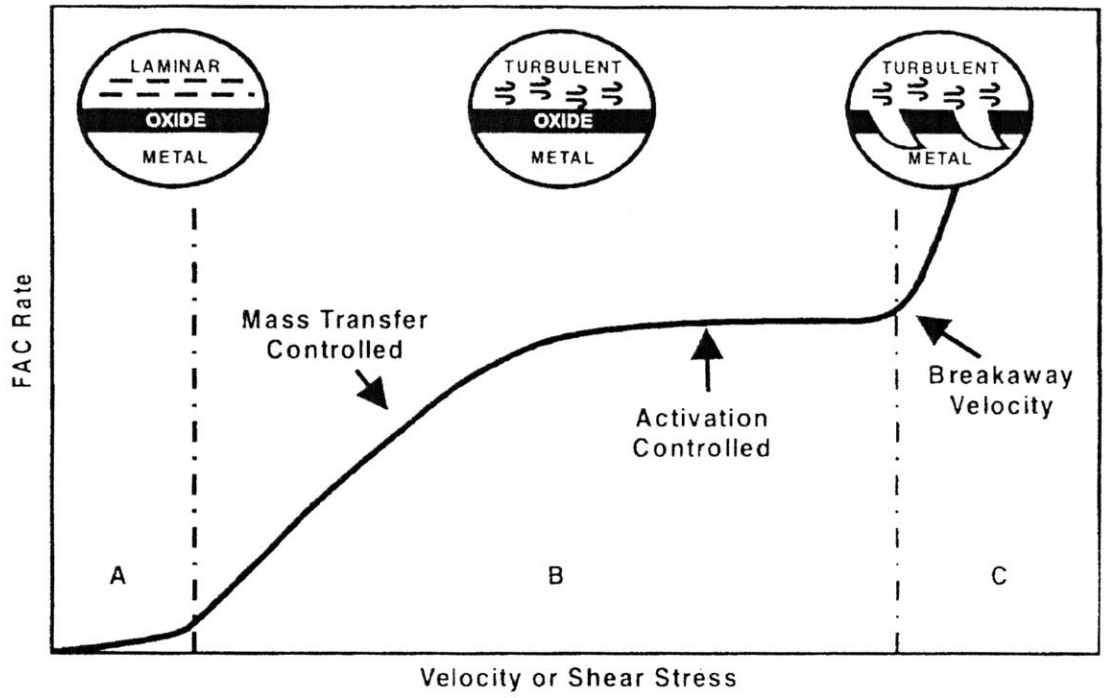

Figure 2-6: Flow-assisted corrosion rate as a function of fluid velocity on a metal surface with a protective oxide layer [5].

oxygen concentration, temperature, and geometry. The first three factors determines the oxide layer composition and solubility. Lower pH, lower oxygen levels, and higher temperatures increase FAC by increasing the solubility and decreasing the stability of the oxide layer.

Increases in temperature, which depend on heat flux, increase inorganic fouling (e.g., crystallization and particulate fouling), but decrease biological fouling since many organisms cannot withstand high temperatures [33]. The deposition rate is highly dependent on the level of sub-cooled boiling on the surface. As heat fluxes increases, the rate of subcooled boiling increases, which results in higher CRUD deposition [9]. One study by Wu, Jones, and Newell found a 25% increase of solutes near the bubble attachment point under nucleate boiling conditions in refrigerant R-124a [43]. Another interesting effect of increasing the heat flux through a surface his the increase in the boiling chimney population density, also due to increased nucleate boiling [13]. In a study by Barrera, the rate of CRUD deposition was estimated to be proportional to the fifith power of the local heat rate [63].

2.3.2 Fouling Mitigation by Filtering and Cleaning

Filtering or pretreatment of the fluid can remove salts, organic and inorganic content, oxygen, organisms, and particulates in the fluid before they get a chance to deposit on surfaces. Ion exchanges are commonly used to remove cations. Reverse osmosis can be used to force water to diffuse through a semi-permeable membrane, leaving salts behind. For soluble species, changing the pH or adding other species that react with them can precipitate out species (e.g., adding lime to precipitate out calcium and magnesium ions in water, or adding acid to convert bicarbonate to carbonic acid) to aid in filtering. Since many of the particles are small or in suspension, clarifying agents can be added to encourage flocculation to form larger clusters [6].

Deposits may be removed through several different mechanisms:

- Dissolution: deposits become ions in solution and leave the surface
- Erosion: particulates are moved away by external forces
- Spalling: large masses break off and leave

Cleaning of surfaces can be categorized into three categories: mechanical cleaning, chemical treatment, and thermal treatment. Mechanical cleaning includes the use of water jets and water lances, drilling and rodding, blast cleaning using abrasive material, air or steam blasts, sonic vibrations, and systems for circulating abrasive balls or brushes. For more loosely-bound or soluble foulants, simply rinsing with water may be enough to remove the layer. For more tenacious foulants, chemical treatments can be used with alkali, acid, or a combination to dissolve the foulants. Sodium hydroxide followed by nitric acid is commonly used in the food industry, as well as surfactants, chelating agents, or sequestrants. Sanitization, either through chemical or thermal treatment, may be used to kill microbes. Some cleaning can be done in place by changing flow rates, temperature, or chemical concentrations as long as it does not adversely affect the product. Thermal treatments, such as using thermal shock to crack the fouling layer to be peeled off, raising the temperature to increase particle solubility and reaction rates, making use of phase transitions of materials, or to kill microbes can also help remove fouling [36, 6].

In nuclear reactors, the fluid purification system only removes a small percentage of corrosion products [11]. Usual chemical cleaning is usually not sufficient to remove thick CRUD. Some nuclear power plants have removed CRUD using the more expensive method of ultrasonic fuel cleaning during reloading [9, 42]. Ultrasonic cleaning uses transducers to generate and direct ultrasonic waves towards the surface, causing

cavitation and removing the CRUD [64]. It is difficult to design and implement a system for on-line cleaning of the fuel rods in a reactor. The fuel rods are usually only taken out after a cycle is completed, which is currently about every 18 months in the US.

Another method of removing CRUD from fuel rods is by inducing a "CRUD burst," which releases corrosion products into the fluid system, before planned refueling. This would occur naturally when the reactor coolant system is exposed to the atmosphere, but is induced beforehand so that the activated products can be removed from the coolant system to decrease exposure to the workers. The corrosion products are released at a certain time by adding hydrogen peroxide into the coolant, creating oxidizing conditions that increases the solubility of the particles [55].

2.3.3 Fouling Mitigation by Material and Component Choices

2.3.3.1 System Design

The system can be designed to inhibit fouling or deal with its effects in several ways. Installation of pretreatment systems, such as water clarifiers, filters, settlers, ion exchange beds, etc., remove particles or organisms in the fluid before they get to surfaces. On-line cleaning systems and antifouling injection systems can help continuously precipitate or settle out and filter out foulants. These systems, as well as degasification, can also inhibit corrosion of surfaces and growth of organisms by removing chemicals or dissolved gasses that enhance corrosion, chemical, or biological fouling. Some designs may be less prone to fouling and its effects than others, such as fluidized bed heat exchangers, which help keep particles suspended and provide extra surface area to accomodate for heat transfer losses [6]. In coal power plants, on-line cleaning is in the form of sootblowing. Blasts of water, steam, or high-pressure air is forced through the boiler to remove soot. However, this method of cleaning lowers the efficiency of the plant since it requires more power and increase gas losses [56].

Systems could also be designed for easy maintenance or replacement of parts. In addition, a redundant system can be added to serve as a backup while the primary system is down for maintenance. This is often done in the oil refinery industry where their plants are designed with multiple heat exchangers that can be valved off for maintenance [6]. If fouling is irreversible or if it is more cost-effective to replace rather than clean components, as is usual for fouled membranes, the system can be designed for easy access and replacement [34].

2.3.3.2 Choice of Materials

The fluid and construction materials of a system greatly effects the fouling layer that forms. Some materials form stable, adhesive oxides that serve as a passivating layer, preventing the surface below it from continuing to corrode [6]. Using a material with the same charge as the foulants will increase the electrostatic repulsion forces between the two, inhibiting fouling. Materials and fluids with hydrophobic or hydrophilic properties can be chosen to minimize fouling [37]. Additionally, materials with low surface energy are more resistant to fouling and easier to clean [65].

Typical materials in LWRs are nickel-based alloys such as alloy 600, alloy 690, or alloy 800 for steam generator tubing; SS304 for piping, reactor pressure vessel cladding, and the channel heads of the steam generator; and zircaloy for fuel cladding [44]. Other materials include alloys X-750 and 718, SS316, and A0286 [11]. Alloy 800 is used in Europe and does not suffer from stress corrosion cracking issues as extensively as alloy 600 used in the US [12]. Plants that use alloy 690 instead of 600 for their steam generator tubing also have less corrosion issues [44].

Materials can be heat treated to improve their material properties, for example, increasing corrosion-resistance which will lower the corrosion deposit source term. In LWRs, the alloy 600 used for steam generator tubing is mill annealed (MA) or thermally treated (TT), and alloy 690 is thermally treated [11, 44]. The thermally treated alloys withstand corrosion better than the mill annealed alloys, so most reactors in the US now use alloy 690 TT.

2.3.4 Fouling Modification by Surface Modification

Surface modifications can prevent and mitigate fouling and its effects, but many factors need to be considered in choosing which technique to use. Ideally, the modification should be uniform, easily reproducible, cheap, and stable, while not adversely affecting other aspects of the system. For example, neutronics must be considered when choosing a coating for a reactor application.

2.3.4.1 Surface Treatment and Coating

Pickling, which is a surface treatment for removing impurities on metals, is often paired with passivating when used as a pretreatment technique. Pickling removes the outer layer of material that has less corrosion or fouling resistance. This is commonly applied for stainless steels where the outer layer has less chromium. After pickling

with nitric acid or hydrofluoric acid, the stainless steel will naturally form a passivating, chromium-rich oxide layer, though this can also be encouraged by heating the surface in oxidizing conditions [66]. Since smoother surfaces provides less contact area and fewer nucleation sites, they tend to discourage deposition. Surfaces can be pretreated by abrasive blasting for a smoother finish. Abrasive materials commonly used include glass beads, sand, or soda bicarbonate [67].

A simple and frequently used method to increase the fouling resistance of surfaces is to apply a coating that has a lower surface energy, decreases adsorption, or can protect against corrosion. Coatings on marine surfaces can be used to help mitigate fouling. However, frequent repainting is necessary due to coatings being worn down by solvent action of seawater or by being chipped off, the paint film itself can physically break down, or corrosion of the coated surface itself may occur. In systems where the water can be treated, injection of chlorine, sodium pentachlorphenate, or other chemicals can sterilize the water. This has some drawbacks, such as the large volume of water may need to be treated, the chemicals can increase corrosion of steel due to the destruction of the protecting bioslime coating, lowering the pH will kill off many organisms but is corrosive, and some chemicals can be a danger to humans. Heating the water can also be used to prevent biofouling, but the cost of installation and operation is high, unless it is used for plants with a lot of waste heat, and would need to be performed frequently to prevent microbial growth. Ships tend to be constructed from steel lined with lead, galvanized wrought-iron and steel, or copper-nickel alloys, which experience less fouling than other materials, but are nonetheless susceptible. Unfortunately, most metals that are fouling-resistant are vulnerable to erosion [16, 65].

Other modification techniques can be employed to control fouling besides coatings, including grafting of hydrophilic or hydrophobic polymers onto membranes, plasma treatment, and chemical reactions to introduce charged groups or biocides onto the surface [37]. Studies by O'Hanley et al. found that hydrophilic porous surfaces had CHF enhancements of up to 60%, and hydrophobic porous surfaces saw a reduction of up to 97% compared to an uncoated sapphire heater [68]. A porous surface was created by depositing nanoparticles on the surface, either using silica or fluorosilane compounds for hydrophilic and hydrophobic surfaces, respectively. Hydrophilic porous surfaces improve rewetting of the surface and increase CHF, whereas hydrophobic surfaces decrease wettability. However, non-porous hydrophilic and hydrophobic surfaces did not result in much change in the CHF, indicating that porosity is a large factor in CHF, and wettability only mattered on porous surfaces. Surface roughnesses varying from smooth surfaces to 15 μm tall micro-posts also did not affect

CHF much [14, 68]. Nanoparticulate deposits can enhance CHF and increase the heat transfer coefficient by increasing wettability and capillarity. One study found that the CHF was higher by as much as 90% compared to uncoated heaters, though the CHF decreases as the imposed cross section of the heater deviates from that of a circle [69]. Membranes, unlike most surfaces, are less susceptible to fouling when surfaces are hydrophilic rather than hydrophobic. Coating membranes with water-soluble polymers or surfactants to change hydrophilicity, smoothness, and surface charge have shown increased foulant resistance [37].

In nuclear reactors, coatings have to be carefully chosen due to the presence of hight temperature water or steam and ionizing radiation. For example, alkyds, a polyester modified with other components, is commonly used in industry as a surface coating. However, they would be inapproriate for use in critical areas of the reactor because they do not have good chemical or moisture resistance and would break down when exposed to radiation [70]. Inorganic zinc is used to provide galvanic protection for steel, but there have been concerns about hydrogen gas generation when in contact with steam [71]. Silicon carbide (SiC) is used to coat superheaters and is used in tristructural-isotropic (TRISO) fuel to retain fission products. SiC has excellent radiation resistance and can withstand high temperatures in addition to having high corrosion resistance, making it a suitable for use in reactor conditions [72, 73].

2.3.4.2 Microtexturing

Increased surface roughness usually increases fouling since valleys hinder removal from shear stress and hills can serve as nucleation sites. Some studies have shown that increasing surface roughness can lower the wall superheat needed for boiling to occur and different surface finishes can shift the position of the boiling curve significantly [53, 74]. Nanoparticle deposition on surfaces have recently been explored as a potential surface modification for mitigating fouling. On membranes, nanoparticles such as titanium dioxide (TiO_2) with superhydrophilicity decrease fouling and with their photocatalytic properties can decompose organic compounds, forming self-cleaning surfaces [75, 37].

In the nuclear industry, there have been proposals to polish fuel cladding to make them as smooth as possible in order to minimize deposition [76]. Alternatively, improved boiling can increase the heat transfer of the surface. However, there is very little information on exploiting the CRUD layer to obtain better heat transfer. Bubble formation and departure from surfaces is a very efficient mode of heat transfer and is

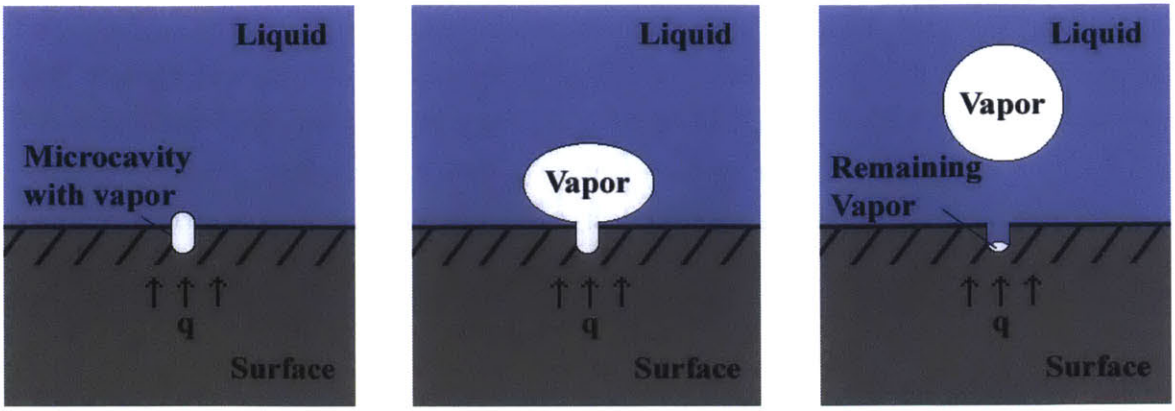

Figure 2-7: Bubble growth on heated surface with some vapor left in the microcavity after bubble departure.

desirable in nuclear reactors, as long as it stays in the nucleate boiling regime. When the CHF is reached, the heat transfer efficiency decreases, which can lead to overheating and burnout of the surface underneath. Increasing the surface roughness is one way to increase the number and size of the cavities. Several studies have observed that bubble nucleation tends to occur more frequently at microcavities for a given heat flux [74, 53]. Chen, Wu, and Jones examined the relationship between active nucleation sites and several different cavity geometries. They found that the pit and groove type cavities were the best for nucleation [48]. Cavities that do not get fully wetted tend to be more stable nucleation sites due to vapor trapping (see Figure 2-7). In experiments by Jones, McHale, and Garimella, increased surface roughness showed a two-fold increase in the heat transfer coefficient compared to smooth surfaces, but was less effective when the roughness was small or the pressure of the system was high, the second of which is the case in PWRs [53].

Poniewski and Thome examined numerous studies and found that in general, micro-structured surfaces outperformed smooth surfaces in terms of heat transfer. They ascertained that whether a microscopic bubble remained in the cavity largely determined whether the site remained active. This is highly dependent on the cavity geometry and wettability of the surface. A smaller capillary size resulted in a smaller temperature difference (i.e., superheat) needed to initiate bubble growth. Experiments done by Bergles and Chyu with copper particles coated on surfaces showed that the manufactured surface required less superheating to initiate boiling and the surfaces achieved heat transfer coefficients up to eight times larger than smooth surfaces [77]. Zhang and Chen found heat transfer coefficients 3-10 times larger for copper surfaces sintered with particles to produce capillary-porous structures compared to

smooth surfaces [78]. Fedorov used stainless steel meshes welded to the surface, and the finest mesh had a heat transfer coefficient 20 times that of a smooth surface [50]. Investigations by Poniewski and his colleagues showed heat transfer coefficients 5.5 times larger for porous coated surfaces than smooth surfaces [50]. Experiments by Toloei, Stoilov, and Northwood showed decreased corrosion rate on patterned surfaces on nickel metal [79].

2.4 Summary

Fouling is a wide-spread problem in both heated and non-heated systems. Factors effecting the adhesion of foulants to a surface include London-van der Waals forces, electrostatic forces, contact area, surface energy, particle size and concentration, particle solubility limits, hydrodynamic interactions, fluid velocity, and heat flux. Various types of fouling can occur, and foulants can vary from microorganisms to soot. The fouling mechanism of interest in this experiment is CRUD deposition that occurs on fuel pins in nuclear reactors. While many mitigation techniques have been explored, such as zinc injection or ultrasonic cleaning, no method has completely prevented CRUD growth. In addition, few studies have examined the effect of engineered surface textures on CRUD formation. Of particular interest is the formation of vapor chimneys in the CRUD layer, which could produce a beneficial boiling effect for enhancing heat transfer.

Chapter 3

Experimental Methods

3.1 Materials and Materials Preparation

3.1.1 Sample Preparation

Test grade silicon wafers 500 μm thick were ordered from American Precision Dicing, Inc. and came diced into 10 mm $\times$ 10 mm squares. The monocrystalline silicon wafers were uncoated and had one side fully polished. A 8 mm $\times$ 8 mm square grid of holes, leaving 1 mm on each side, was drawn in CAD software CleWin. Table 3.1 shows the various pitches of the microcavity samples, measured from center to center, and the expected density of the microcavities. Plain silicon substrates without any photolithographed defects are labelled as control samples.

The microfabrication process included using a Shipley 1813 photoresist to spin coat the silicon substrates to a thickness of approximately 1.4 μm. Lithography with a Direct Write uPG501 by Heidelberg Instruments was used to make 3 μm diameter holes on silicon substrates in the desired pattern. Reactive ion etching

Samples	Density (microcavities/mm^2)
30 μm pitch	333
50 μm pitch	200
80 μm pitch	125
100 μm pitch	100
500 μm pitch	20
800 μm pitch	13
Control (no microcavities)	0

Table 3.1: Microcavity pitches and microcavity density.

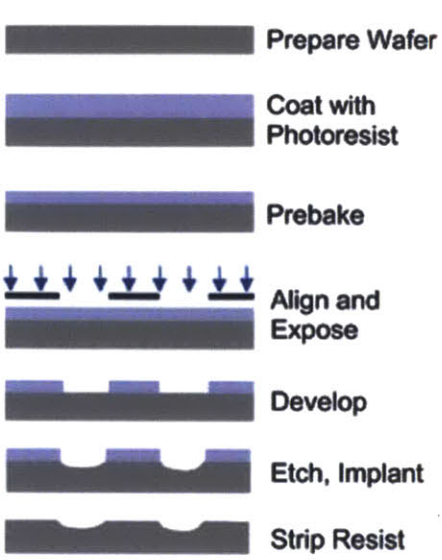

(a) Photolithography and etching process [80].

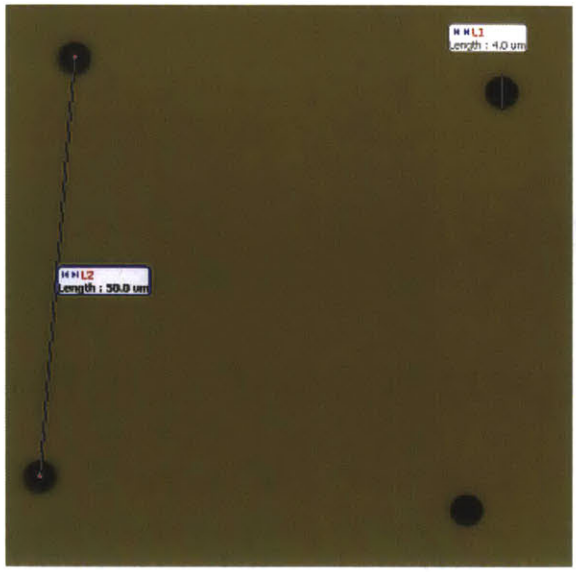

(b) Part of the final pattern after reactive ion etching 50 μm pitch microcavities onto a silicon substrate.

Figure 3-1: Lithography process and silicon substrate after processing.

included placing a photomask on top of the photoresist and then exposing it to UV light to remove parts of the photoresist. The substrate then underwent etching using sulfur hexafluoride (SF_6) and octafluorocyclobutane (C_4F_8) to remove the exposed parts of the silicon surface. After reactive ion etching, the holes had a diameter of approximately 4-5 μm with a depth of approximately 7 μm. Figure3-1a shows this process and Figure 3-1b shows part of the grid on a silicon substrate after etching was completed. The remaining photresist was removed by sonicating the silicon substrates in acetone for one minute and then rinsing the surface with ethanol.

Two samples had microposts instead of microcavities. Uncoated, 650 μm thick monocrystalline silicon wafers diced into 22 mm $\times$ 22 mm squares were etched with 20 mm $\times$ 20 mm square grids of microposts using contact photolithography and reactive ion etching, similar to the way the microcavity samples were made. A photoresist and thermally grown oxide layer covered the areas that would become the micropillars. Reactive ion etching was used to etch the areas around the microposts, and the depth was controlled by altering etching time. The photoresist was then removed using sulfuric acid and hydrogen peroxide. The microposts had a circular cross-section with a diameter of 10 μm. The microposts were 3 μm tall with a pitch of 25 μm for one sample, and 6 μm tall with a pitch of 15 μm for the other sample.

3.1.2 PWR Water Simulant

Coolant in PWRs has approximately 1500 ppm of boric acid and 3 ppm of lithium hydroxide at the beginning of the fuel cycle. Because our experiment used deionized water for simplicity, not deaerated water as PWRs do, the pH was lower than normal. Deionized water reacts quickly with carbon dioxide in the air to form carbonic acid. To maintain a pH around 7 that is usual in nuclear power plants, less H_3BO_3 (10 ppm) and more LiOH (5 ppm) was used in our experiment. Boric acid with 99.945% purity was supplied by Mallinckrodt and anhydrous lithium hydroxide with 99.995% metal basis was supplied by Alfa Aesar.

Nanoparticles of nickel(II) oxide (NiO) and iron(II,III) oxide (Fe_3O_4) were also added to simulate corrosion deposits. Most reactors have a few ppm or less of nickel and iron oxides, but this experiment used 100 ppm each to accelerate CRUD growth. NiO in the form of 8-20 nm average particle size (APS) powder with a 99+% metal basis and Fe_3O_4 in the form of 20-30 nm APS powder with a surface area of approximately 60 m^2/g and a 98% metal basis were supplied by Alfa Aesar. Deionized water with a resistivity greater than 15MΩ was used.

Weighing by difference was used to weigh out the appropriate amount of NiO and Fe_3O_4 to be mixed with deionized water to form a concentrated mixture of 600 ppm each. H_3BO_3 and LiOH were mixed with deionized water in concentrations of 12 ppm and 6 ppm, respectively. When preparing a batch of PWR water for the experiment, the NiO and Fe_3O_4 mixture was shaken and sonicated for 5 minutes to ensure the particles were homogeneously distributed. A Vibra-Cell sonicator supplied by Sonics & Materials, Inc. with a 1/2" diameter microtip probe was used at an amplitude of 50-60% for approximately 500 mL of fluid. To make the PWR water simulant, 200 mL of the NiO and Fe_3O_4 solution was poured out and mixed with 1 L of the H_3BO_3 and LiOH solution, which was also shaken beforehand. This resulted in 1.2 L of solution containing 100 ppm NiO, 100 ppm Fe_3O_4, 10 ppm H_3BO_3, and 5 ppm LiOH. For the 50 ppm NiO and Fe_3O_4 PWR simulant, 100 mL of the NiO and Fe_3O_4 mixture was mixed with 100 mL of deionized water and 1 L of H_3BO_3 and LiOH solution instead. After mixing, the solution was sonicated again for 5 minutes. This allowed the particles to stay in suspension during the experiments with 1 hour of boiling, though the 24 hour experiments resulted in a much clearer solution at the end of boiling, indicating that many of the particles did settle out as boiling occured.

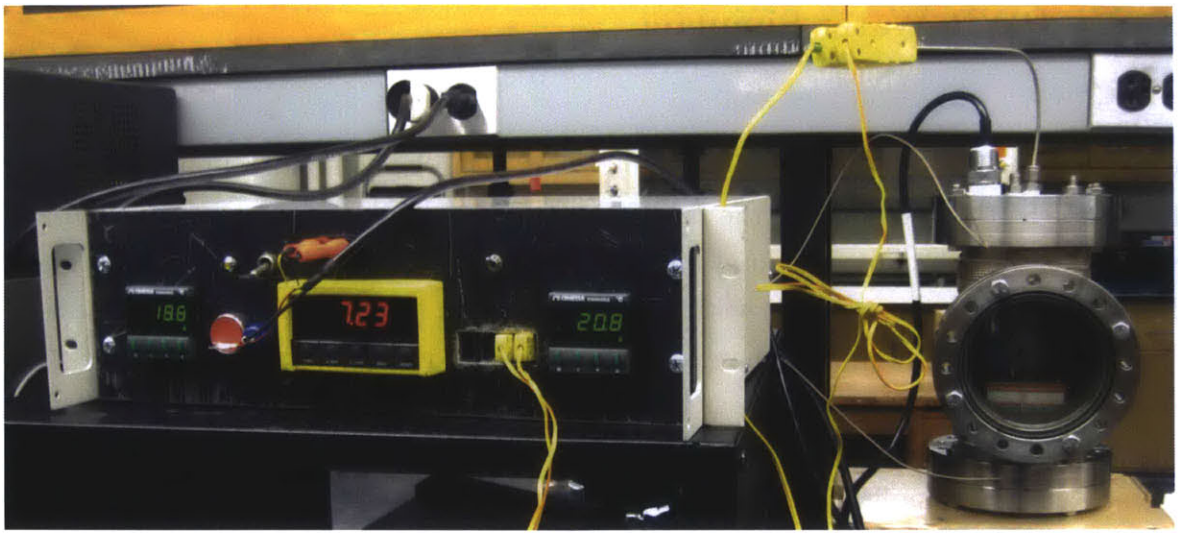

Figure 3-2: Photograph of boiling facility (right) and electronic control box (left).

3.2 Experimental System

The experimental setup consisted of the boiling facility, electronic control box, and a datalogger. The boiling facility housed the sample heater and the pedestal that holds the sample while boiling. It was attached to a pump for circulating PWR water in the facility. K-type thermocouples connected the boiling facility and the electronic control box. The electronic control box contained the sample heater and bath heater controllers as well as the pH meter. The datalogger contained the logomatic on a carrier board and attached to an amplifier box. There were two identical setups, identified as Facility 1 and Facility 2. Figure 3-2 shows one of the boiling facilities with its associated electronic control box.

3.2.1 Boiling Facility

Figure 3-3 shows the internals of the boiling facility. The base of the boiling facility contains a pedestal that contains the heating element for the sample. The exterior of the boiling facility has a HTS/Amptek heavy insulated heating tape clamped to it. The sample and bath heaters are connected to the electronic control box so that they only turned on when both the heater switch has been turned on and the safety button had been pressed on the electronic control box. The bath heater provides 288 W of power, and the sample heater has an additional dial to control the percent of power applied such that, when boiling, was turned to 144 W. The main mode of heat transfer to the sample and the wall of the boiling facility is thermal conduction

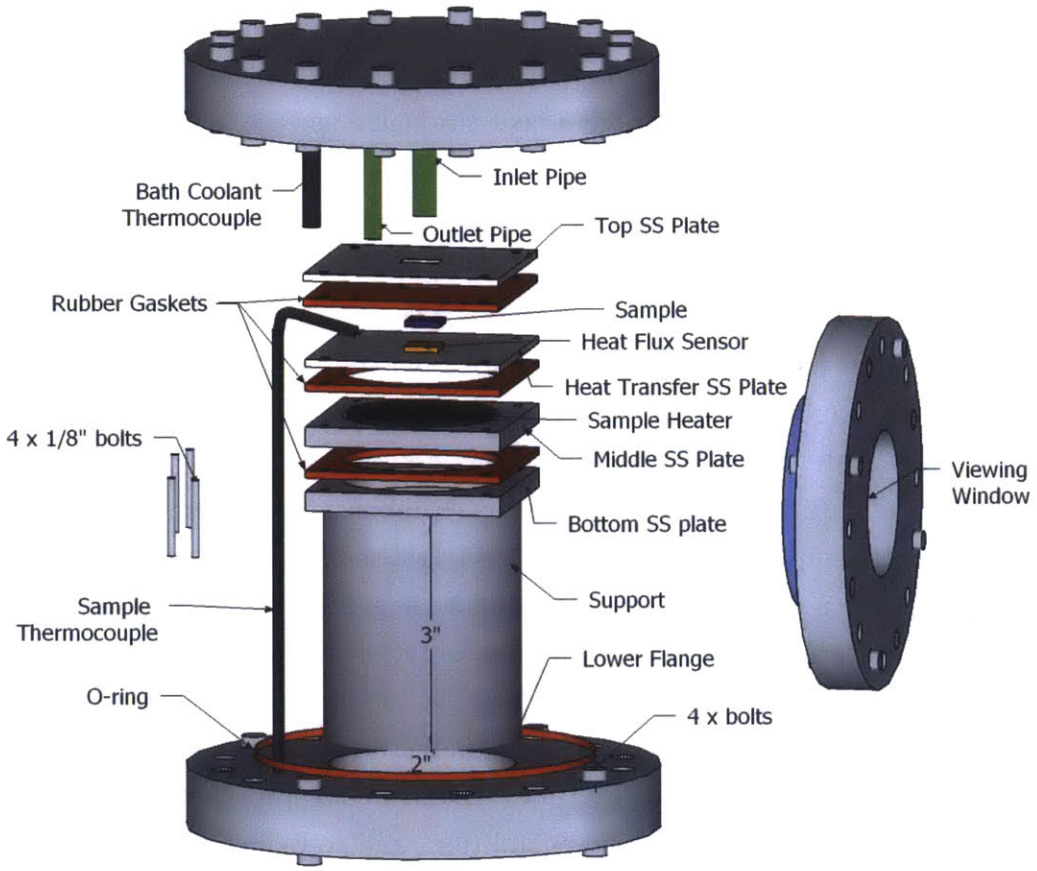

Figure 3-3: 3-D model of boiling facility internals.

whereas heat transfer in the bulk fluid is through convection.

On top of the sample heater lies a stainless steel heat transfer plate. A heat flux sensor is located in the middle of the plate, and is attached to the plate with an adhesive that also protects the heat flux sensor from high temperature water. The heat flux sensors used are 10 mm $\times$ 10 mm (the same size as the silicon samples) and 0.45 mm thick, supplied by Captec Enterprise. It utilizes a flat, copper plate with 2 copper cable leads that outputs a voltage signal proportional to heat flux with a response time of 0.3 seconds. The heat flux sensors came calibrated, 1.11 $\mu V/(W/m^2)$ for Facility 1 and 0.822 $\mu V/(W/m^2)$ for Facility 2, with a calibration accuracy of +/- 3%. The heat flux sensor generates a voltage directly proportional to the heat flux, which is the rate of energy transfer from heat through a surface, measured in units of W/m^2. Measurements from a series of thermocouples on the bottom and top surface of the copper plate are taken to calculate the temperature difference. The sample would be placed directly on top of the heat flux sensor.

Silver conductive grease with a silicone base, supplied by Chemtronics, was placed between the copper plate and the stainless steel plate to fill in air gaps between the two surfaces to enhance thermal conductivity. The thermal conductivity of the silver paste was 5.6 W/m-K. The silver conductive grease was also used between the copper plate on the heat flux sensor and the sample. Rubber gaskets were placed between the stainless steel components to ensure a watertight seal. The top rubber gasket and top steel plate have a 8 mm $\times$8 mm opening for the sample. They clamped down on the sample by tightening the four bolts at the corners of the plate. Early experiments experienced a lot of water boiling from the sides of the middle steel plate (which enclosed the sample heater) due to thermal conduction through the plate. The bulk water temperature would often exceed its setpoint and approach the boiling point. To maintain subcooled nucleate boiling conditions and to reduce the amount of heat loss through the steel plate, a strip of rubber was clamped around the perimeter of the middle steel plate in order to insulate it.

K-type thermocouples from Omega Engineering were used for measuring the temperature of the bath water and the sample. The bath thermocouple entered from the top of the facility and the tip sits off-center and slightly above the top steel plate. The bath thermocouple has two connections as a safey precaution, one going to the electronic control box and the other going to the datalogger. The sample temperature is indirectly measured by placing two smaller thermocouples on the stainless steel heat transfer plate above the heater, the same plate the heat flux sensor is sitting on. One thermocouple is connected to the electronic control box and the other is connected

to the datalogger.

A medium/high flow variable-speed peristaltic tubing pump from Control Company, with flow rates ranging from 0.005 mL/minute to 600 mL/minute, was used with 3/16 inch inner diameter tubing to circulate the water in the boiling facility. A Fl-3939ST rotameter supplied by Omega Engineering was used to estimate the approximate flow rates used in the experiments with an accuracy of $\pm 2\%$. The usual speed was 2-Fast on the pump, which corresponds to a flow rate of approximately 128 mL/minute. The water intake was near the edge of the facility and the outlet was 2-3 centimeters above the sample.

It was observed during previous experiments without the pump that sometimes a vapor film would develop over the sample. Rewetting the surface was not only difficult due to a high temperature being maintained as a result of the lower heat transfer with the presence of an insulating vapor layer, but also because the sample sat lower than its surroundings (the top rubber gasket and steel plate) in our boiling facility. Adding the pump to circulate water prevented a stable vapor film from developing on the surface of the sample, hindered sedimentation during the experiment, and more closely matches the flow conditions we would expect in a PWR. The pump was set to a low flow rate to avoid cooling the sample surface as much as possible while still preventing stable film boiling.

3.2.2 Electronic Control Box

The circuit diagram for the electronic control box is shown in Figure 3-4. The electronic control box contained two solid state relays that controlled load current to the bath water and sample temperature controllers. The SSR240AC45 solid state relays by Omega Engineering used in Facility 1 have a maximum load current of 45 amps and an actuation voltage of 3 Vdc. The SNC-R2025-507 solid state relays by National Controls Corporation used in Facility 2 have a maximum load current of 25 amps and an actuation voltage of 3 Vdc. The C9000A temperature controllers were supplied by Omega Engineering. The bath and sample thermocouples were inputs for the temperature controllers. The setpoints on the temperature controllers were 97°C for the bulk water and 125°C for the sample. They controlled the amount of power supplied to the heaters and also also provided real-time data on bath and sample temperatures during boiling.

The temperature controllers operate with a Proportional-Integral-Derivative feedback mechanism. The proportional time was 20 seconds, the proportional band (in-

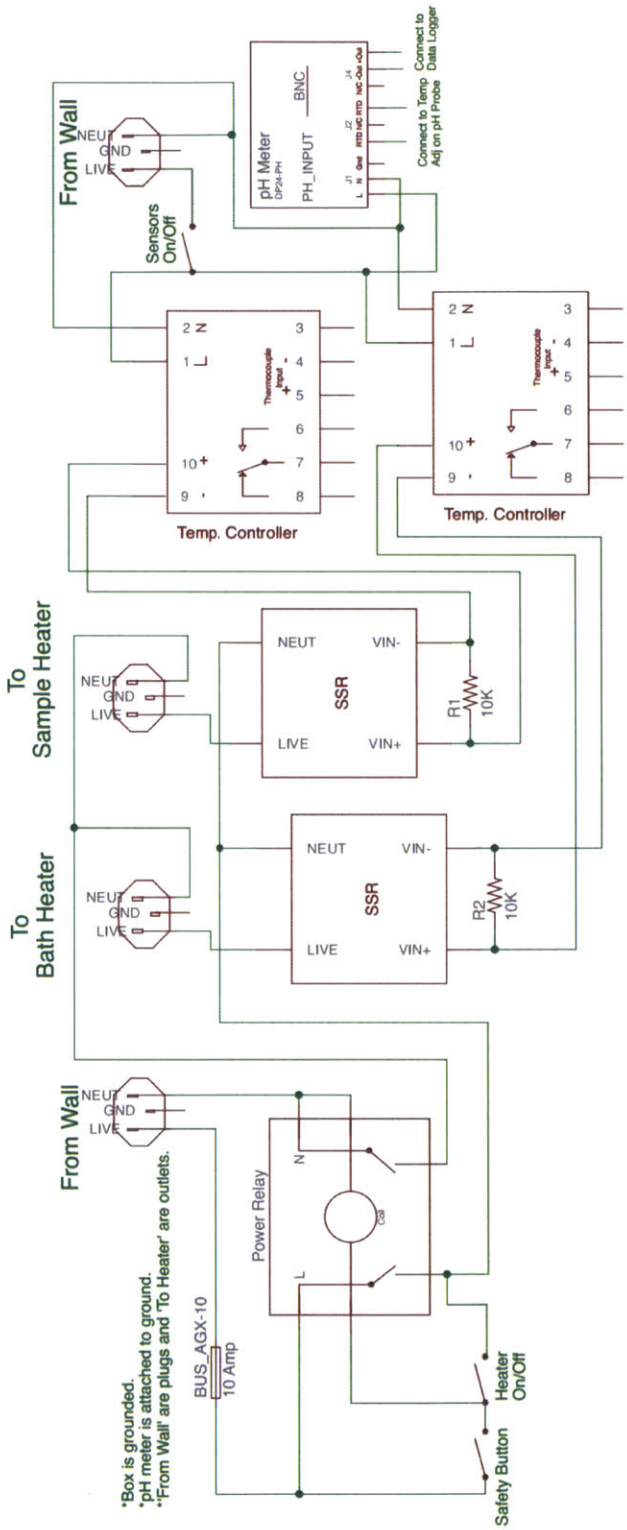

Figure 3-4: Electronic control box circuit diagram.

verse of gain) was 2.5% of the full scale, the derivative time was 25 seconds, and the integral time was 350 seconds. A proportional control causes the power supplied to the heater to decrease as the temperature approaches the setpoint to prevent overshooting the setpoint. The integral time constant adjusts the proportional band to compensate for offsets from the setpoint. If it is set too high, the heater will take longer to reach the setpoint. If the integral time constant is too short, the heater responds very quickly and the temperature could overshoot, then overcorrect, and then continue to oscillate in this manner around the setpoint temperature. The derivative rate time shifts the proportional band according to the rate of temperature change to minimize overshooting or undershooting. For example, if the rate of temperature change is slow, the proportional band would be shifted higher so that the response of the heater is slower [81, 82]. The cycle time for the bath heater was left on the default 20 seconds, but the cycle time for the sample heater was set to 0.3 seconds to get a fairly continuous heat flux through the sample surface. Such a fast cycle time is only possible due to the use of solid state relays instead of mechanical relays. A longer cycle time would have allowed the sample to cool down more before the heater is turned on again, so a short cycle time was chosen to maintain a steady heat flux.

3.2.3 Datalogger

SparkFun Electronics' logomatic and carrier board was supplied by Ocean Controls. It was used to read 0-3.3V inputs from the amplified sample and bath thermocouples signals and from the heat flux sensor. The circuit diagram for the amplifiers is shown in Figure 3-5. The actual logomatic and amplifier box are shown in Figure 3-6. The logomatic was set to record to a microSD card in ASCII format at a frequency of 1 Hz. Analog-to-digital logging was used to convert the voltage to a number within the range of 0 to 1023 for each channel. This value was then converted to the appropriate units of measurement.

Since the sensitivities of the heat flux sensors were known, the conversion between the levels recorded by the logomatic and heat flux in $\mathrm{W/m^2}$ is simply the voltage per level divided by the sensitivity. Using the heat flux sensor with a sensitivity of 1.11 $\mu\mathrm{V/(W/m^2)}$ as an example, we calculated the conversion factor F_{HFS1} in the following way:

$$F_{HFS1} = \frac{3.3\,V}{1024\,levels} \times \frac{10^6\,\mu V/V}{1.11\,\mu V/\,(W/m^2)} \approx 2903.294\ \left(W/m^2\right)/level \qquad (3.1)$$

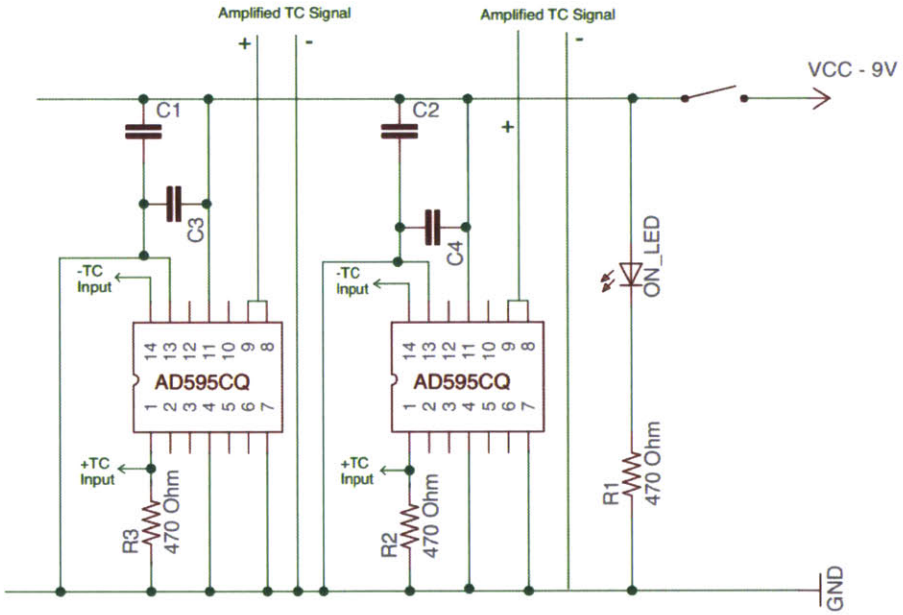

Figure 3-5: Thermocouple amplifiers circuit diagram. The inputs come from the sample and bath thermocouples in the boiling facility. Capacitors are used to filter out noise and smooth the output of the power supply. When switched on, the LED lights up to show that the circuit is working. The amplified thermocouple (TC) output signals are the inputs for the logomatic.

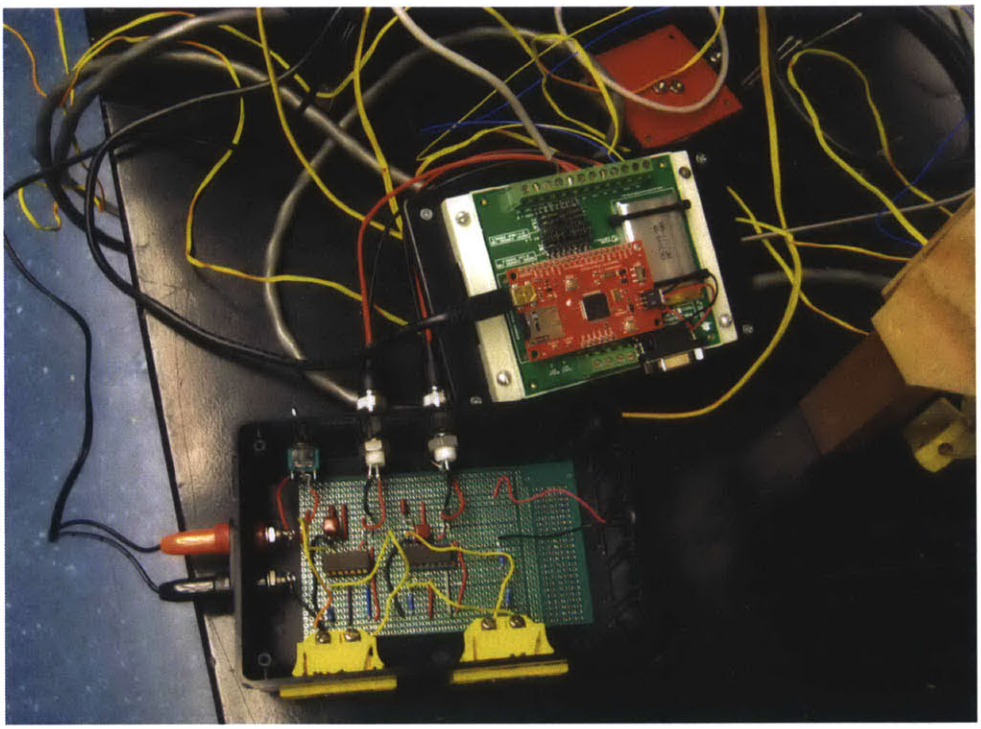

Figure 3-6: Logomatic with carrier board and amplifier box. The banana plugs connect the power supply to the amplifier box. The sample and bath thermocouples from the boiling facility connect to the two standard K-type panel connectors. The outputs from the black amplifier box connect to the logomatic carrier board via BNC connectors. The logomatic and carrier board have a LiPo battery and can also be powered via the USB connector.

Multiplying the recorded level by this conversion factor gives the heat flux in units of W/m^2.

Since the voltage of the thermocouples were very low, AD595CQ cold junction thermocouple amplifiers made by Analog Devices, Inc. were used. These integrated circuit chips increased the signal from the bath and sample K-type thermocouples coming from the boiling facility through a differential amplifier. The signal is then applied through gain scaling resistors so that the final output is 10 mV/°C. They have a calibration accuracy of +/- 1°C. The bath and sample thermocouples are directly proportional to the voltage, with level 0 being 0°C. The conversion factor for both thermocouples, denoted as F_{TC}, was calculated in the following way:

$$F_{TC} = \frac{3.3\,V}{1024\,levels} \times \frac{1000\,mV/V}{10\,mV/C} \approx 0.322266\,C/level \tag{3.2}$$

3.3 CRUD Growth Procedure

The boiling facility was used to grow CRUD at an accelerated rate. The experiment had many simplifications compared to real PWRs. Silicon substrates were used rather than Zircaloy, but if it can be proven that CRUD morphology can be controlled through induced microcavities on silicon surfaces, it would indicate that it is worth pursuing this avenue for real cladding materials. The simulated PWR coolant had more nickel and iron oxides in it than found in reactor coolant to speed up the CRUD deposition process. Another important deviation from PWR conditions is that our boiling facility was operated at atmospheric pressure rather than the typical PWR pressure of 15.5 MPa. This also changed the boiling point of the coolant from around 315°C to 100°C. Our experiment held the bulk water close to the boiling point, with wall superheat of 25°C. No radiation fields were present during the experiment, but irradiation can change material properties and the effects of the CRUD layer on the system.

3.3.1 Test Matrix

In order to determine the effect of the induced microcavities on vapor chimney formation, different grids of holes were used. The pitch of the microcavities varied from 30 μm to 800 μm. The first tests used 50 ppm of nickel and iron oxides, but later tests used concentrations of 100 ppm to speed up the CRUD deposition process. Two samples were run for 24 hours rather than the usual 1 hour to see the effect of time

over CRUD growth. In addition, two samples with grids of 3 μm tall, 25 μm pitch and 6 μm tall, 15 μm pitch microposts were used to observe the introduction of these surface defects on CRUD morphology and vapor chimney formation. Table 3.2 shows the text matrix containing microcavity and micropost pitches, boiling time, concentration of nickel and iron oxides in the PWR water simulant, and average heat flux.

3.3.2 Boiling Procedure

Silicon substrates were prepared by photolithography and then heated in the boiling facility. The experimental procedure for boiling is as follows:

1. Coat the heat flux sensor with a thin layer of silver conductive grease and put a sample on heat flux sensor.
2. Wedge the sample thermocouples between the stainless steel heat transfer plate and the rubber gasket, close to the heat flux sensor.
3. Use four bolts at the corners to ensure the rubber and stainless steel gaskets tightly clamp down on the sample.
4. Place the O-ring around bottom flange and place bolts, spaced evenly, along bottom flange. Put the body of the facility on.
5. Tighten the bolts connecting the body with bottom flange.
6. Measure out and sonicate 1.2 L of PWR water simulant. Check that pH of the PWR water is around 7, either with a pH strip or a pH probe.
7. Check the water valve is closed, fill up the pool facility with the of PWR water from the hole on the top flange, and plug the hole with a swagelok cap.
8. Place the bath thermocouple in the facility from the entrance on the top flange and tighten the swagelok. Connect the sample and bath thermocouples to the electronic control box.
9. Turn on the electronic control box to read the sample temperature and bath temperature. Check that the bath temperature setpoint is at 97°C and the sample temperature setpoint is at 125°C.
10. Switch on the amplifier box and turn on the datalogger. Check that there is a microSD card ready to record data.

Sample	t (h)	Conc. (ppm)	Heat Flux (kW/m^2)	Std. Dev. (kW/m^2)	pH	Notes
Control	1	100	65.5 16.4 18.1	24.3 10.6 7.86	6 6/6.5 [10] 8	[1,2] Heat flux sensor was not working. [3] Sample temperature excursion up to 180°C. [4] Possible temperature excursion up to 190°C. [5] In SEM images, saw that this was actually a 30 μm pitch sample. [6] In the middle of the experiment, the sample heater shut down for 5 minutes. Only recorded last 30 minutes. [7] Temperature excursion to 170°C near end of run. [8] Heat flux sensor not working. [9] Sample temperature excursion up to 190°C. [10] Second pH value is included if there was a change after boiling.
Microcavity 100 μm pitch	1	100	3.97 [1] 19.0 7.91[2]	1.28 12.1 1.74	7 6.5 7/7.5[10]	
Microcavity 80 μm pitch	1	100	37.7 51.9 25.3 [3]	34.3 11.3 15.0	7 7/7.5[10] 7/7.5[10]	
Microcavity 50 μm pitch	1	100	9.68 [4] 17.2 17.6 [5]	7.83 8.05 7.25	7/8[10] 7 7	
Microcavity 30 μm pitch	1	100	18.0 [6] 18.9 33.6 [7]	14.8 2.99 21.2	7 7 6.5[10]	
Control	24	100	36.8 — [8]	15.7 —	7/8 7/8	
Control	1	50	32.2 35.1	16.3 16.9	6.5/7[10] 7	
Microcavity 50 μm pitch	1	50	87.3 [9] 24.7	51.4 18.9	7 6/6.5[10]	
Microcavity 500 μm pitch	1	50	18.2 49.1	17.1 19.1	6/6.5[10] 6.5/7[10]	
Microcavity 800 μm pitch	1	50	8.03 38.4	3.68 15.4	6/7[10] 6/6.5[10]	
Micropost 3 μm tall	1	100	40.2	16.5	7.5	
Micropost 6 μm tall	1	100	17.9	7.24	7	

Table 3.2: Test matrix of samples including the pitch (if microcavities or microposts are present), boiling time (t), concentration of NiO and Fe_3O_4, average heat flux, average heat flux standard deviation (std. dev.), pH, and notes on any anomalies during the runs.

11. Make sure the sample heater dial is off. Flip the heater switch and push the safety button on the electornic control box to start heating the bulk water.

12. When the water approaches the bath temperature setpoint, which takes approximately 70-80 minutes from when the bath heater is turned on, turn up the sample heater.

13. Start timing when the sample temperature reaches the setpoint, which takes a few minutes.

14. Let it run for as long as the experiment calls for. Afterwards, turn off the sample and bath heaters.

15. After the experiment is done, take a PWR water sample in a vial. Check the pH of the water. Drain the PWR water from the facility, then close the drain.

16. Stop recording data on the datalogger and transfer the text file from the microSD card to a PC. Turn off the datalogger and amplifier box.

17. Turn off electronic control box. Unplug the bath heater and thermocouples that connects the boling facility to the electronic control box.

18. Remove the bolts on the gaskets and carefully place the sample in a labelled sample holder.

19. Wipe down the facility.

3.4 Analyses

The goals for the analysis of the CRUD samples were to determine the relationship between surface texture and CRUD and vapor chimney formation. The main tools used for imaging and analyses was a field emission scanning electron microscope (FESEM) and a FIB. A description of the method of analysis follows.

3.4.1 Tools for Analysis

3.4.1.1 SEM

A field emission scanning electron microscope was used to observe any correlation between vapor chimneys and location of microcavities. Most of the pictures were taken with a Zeiss FESEM Supra55VP at the Center for Nanoscale Systems (CNS)

Figure 3-7: FESEM Supra55VP.

at Harvard University, shown in Figure 3-7. The samples were mounted onto pin stubs using copper conducting tape and then placed onto the sample stage of the SEM. In a SEM, a beam of electrons is generated by an electron gun at the top of the SEM column. The beam is aimed at the sample, going through a condenser lens and then an objective lens in the SEM column before reaching the sample chamber. The system must be under vacuum to prevent the scattering of electrons against gas molecules. Poor vacuum makes imaging difficult and could also damage the system.

The incident electron beam causes secondary electrons to be ejected from the sample, and a few of the original electrons also backscatter from the surface. Secondary electrons give better resolution since they are more sensitive than backscattered electrons. Backscattered electrons are able to come from deeper within the sample than secondary electrons, which are emitted close to the surface of the sample. However, backscattered electrons are sensitive to the atomic mass of the material they are scattered from. For example, heavier atoms showing up brighter in the image since the electrons are scattered back more strongly. Secondary electrons are more useful for looking at the topography of the sample, while backscattered electrons are more important for chemical information [83].

The In-Lens detector, located inside the electron column of the SEM, and the SE2 (Everhart-Thornley) detector were used. The In-Lens detector is very efficient at collecting secondary electrons to give an image of the morphology and surface topography of the sample. The SE2 detector collects both secondary electrons and backscattered electrons. Areas from which more secondary electrons reach the detector results in brighter areas on the image.

3.4.1.2 FIB

A focused ion beam was used to cut samples to get a cross-sectional view of the CRUD layer. A Zeiss NVision 40 at the CNS was used for milling. The FIB is combined with a FESEM to allow for imaging in the same way as mentioned in the previous section. The SEM column is vertical while the FIB column is 54° from vertical. The FIB column contains liquid gallium metal, chosen for its low vapor pressure and because it is relatively unreactive. For milling, the FIB focuses a beam of gallium ions, which goes through a condenser and objective lens before exiting the injection nozzle into the sample chamber. When the gallium ions hit the sample surface, some of the atoms on the sample surface are ejected. A higher current causes more sputtering so samples can be milled faster, but the resolution is worse than at a lower current. For deeper cuts or for harder material where milling is more difficult, the dwell time can be increased, or the cut can be made in several layers (i.e., the beam sweeps across the chosen area multiple times). One drawback of this process is that some of the gallium ions are implanted on the surface of the area that was milled. However, this can cleaned off using the ion beam at a lower current.

3.4.2 Analysis Methods

A working distance of 5-15 mm was used for sample observation. A lower working distance and a smaller spot size allows for higher magnification, but results in smaller depth of field. The image is in focus when the working distance of the sample is at the focal point of the electron beam. The extra high voltage (EHT) level was within the range of 3-10 kV. If charging was seen on the sample, the EHT could be adjusted. When charge accumulates on nonconductive samples, resulting in streaks and abnormally lighter or darker areas. A smaller beam may reduce the charging issue and can also provide better resolution. A sharp image was obtained by changing the focus, stigmation, and aperture alignment. Astigmatism is when the images are stretched in the x- or y-direction and this can be fixed by using the stigmator. With

the wobbler on, the aperture alignment should be adjusted so that the image comes in and out of focus without moving up and down or side to side. The aperture size used was the default 30 μm. For higher quality images, a slower scan speed was used. This keeps the beam on each pixel for a longer time, allowing more electrons to be collected.

Several SEM pictures were taken at different areas of each sample, both at low and high magnifications, to get an idea of the general CRUD growth on the sample and of local CRUD morphology near and away from the sites of the induced defects. A representative area near the center of the sample was found through visual inspection. The CRUD and sedimentation amounts in the region should look similar to other areas on the sample that had been exposed to PWR water during boiling and a check for microcavities or microposts (if not a control sample) was done. Any patterns seen in where the CRUD forms or does not form on the sample could also be easily observed.

EDS, which was part of the SEM, was used for elemental analysis. X-ray analysis requires a higher beam voltage than imaging with the In-Lens and SE2 detectors does. The voltage should be 2.5-3 times the excitation voltage of the material. Since we wanted to analyze iron and nickel oxides, a beam voltage of 18 kV was selected. Iron has an x-ray with an energy of 6.266 keV and nickel has a transition energy of around 7.323 keV [84]. The electron beam striking the sample causes electrons in the sample material to become excited. When these excited electrons decay down to their ground state, they release characteristic x-rays. EDS counts the number of x-rays at a given energy, and identifies the element according to the energy.

When the FIB was used, the FIB and SEM must be aligned by setting up the eucentric axis and the coincidence point. Milling was done while the sample was tilted at 54° so that the FIB column would be prependicular to the surface and cut directly down into the sample. A working distance of 5-11 mm was used and imaging was done in the SEM since imaging in the FIB is highly damaging to the material. For milling, the initial beam current used was 1.5 nA at an accelerating voltage of 30 kV. After the first cut, several cuts were made at a lower current of 150 pA to clean off the gallium ions that had deposited on the sample. This allowed for a clearer image of the internals of the CRUD layer.

For the analysis, we wanted to know what areas had thick CRUD growth and whether the vapor chimneys would be more likely to appear at the defects or away from the defects. The SEM allowed us to look at the CRUD topology on the micrometer level, which is on the scale of vapor chimneys. The EDX system on the SEM also enabled us to determine the composition of the particles on the sample

surface in different regions. Patterns or unnatural features on the surface, such as unidentified particles, were noted and examined more closely. Areas around the defects were examined at high magnification to see if there are any differences in CRUD growth around them compared to the bulk surface. The FIB allowed for cutting the surface of the sample on the microscale to get a look inside the CRUD layer. This was done to see if the inside of the CRUD layer was the same as the surface, and if it was possible to if vapor chimneys went straight through the CRUD layer, if they twisted, or if they could be blocked off and new ones form in different areas. Image processing was done in Matlab to determine the percent of area that was relatively clean compared to the areas with CRUD deposition on various samples.

Chapter 4

Results

The results for each test will be summarized in this chapter. The experiments are organized into the following four groups:

1. Substrates with engineered microcavities ranging from 30 μm to 100 μm and control samples that underwent boiling for 1 hour (not including the time to heat up the bulk water to the water temperature setpoint) in coolant containing Fe_3O_4 and NiO concentrations of 100 ppm each.

2. 50μm, 500 μm, 800 μm pitch samples and control samples that were boiled for 1 hour with Fe_3O_4 and NiO concentrations of 50 ppm.

3. Two control samples run for 24 hours, with all other parameters held constant.

4. Samples with microposts 3 μm tall and 6 μm tall that underwent boiling for 1 hour with Fe_3O_4 and NiO concentrations of 100 ppm.

The experiments within each group are organized by microcavity pitch or micropost height and were tabulated in Table 3.2. Only a few, representative SEM images will be provided to illustrate important points.

4.1 Logomatic Data Analysis

The sample temperature, water temperature, and heat flux going through the sample were recorded in the logomatic. The values that are in the data file must be converted to actual units of measurement using the conversion factors mentioned in section 3.2.3. The temperature data showed consistent bulk water temperatures during heating. A few samples experienced a temperature excursion due to thermocouple or heater

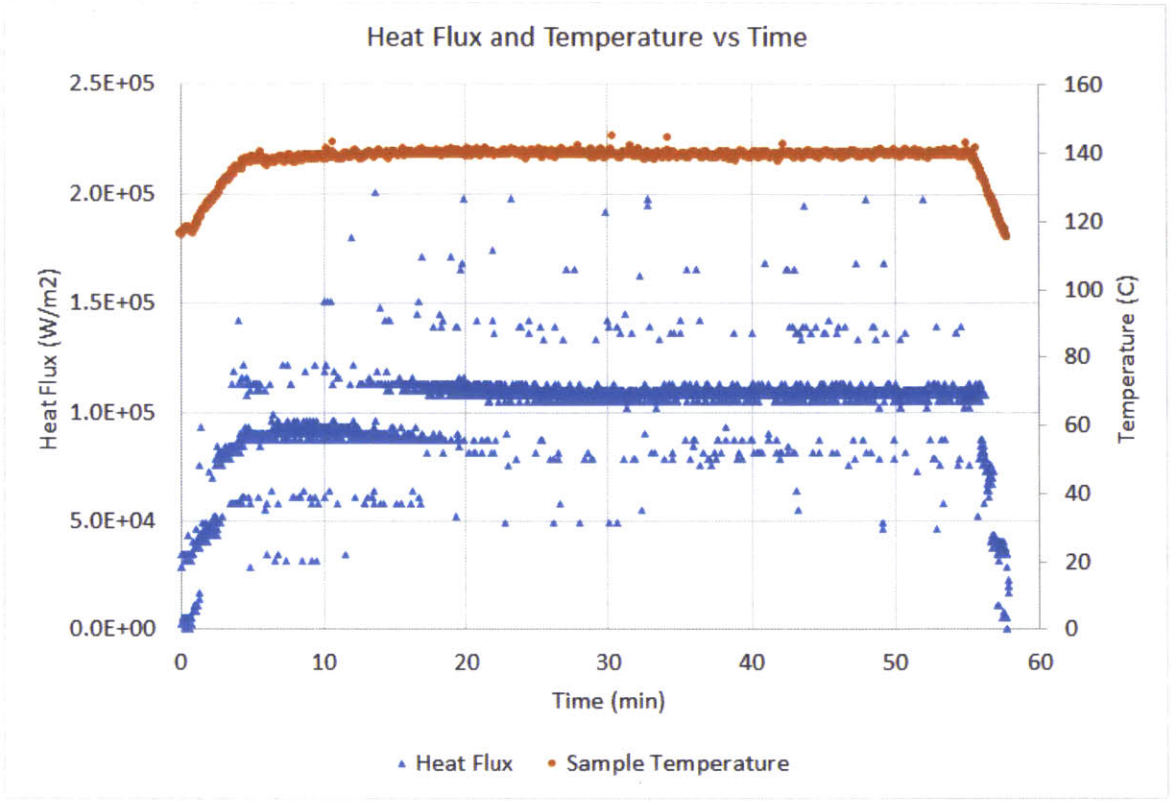

Figure 4-1: Heat flux and sample temperature versus time for a sample with 30 μm pitch microcavities. It clearly shows the temperature rising and then staying at a constant temperature of around 140°C before dropping off as the sample heater is turned off at the end of the run. The heat flux matches the temperature. Heat flux increases with increasing temperature difference between the bottom of the sample and the top of the surface (which is exposed to coolant).

controller failure. The heat flux was recorded during the runs, and the average heat flux and standard deviation for each run was calculated and recorded in Table 3.2. The pH of the simulated PWR water before and after boiling were estimated using pH strips. The pH was within a range of 6 to 8. The pH strips showed that while some of the trials had a fluid pH that stayed the same, some became slightly more basic after the experiment.

The graphs of temperature as a function of time show a rise in temperature as the sample heater is turned on. The temperature then either approaches a constant temperature, or it overshoots and drops back down, sometimes oscillating before reaching a steady temperature. An example of the first possibility, which was seen during the majority of runs, is shown in Figure 4-1. The shape of the heat flux curve usually followed the sample temperature graphs. However, the heat flux had a lot of variance due to the sample heater cycling on and off during the experiment. Despite

(a) Silicon substrate with a grid of 30 μm pitch microcavities before CRUD deposition.

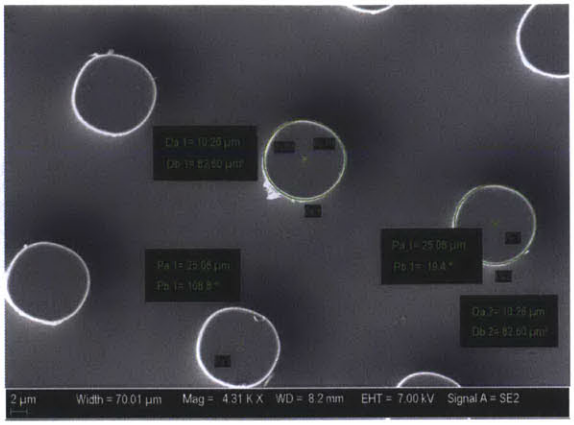

(b) A top view of a silicon substrate with 3 μm tall microposts before CRUD deposition. The microposts for this sample are on a square grid with pitches of 25 μm.

Figure 4-2: SEM images of microcavity and micropost samples before boiling.

using the same temperature setpoints and the cycle heating times each time, the heat flux differed for each run. A few of the runs experienced a temperature excursion, either due to faulty thermocouple readings that resulted in overheating, the heater controllers failing open, or dryout of the sample surface.

4.2 SEM Analysis

4.2.1 Pre-boiling SEM Analysis

SEM images of the photolithographed silicon substrates were taken before growing CRUD on them in the boiling facility for comparison with post-boiling samples. Figure 4-2a shows a clean silicon substrate with 30 μm pitch before one of the runs. The diameter of the holes were between 4-5 μm. The microcavities on the same sample were generally the same diameter, but the diameters between different samples varied, most likely due to different reactive ion etching times. The samples were fairly free of contamination after rinsing with acetone and ethanol. Most of the microcavities had no visible defects. One of the samples with microposts was observed using the SEM before boiling, shown in Figure 4-2b. The diameter of the posts were approximately 10 μm. The 3 μm tall micropost sample had a pitch of of 25 μm center-to-center, while the 6 μm tall micropost sample had a smaller pitch of 15 μm.

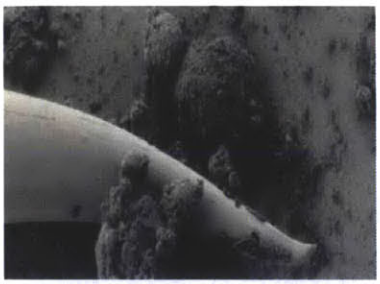

(a) Sedimentation particle before it has been moved by the needle.

(b) Sedimentation particle being rolled by needle.

(c) Sedimentation particle after being moved, still completely intact. The surface underneath was clean and showed no particles left behind.

Figure 4-3: SEM images of the process of using an OmniProbe needle to push a large particle.

4.2.2 Post-boiling SEM Analysis

4.2.2.1 Microcavity Samples, 1 Hour, 100 ppm

The samples boiled for 1 hour in simulated PWR coolant with Fe_3O_4 and NiO concentrations of 100 ppm, 10 ppm H_3BO_3, and 5 ppm LiOH included microcavity pitches ranging from 30-100 μm and samples with no etched sites. The etched sites, which are the dark holes on the images, were very clear in all the samples, even on the samples with thicker CRUD. The lighter areas are CRUD or sedimentation particles, while the darker grey is the silicon surface. The CRUD are the smaller, "softer" looking structures. The larger, denser looking particles are sediments since they are not bonded to the surface. This was confirmed in the FIB by using OmniProbe needle to push one of the large particles. The particle easily rolled, intact and without leaving any trace behind on the surface. This process is shown in Figure 4-3.

The control samples with no induced defects had about the same amount of deposition as the samples with microcavity pitches of 50 μm. Two of the control samples were similar to Figure 4-4a, where there was CRUD growth throughout the sample comparable to the amount seen in the 80 μm microcavity pitch samples. A low magnification image of one of the control samples without much deposition is shown in Figure 4-5. However, the other control sample had some regions that showed large sediments and a substantial amount of particles deposited in those regions specifically, as seen in Figure 4-4b. Only a few small areas are devoid of particles on the surface.

High magnification SEM images of each of the microcavity samples are shown in Figure 4-6. One of the 30 μm pitch samples, shown in Figure 4-6a, did not experience

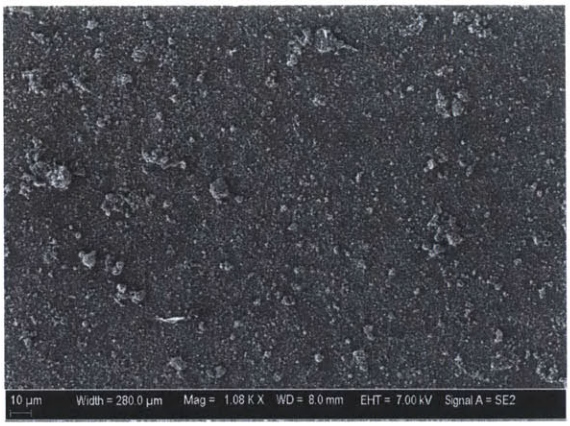

(a) Control sample that had homogeneously distributed small particles with some CRUD growth.

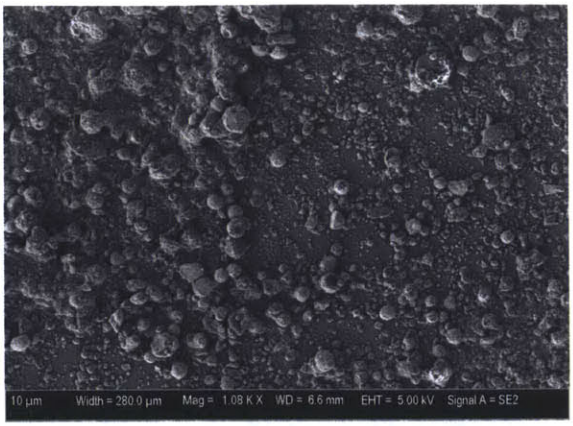

(b) Control sample that had some areas of substantial deposition with large sediments, between 10-20 μm wide.

Figure 4-4: SEM images of two different control samples, both boiled for 1 hour with coolant containing 100 ppm of Fe_3O_4 and NiO. All images are at the magnification of 1,080×.

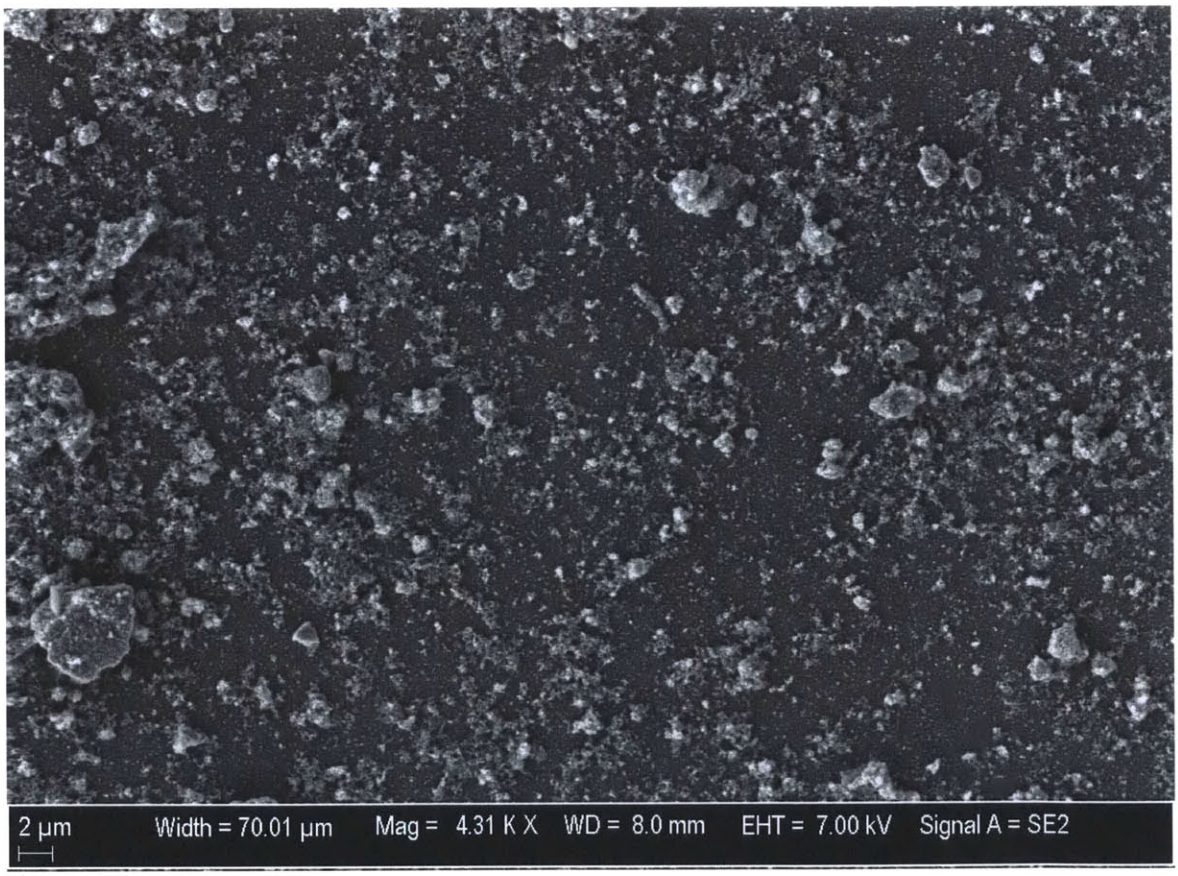

Figure 4-5: Control sample boiled for 1 hour with coolant containing 100 ppm of Fe_3O_4 and NiO. It shows a low amount of CRUD growth compared to some of the samples with induced microcavities.

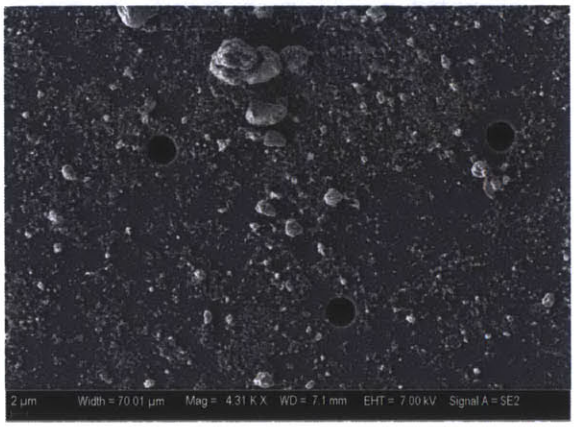

(a) 30 μm microcavity pitch sample. It showed the least amount of particle deposition among the microcavity and control samples, but had larger sediments than the wide microcavity pitch samples.

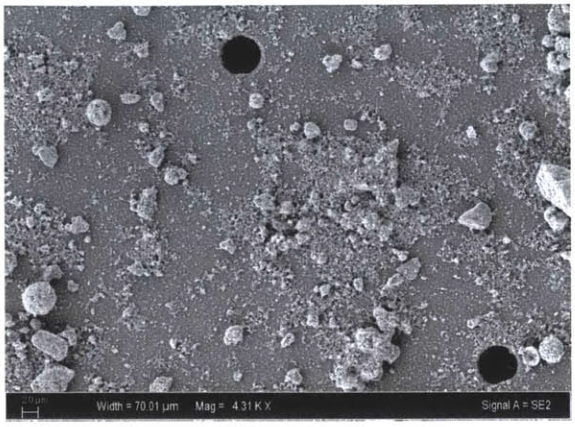

(b) 50 μm microcavity pitch sample.

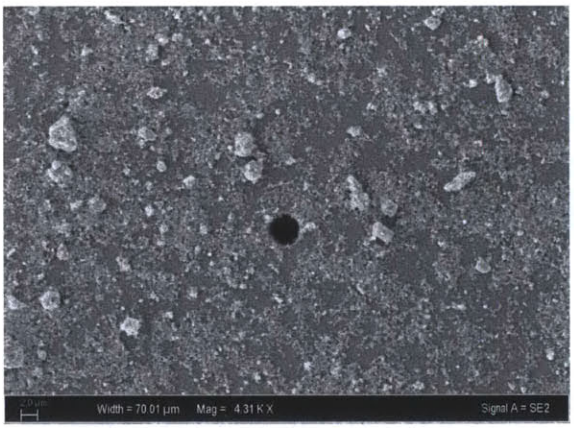

(c) 80 μm microcavity pitch sample.

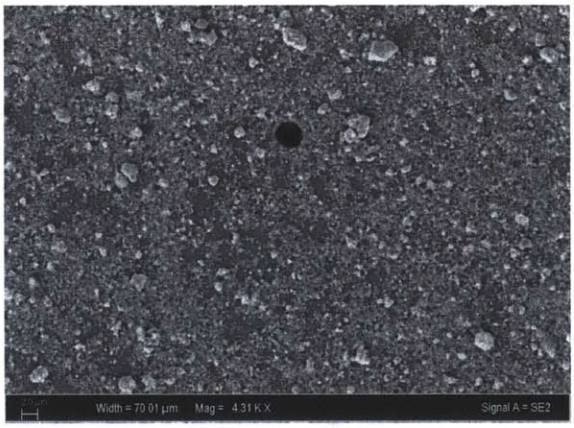

(d) 100 μm microcavity pitch sample. It showed the most deposition out of the 30 μm, 50 μm, and 80 μm samples boiled under the same conditions.

Figure 4-6: SEM images of samples boiled for 1 hour with coolant containing 100 ppm of Fe_3O_4 and NiO, 10 ppm of H_3BO_3, and 5 ppm of LiOH. All images are at the same magnification of 4,310×, with each image showing an area of 70 μm × 52.5 μm.

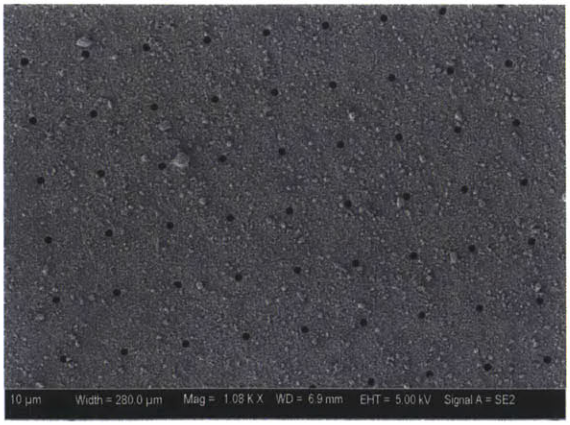

(a) 30 μm microcavity pitch sample that had a substantial amount of CRUD throughout the entire surface.

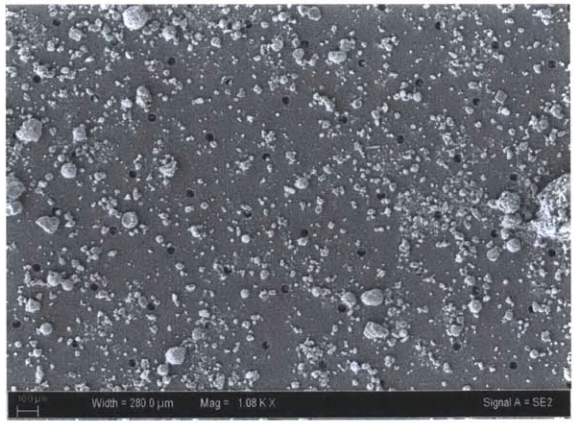

(b) 30 μm microcavity pitch sample where the sample heater shut off for 5 minutes before resuming during boiling. The sample had low amounts of CRUD, but contained large sediments on the surface.

Figure 4-7: SEM images of 30 μm microcavity pitch samples after boiling for 1 hour. They show conflicting results. Both images are at the magnification of 1,080 $\times$.

much CRUD growth, but did have a relatively large amount of of sedimentation. The second 30 μm pitch sample showed the opposite result, containing an abundant amount of CRUD throughout the surface, shown in Figure 4-7a. The last of the 30 μm pitch sample, shown in Figure 4-7b, had almost no CRUD growth on it and only larger particles that settled onto its surface, but it did experience anomalous conditions. During boiling, the sample heater had lost power for 5 minutes. The experiment was resumed after power was recovered and extended to account for the heating time lost.

The 50 μm pitch samples had a relatively small amount of CRUD growth, consistently less than the 80 μm and 100 μm pitch samples. The sedimentation particles on the 50 μm pitch sample were comparable in size to the 30 μm pitch sample that had experienced similar CRUD growth. The 80 μm pitch samples were more homogeneously covered in CRUD than the lower pitch samples. The 100 μm pitch samples were similar to the 80 μm pitch samples, but generally had more CRUD.

Larger sedimentation particles were seen more frequently on microcavity samples that had less CRUD growth. For example, the 30 μm and 50 μm pitch sample had many sedimentation particles with diameters around 5-10 μm as shown in Figure 4-8a. The largest particles in the 80 μm and 100 μm pitch samples usually had a diameter around 3-7 μm, shown in Figure 4-8b, but these were also seen less frequently.

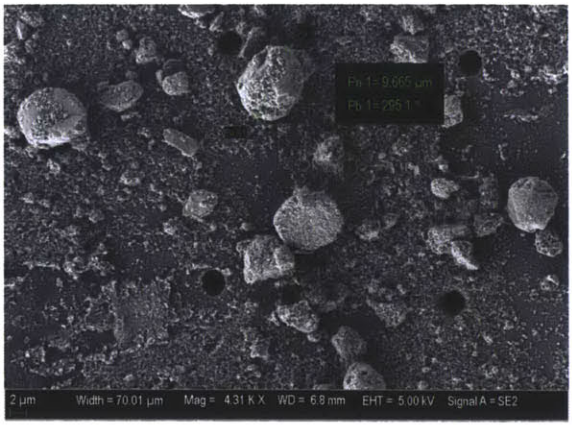

(a) 30 μm pitch sample at 4310×. The largest particles are around 10 μm in diameter.

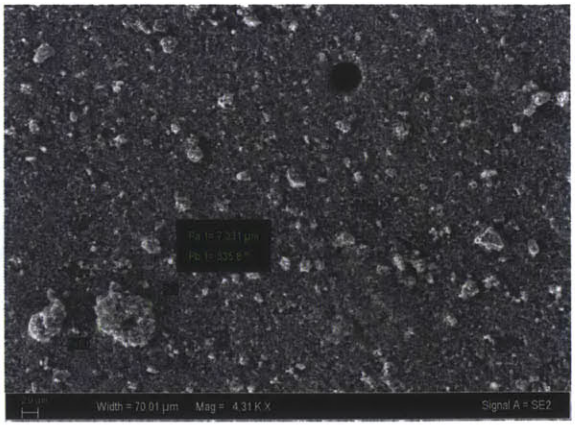

(b) 80 μm pitch sample at 4310×. The largest particles are around 7 μm in diameter.

Figure 4-8: Measurement of large sedimentation particles on samples after boiling.

4.2.2.2 Microcavity Samples, 1 Hour, 50 ppm

Samples with various grids of microcavities were also boiled for 1 hour with smaller Fe_3O_4 and NiO concentrations of 50 ppm in the simulated PWR coolant. Figure 4-9 shows both of the 50 μm pitch samples. One of the 50 μm pitch sample, shown in Figure 4-9b, heated up to 180°C over a period of 12 minutes in the middle of the run before the heater was cycled. This sample clearly shows a pattern of cleaner and dirtier areas. The 50 μm pitch sample that did not experience this temperature excursion (see Figure 4-9a) had more particles present on the surface, but also had a faint, but similar pattern.

Figure 4-10a shows the 500 μm sample, which had more particulate deposition than the 50 μm. There were areas of thicker CRUD growth as well as cleaner areas, but no clear pattern was observed. The 800 μm pitch sample, shown in Figure 4-11, had the modal pattern as well. The clear areas were approximately 50 μm wide, and ribbons of particulate deposition were approximately 10 μm wide. Acquiring a good image of CRUD deposition on the second 800 μm pitch sample was unsuccessful due to charging effects in the SEM. The control sample that was run at this concentration of 50 ppm Fe_3O_4 and NiO in the simulated PWR coolant, shown in Figure 4-10b, was relatively homogeneously covered in particles, unlike the samples with grids of microcavities. In one of the control samples, while most of the surface was covered with a layer of CRUD, one corner had many large clean areas. Many were in the shape of ellipses, as large as 10 μm wide, as shown in Figure 4-12.

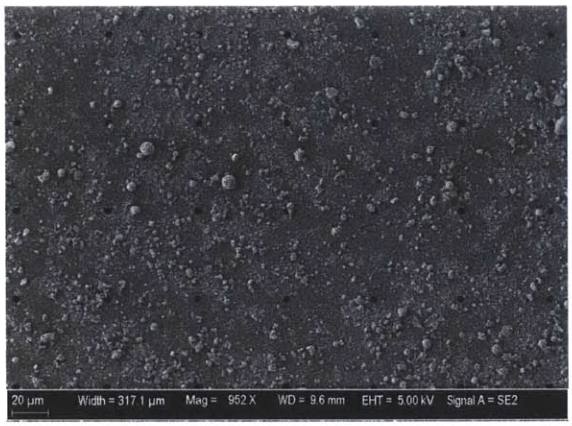

(a) 50μm microcavity pitch sample at a magnification of 952×.

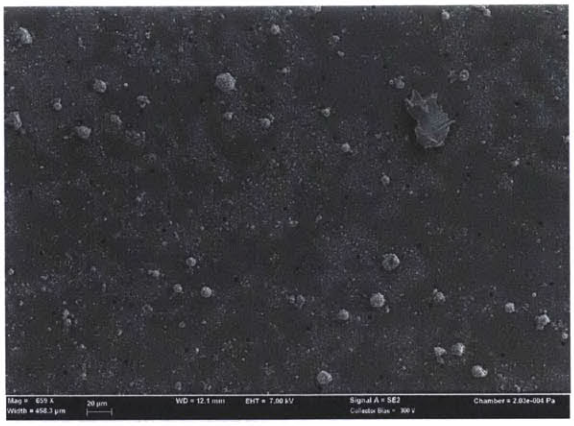

(b) 50μm microcavity pitch sample that went up to 180°C in the middle of a 1 hour run. A modal pattern can be clearly seen with regions of more or less particle deposition. Magnification is 659×.

Figure 4-9: SEM images of 50 μm microcavity pitch sample boiled for 1 hour with coolant containing 50 ppm of Fe_3O_4 and NiO.

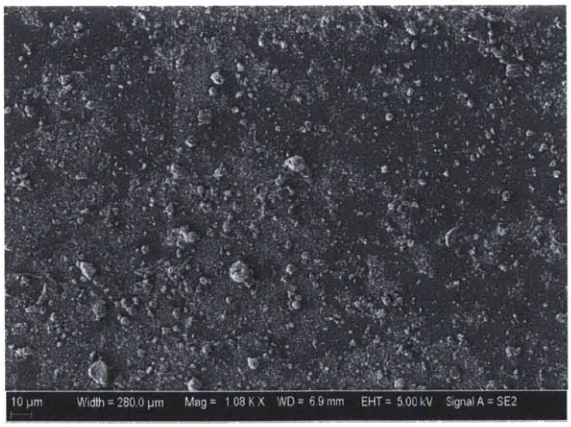

(a) 500 μm microcavity pitch sample.

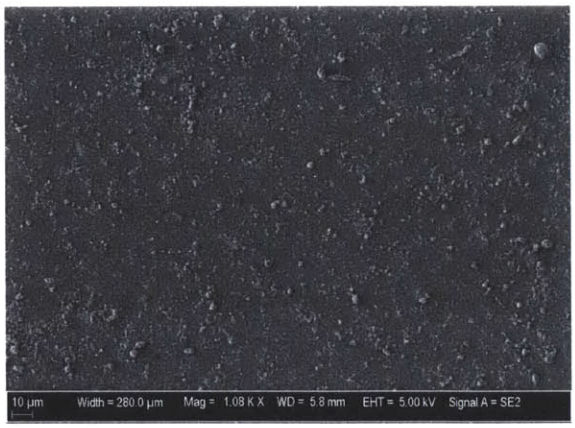

(b) Control sample which shows more homogeneous deposition than the samples with microcavities boiled under similar conditions.

Figure 4-10: Samples boiled for 1 hour with coolant containing 50 ppm of Fe_3O_4 and NiO at magnifications of 1,080×.

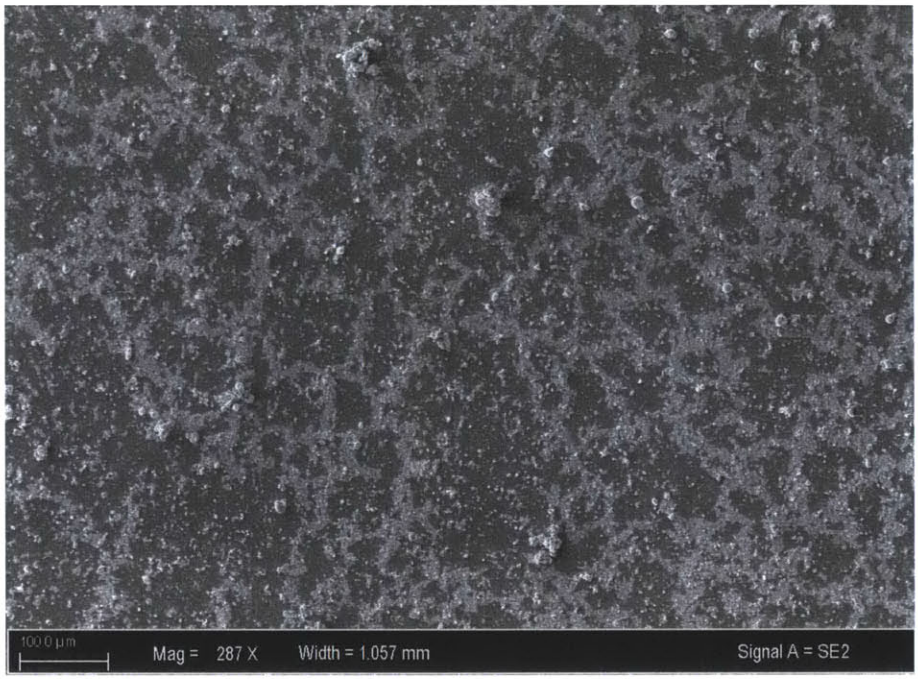

Figure 4-11: SEM image of a 800 μm pitch microcavity sample boiled for 1 hour with coolant containing 50 ppm of Fe_3O_4 and NiO. A modal phenomena was observed with alternating areas of more and less deposition.

4.2.2.3 Control Samples, 24 Hours, 100 ppm

One control sample that underwent boiling for 1 hour in PWR water simulant with Fe_3O_4 and NiO concentrations of 100 ppm is shown in Figure 4-13a. There is more CRUD growth and sedimentation than the any of the other control samples except for the control sample run for 1 hour that experienced some areas with large sedimentation and deposition around those areas. The other control sample boiled under these conditions showed some unusually clean areas. These clean regions contained some CRUD, which frequently grew in a modal pattern. There was an unnaturally circular boundary between the cleaner surface and the region where there was at least small amounts of deposition over the entire surface, as seen in Figure 4-13b.

4.2.2.4 Micropost Samples, 1 Hour, 100 ppm

The SEM images of the micropost samples are shown in Figures 4-14. The 3 μm tall microposts with pitches of 25 μm had a substantial amount of CRUD, more than any of the plain silicon or the samples with photolithographed microcavities that were run with the same conditions. Some areas were relatively clean, with the silicon surface visible. In areas that did have CRUD covering the surfaces, a lot of particles built up

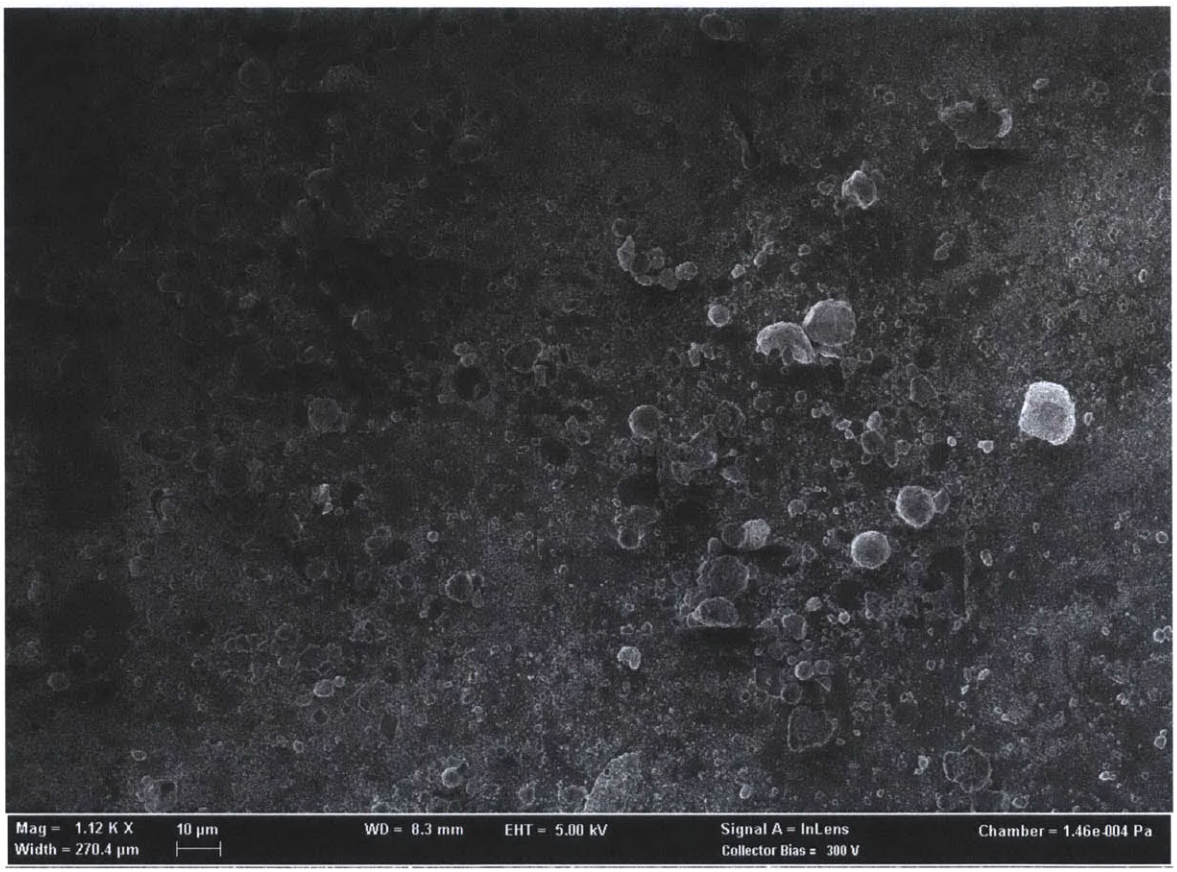

Figure 4-12: SEM image of one corner of a control sample after boiling that shows some clean areas, around 5-10 μm wide, on the surface. This was not observed in the rest of the sample.

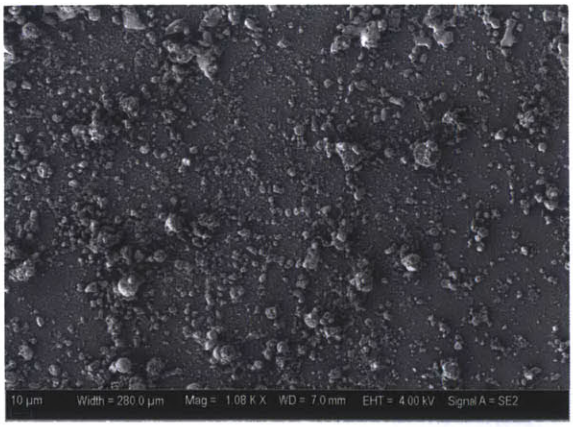

(a) Control sample showing more CRUD growth than on the control and microcavity samples boiled for a shorter amount of time.

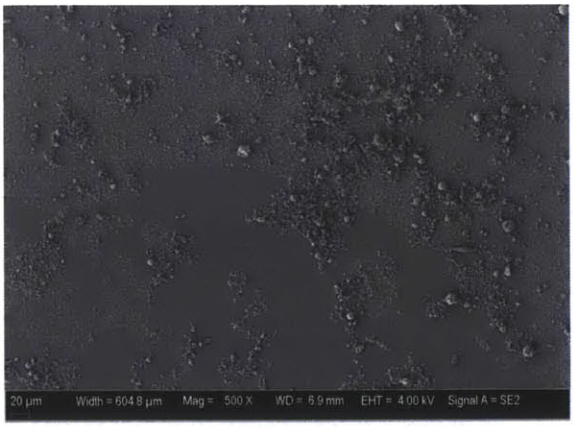

(b) Control sample run for 24 hours with coolant containing 100 ppm of Fe_3O_4 and NiO. This sample showed an unusual boundary between the mostly clean surface with regions of CRUD, and the rest of the surface that was mostly covered with particles.

Figure 4-13: SE images of control samples boiled for 24 hours with coolant containing 100 ppm of Fe_3O_4 and NiO.

upon themselves, sometimes filling up the spaces between the microposts completely and growing on top of the microposts.

The 6 μm tall microposts with pitches of 15 μm experienced a significant amount of deposition compared to the microcavity samples, but the surface had much less CRUD and sedimentation than the 3 μm tall microposts. One interesting area near the edge of the 6 μm tall micropost sample showed particles growing and linking up just on top of the microposts. There were no particles are seen on the surface underneath these areas, though the surrounding areas had CRUD growth both on top of the microposts and on the surface below. Figure 4-15 shows this region.

4.2.3 Post-boiling EDS Analysis

The EDS analysis for samples in locations where there seemed to be thick CRUD growth showed both nickel and iron were present. Figure 4-16 is a SEM image of an area near a microcavity with CRUD deposition that was analyzed using EDS. The spectrum from using EDS with an beam voltage of 18 kV indicated the presence of silicon, iron, nickel, and oxygen on the surface, as shown in Figure 4-17. Iron was present at 13.6 at% and nickel was lower at 8.0 at%. Two iron and two nickel peaks showed up since characteristic x-rays from both their K and L shells were detected. Oxygen made up 33.8 at% of the material, most likely in the form of nickel and iron

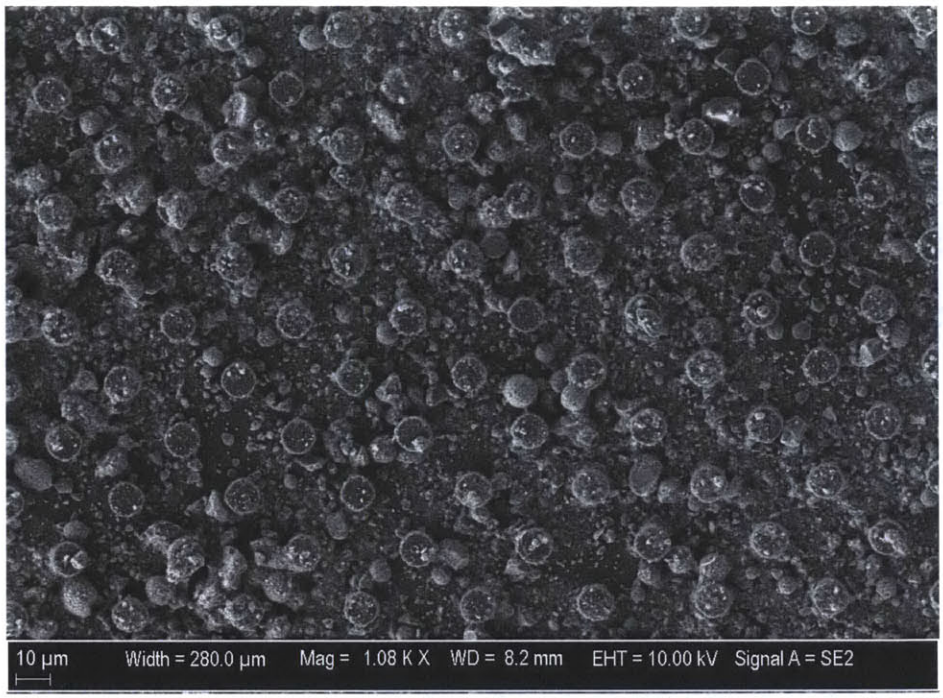

(a) Sample with microposts with a height of 3 μm and pitches of 25 μm. The microposts are on a grid with pitches of 25 μm. Most of the surface, both on top of and between the microposts, was heavily covered with CRUD.

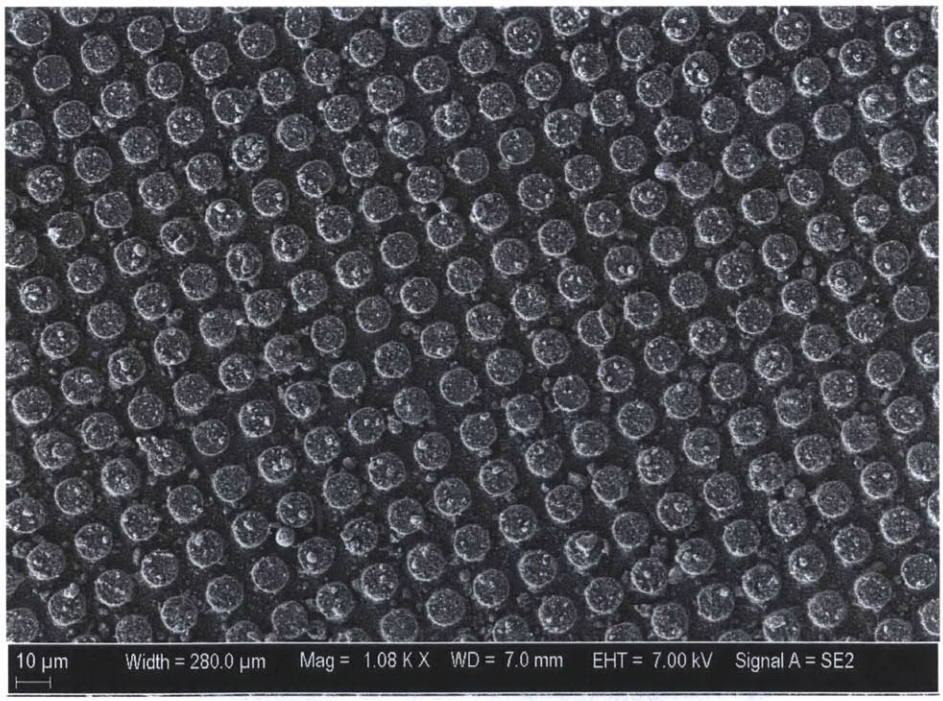

(b) Sample with microposts with a height of 6 μm and pitches of 15 μm. The microposts are on a grid with pitches of 15 μm. Most of the surface, both on top of and between the microposts, was covered with CRUD.

Figure 4-14: Micropost samples after boiling for 1 hour with coolant containing 100 ppm of Fe_3O_4 and NiO. Both images are at a magnification of 1,080$\times$.

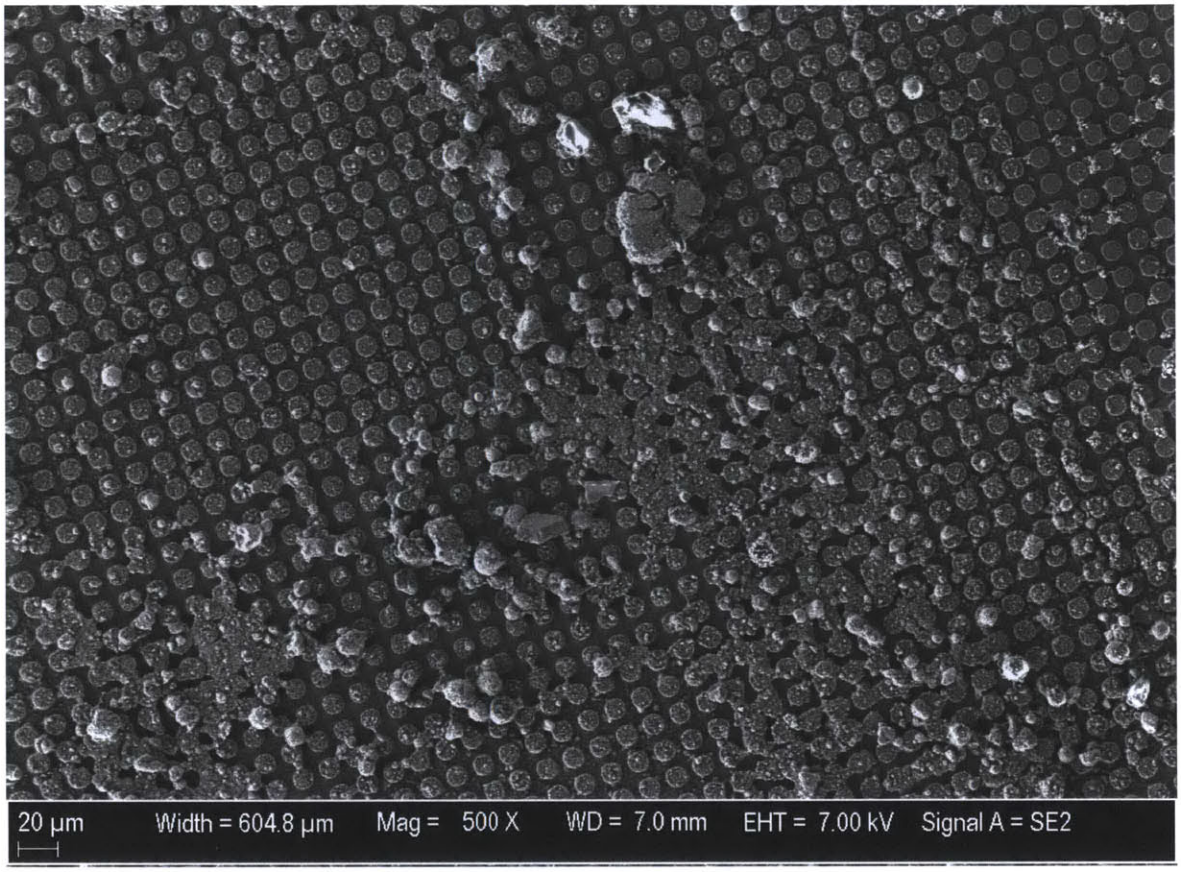

Figure 4-15: SEM image of the region in the 6 μm tall micropost sample that had particles above the microposts, but no particles in the area beneath them. The surrounding regions have small particles both on top of the microposts and on the lower surface. The right side of the image that is devoid of particles is most likely where the rubber gasket was pressed down on the sample during boiling.

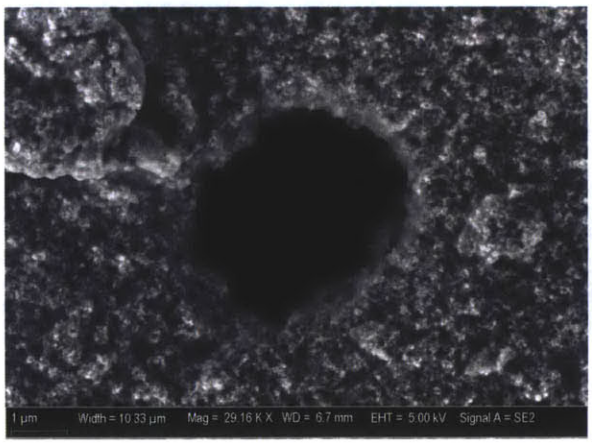

Figure 4-16: Area of thick CRUD growth near a microcavity that was used for EDS analysis.

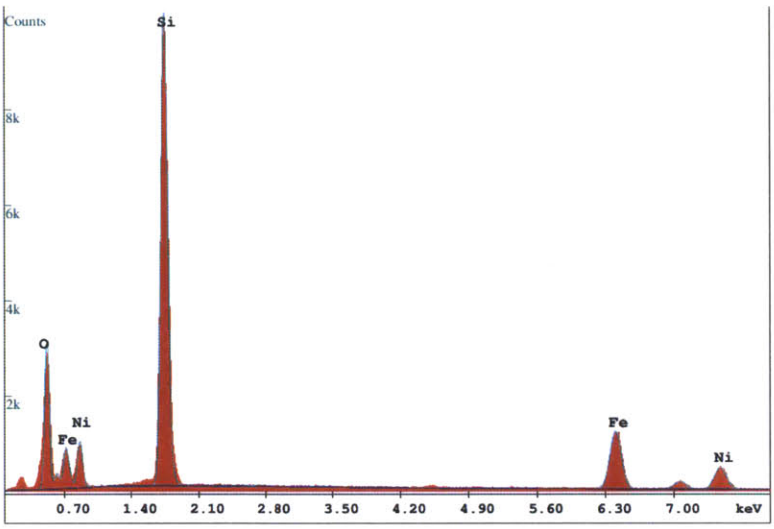

Figure 4-17: EDS spectrum of an area of thick CRUD growth near a microcavity. An accelerating voltage of 18 kV was used and resulted in determining the presence of iron, nickel, oxygen, and silicon on the surface.

oxides. Further EDS analysis revealed that the particles rounder in appearance were nickel oxides, while the more angular particles were iron oxides. No boron or lithium was observed with EDS analysis, most likely because if any did precipitate out in the CRUD layer, they were in too low of a concentration to be separated from the background noise. The coolant simulant used for these experiments contained very low concentrations of H_3BO_3 and LiOH.

In a few samples, what seemed to be cubic crystalline structures were found on top or slightly imbedded into the CRUD layer. EDS analysis was done on one of these structures and it was found to contain chlorine and potassium in addition to the expected silicon, iron, nickel, and oxygen. The crystals are most likely potassium chloride salt. The area in which EDS analysis was done is shown in Figure 4-18, and the spectrum is shown in Figure 4-19.

4.3 FIB Analysis

Ion milling was used on the 3 μm tall micropost sample in a region of thick CRUD. Figure 4-20 shows SEM images of the region at a vapor chimney that was milled using gallium ions. The cross-sectional view of the CRUD shows several pores and part of capillaries that 100-300 nm wide that assist in bringing water into the CRUD layer. One region, in Figure 4-20b, showed a cavity in the CRUD about 1.6 μm wide. Regions of solid light grey that were not part of the silicon substrate were areas that

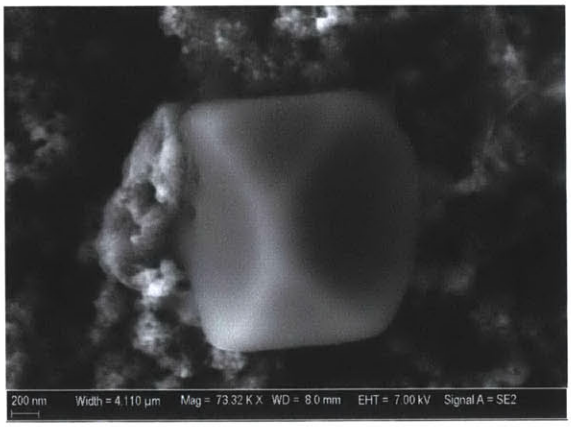

Figure 4-18: Image of a crystal structure that is present in some of the samples after CRUD growth, most likely salt.

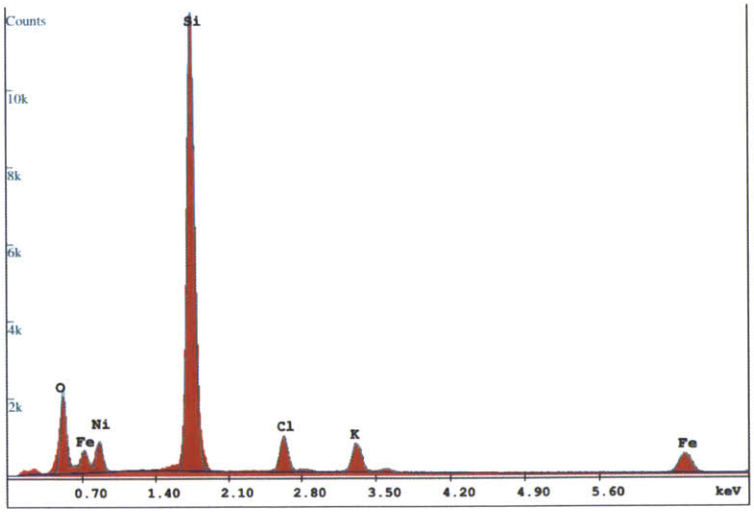

Figure 4-19: EDS spectrum of the foreign crystalline structure after growing CRUD on a sample. Chlorine and potassium were present in addition to the expected elements.

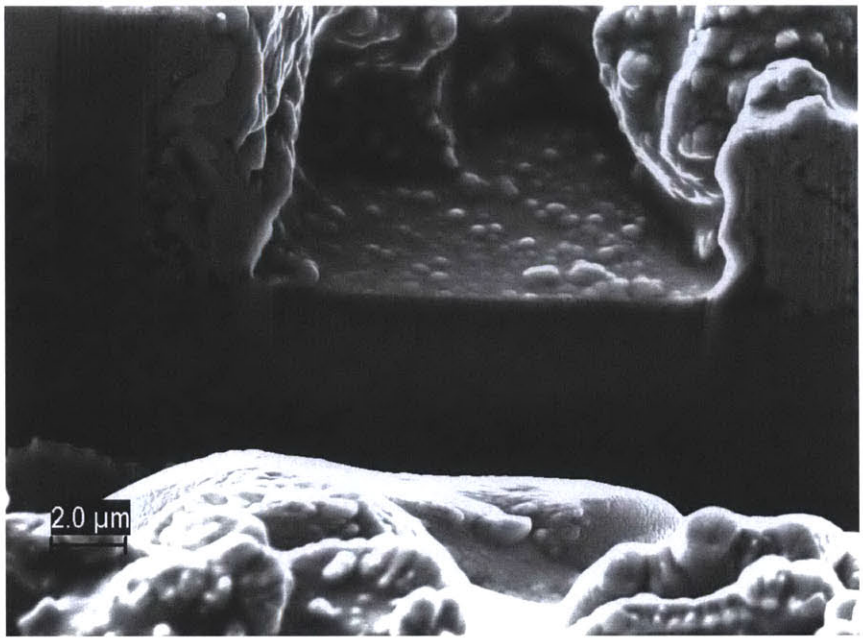

(a) Cross-sectional view of a vapor chimney to the right of a silicon post.

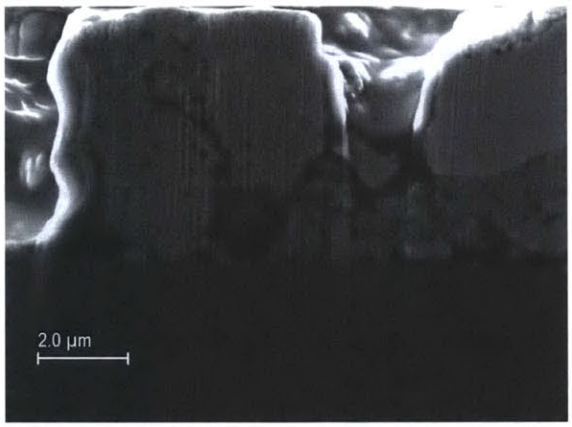

(b) Cross-sectional view of a CRUD particle with small capillaries and a cavity. The edge of the vapor chimney is on the left side.

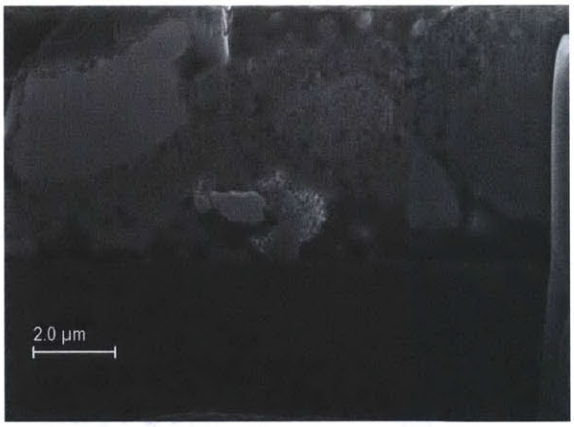

(c) Cross-sectional view of a CRUD particle. Pores can be seen in the CRUD. The solid light grey areas did not have the gallium ions cleaned off of them, so they do not show the interior of the CRUD.

Figure 4-20: Cross-sectional SEM images of 3 μm tall micropost after boiling.

were covered with gallium ions, deposited during the milling process, that had not been cleaned off. Cross-sectional images of other samples milled using the FIB showed a similar porous structure in the CRUD.

4.4 Image Analysis

Representative images of samples that were boiled for 1 hour with 100 ppm of Fe_3O_4 and NiO in the coolant, shown in Figure 4-6, were used for analysis in Matlab. The code is attached in Appendix A. The code was used to manually draw circles around clean areas, areas with CRUD, sediments, or microcavities, and the areas of the drawn circles were then calculated. The total image area analyzed in this way was 3.4 mm^2 for each sample. For the control sample, 30 μm microcavity pitch, and 50 μm microcavity pitch samples, which had many clean areas, the clean area was calculated by taking the difference between the total area and the area of the CRUD, sediments, and microcavities. Figure 4-21 shows the end product of the 30 μm microcavity pitch sample after analysis of the original image (see Figure 4-6a).

The percentage of clean area is constant until around 50 μm, at which point it decreases with increasing microcavity pitch, as shown in Figure 4-22a. The control sample's percentage of clean area was comparable to the 30 μm and 50 μm microcavity pitch samples. The percentage of crudded area is similar for the control sample and the 30 μm and 50 μm microcavity pitch samples (see Figure 4-22b). For microcavities pitches larger than 50 μm pitch, the percentage of crudded area increases with increasing microcavity pitch. The areas covered by sediments and microcavities (if present) were excluded from the calculation of the clean and crudded areas. It was unknown whether CRUD grew underneath the sediments or whether it would have been a clean area. No CRUD was seen covering any microcavity sites, however, closer examination of the microcavity would be needed to determine if any CRUD grew inside the microcavities.

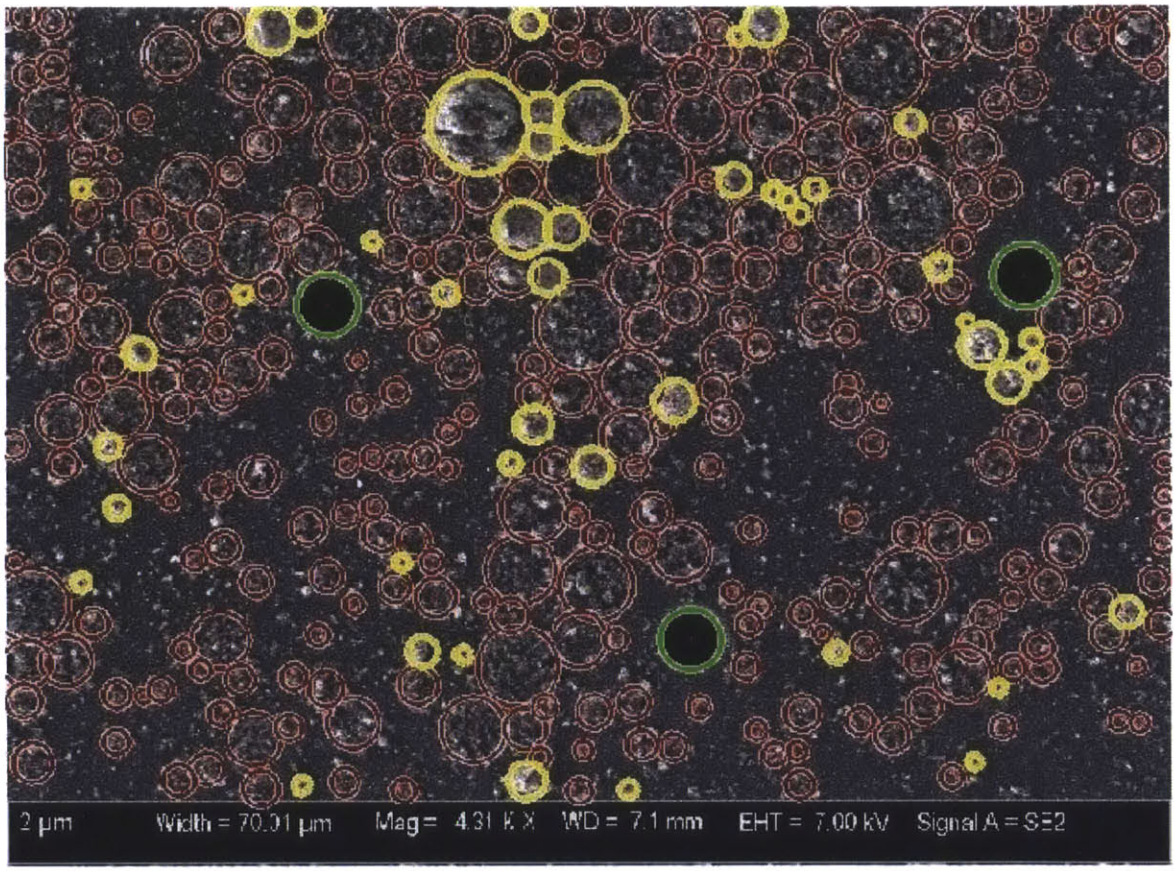

Figure 4-21: Circled areas of CRUD (red), sediments (yellow), and microcavities (green) for a 30 μm microcavity pitch sample after boiling using Matlab.

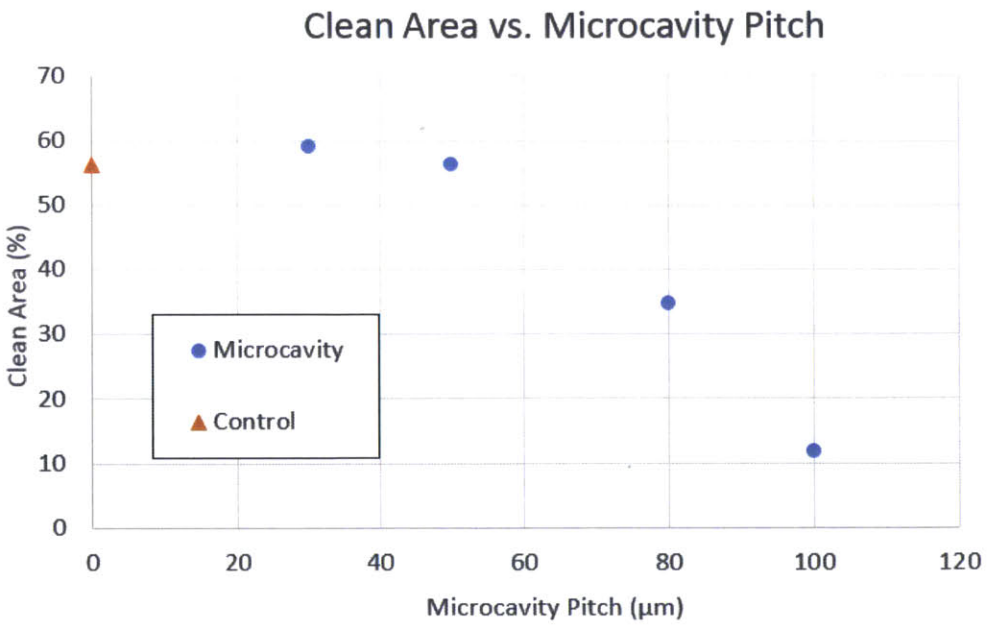

(a) Graph of the percentage of clean area on the sample as a function of the microcavity pitch.

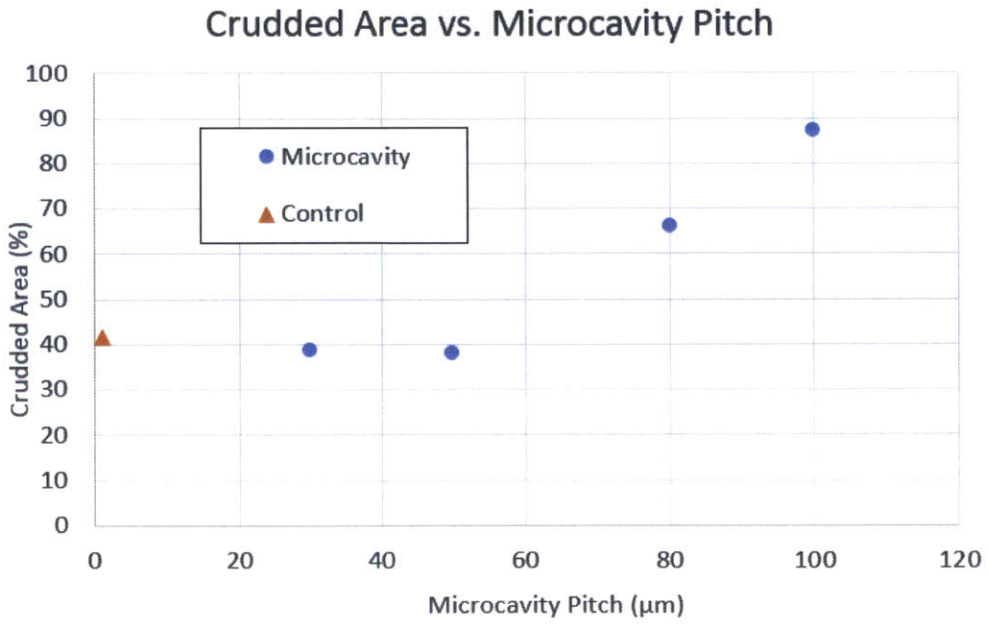

(b) Graph of the percentage of crudded area on the sample as a function of the microcavity pitch.

Figure 4-22: Graphs of the percentage of clean and crudded areas on the sample as a function of the microcavity pitch (blue circles). The control sample (orange triangle) was also included. Sediments and microcavities were excluded from the calculation of the clean and crudded areas.

Chapter 5

Discussion

5.1 Effects of Surface Modification on CRUD Growth

It was originally hypothesized that surfaces with more fabricated microcavities or microposts (i.e., smaller pitches between etched sites) would experience more boiling, and that this would precipitate out more CRUD since solutes would concentrate at the edge of the bubbles as water evaporated. It was postulated that vapor chimneys were likely to be found near defects, such as at the microcavities or the base of the microposts, since they would serve as bubble nucleation sites. What was found, as discussed in further detail in this section, was that microcavities spaced closer together can actually inhibit formation of a CRUD layer. The micropost samples, on the other hand, seemed to promote CRUD growth. The results from the previous section will be discussed, organized by microcavity and micropost samples.

5.1.1 Microcavity Samples

Most areas exhibited increased CRUD growth with increasing microcavity pitches. The modal phenomena observed more often on the lower-pitch samples, such as the 30 μm and 50 μm microcavity pitch samples, may have come about due to resonant modes produced by the forces of bubbles collapsing on the surface of the sample. This modal phenomena was very similar to cymatics, which occurs when a surface vibrates at some resonance, resulting in the particles on the surface arranging themselves in a pattern. Bubbles tend to nucleate at microcavity defects, but the subcooled water could cause condensation, resulting in bubble collapse. In addition, if the local pressure becomes too high, the bubble will implode. For example, the change in pressure could be a result of the coolant being pumped into facility, entering a couple cen-

timeters above the sample surface. When the bubble implodes, the surrounding fluid rushes into the space the bubble used to be, impinging on the surface and causing a shockwave outwards [85]. As mentioned in section 2.3.1.2, high enough shear forces can remove fouling layers. The force from the shockwave could potentially move particles away from the bubble collapse site. From Figure 4-9b, most of the microcavities were in cleaner areas rather than along the path of the settled particles, supporting the theory that the bubbles nucleate at the microcavities and the shockwave moves outward from there.

The areas where particles settled on the surface would likely be where competing forces were in equilibrium. Regions that were clear of particles had enough net force in one direction to move particles away from the area. This is similar to cavitation–the process of vapor forming and bursting–which has been observed in pumps, flow regulation devices, and propellers, which experience changes in pressure [86, 87]. The difference is that our vapor formation comes from increasing vapor pressure by increasing temperature, whereas the nucleation of bubbles in cavitation is from a pressure drop in the fluid. However, the effect of the collapsing bubble is the same. The cavitation force is enough to overcome the adhesion forces between particles and the surface. In fact, cavitation is used as a ultrasonic cleaning technique, though it has the disadvantage of potentially damaging the surface [88, 89]. It is expected that in real reactors, the higher pressure would result in smaller bubble sizes, and this bubble collapse effect would be on a smaller scale.

It is interesting to note that the 800 μm pitch sample where this modal phenomena was also observed, shown in Figure 4-11, had clear areas that were approximately 50 μm wide, and ribbons of particulate deposition were approximately 10 μm wide. This may indicate that there is a maximum threshold, which is around 50 μm, in which this modal phenomena occurs under our boiling conditions. The samples with more space between induced microcavity sites had more CRUD growth, possibly because the sites were not close enough to have the forces from bubble collapse interfere with each other. The exception would be if bubbles nucleated on the surface without the help of the microcavities frequently enough to produce this phenomena, which may be what happened in the 800 μm pitch sample.

Hysteresis most likely plays a large role on formation of CRUD. If boiling sites do occur on a sample, they may serve to continue to promote bubble nucleation at those sites, resulting in a large amount of CRUD deposition on the surface. However, if active boiling sites are not established on the smooth surface, then less CRUD will precipitate out and the surface will be relatively clean. This could explain the differing

results in CRUD formation on the control samples, shown in Figure 4-4. The 80 μm and 100 μm pitch microcavity samples, on average, experienced more CRUD growth than the control samples boiled for 1 hour in coolant containing 100 ppm Fe_3O_4 and NiO. This may be due to the microcavities serving as nucleation sites and promoting subnucleate boiling on the surface. As discussed in section 2.1, solutes precipitate out near edges of bubbles where they are attached to the surface. An initial CRUD layer can further encourage particles in solution to deposit on the surface due to adhesion forces between the particles and the increased surface area since CRUD has a higher roughness than the clean surface. Thus, the presence of microcavities can both promote CRUD deposition and, at certain pitches and with the right heat flux conditions, the shockwaves from bubble collapse can force CRUD out of the local region. The trend of decreasing clean areas with increasing microcavity pitch (see Figure 4-22) should be verified with additional experiments.

Samples with less CRUD growth tended to have larger particles that had settled onto the surface. It is suspected that the larger particles occur due to agglomeration of nickel and iron oxides in the fluid that later settle onto the surface due to gravitational forces. Agglomeration can occur due to Brownian motion bringing particles together that stick due to the attractive van der Waals forces between them. This results in smaller particles adhering to each other and collecting to form a larger cluster [6, 38]. It is unknown whether the particles settled down as heating stopped and the water was drained, or if sedimentation would still occur even if the water remained circulating.

Vapor chimneys, when present, were seen in similar areas rather than being homogeneously distributed. Many of the samples with induced microcavities and some of the control samples had areas with no deposition, making it difficult to tell where vapor chimneys were forming. A thicker CRUD layer must be grown to clearly see vapor chimneys. Figure 5-1 has two vapor chimneys circled in red that are 7 μm apart. This may be due to the presence of conditions beneficial to vapor chimney formation in that area, such as the amount of heat flux. In addition, bubbles often come from existing vapor cavities [90]. Bubbles can be pinched off into two bubbles, creating a second active nucleation site nearby and enhancing vapor chimney formation. The edges of the samples showed particularly interesting characteristics, such as the edge of the control sample shown in Figure 4-12. The clean areas on that sample may be vapor chimneys that occurred due to boiling in those locations. Boiling was observed during many of the experiments to occur preferentially near the edges of the sample, at the interface between the substrate and the rubber gasket above it. This is likely

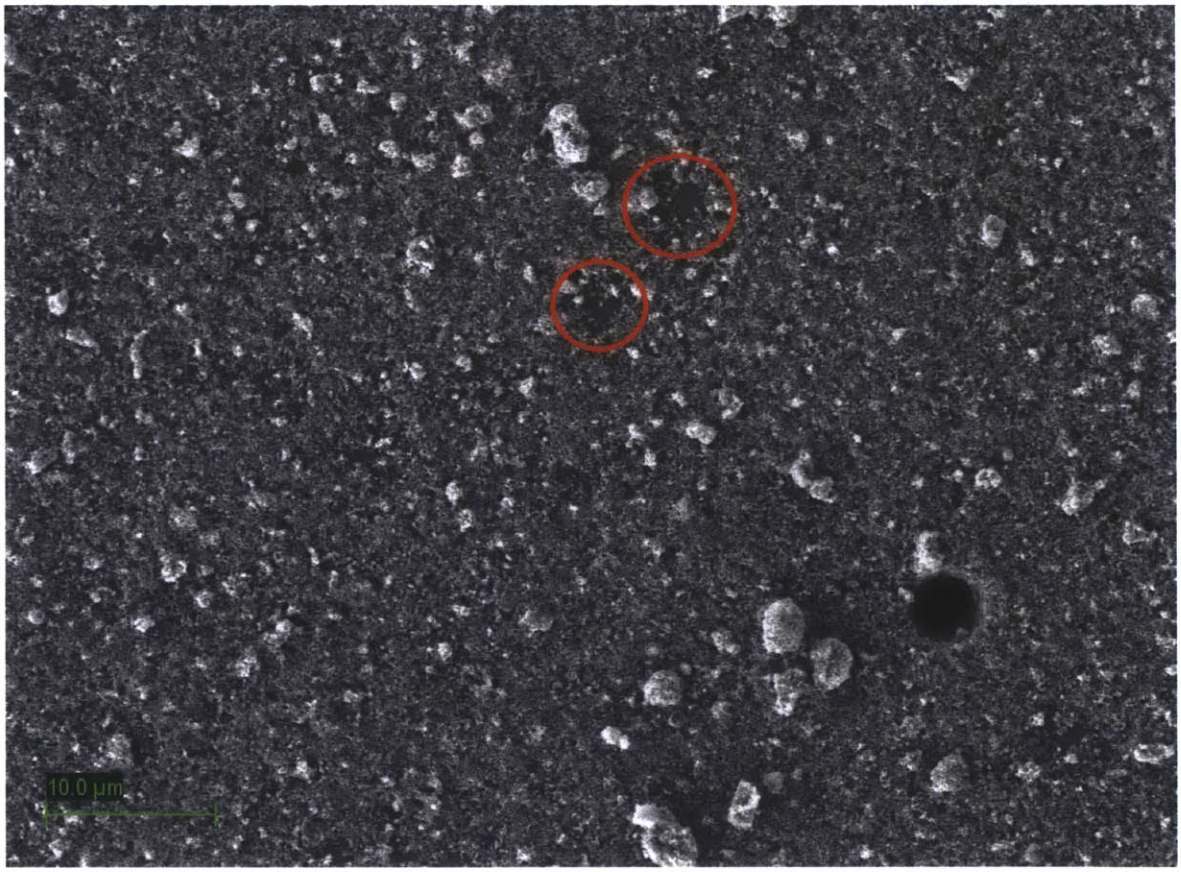

Figure 5-1: A region of an 80 μm microcavity pitch sample with thick CRUD growth after boiling for 1 hour with coolant containing 100 ppm of Fe_3O_4 and NiO. Two red circles show where the vapor chimneys are forming, about 7 μm apart.

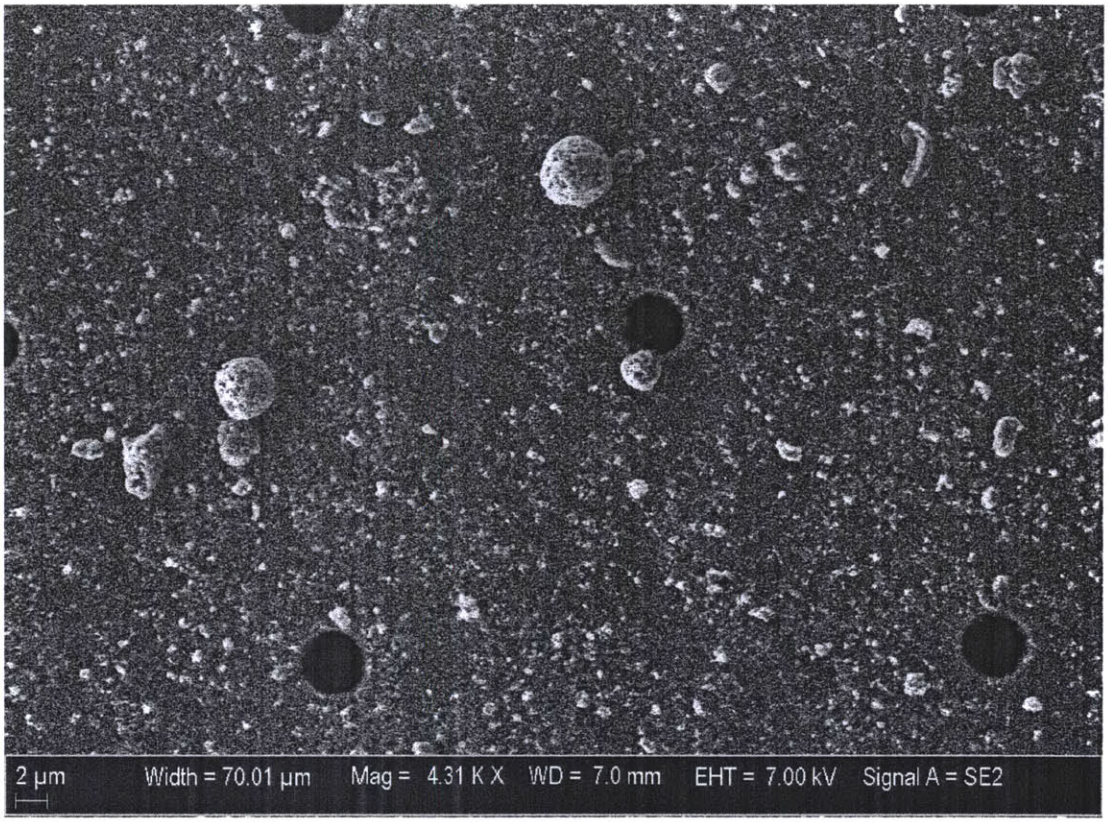

Figure 5-2: SEM image of a 30 μm microcavity pitch sample after boiling for 1 hour with coolant containing 100 ppm of Fe_3O_4 and NiO. There is a ring of CRUD around the microcavities, though the surrounding area less than one micrometer away may be clean of CRUD.

due to vapor more easily nucleating in the cracks between the mated surfaces than on a smooth surface, such as nucleating from gas pockets between the two surfaces [91].

The majority of induced microcavities experienced a ring of CRUD around them, whether the rest of the sample had substantial CRUD or not. Figure 5-2 shows this effect clearly on one of the 30 μm microcavity pitch samples which had a concentration of particles, sometimes just a few hundred nanometers wide, around the microcavities while slightly further from this area, there were places with less particles. This effect was harder to observe on samples that had substantial CRUD growth since there are no clean areas nearby, but a slightly higher build-up around the microcavities could be seen. This supports the theory that microcavities serve as nucleation sites, and that CRUD formation is promoted at bubble attachment points.

The samples boiled in PWR water simulant at 50 ppm Fe_3O_4 and NiO had less

CRUD than the samples boiled in simulant with 100 ppm Fe_3O_4 and NiO. This is expected as the amount of fouling will decrease when the system has less particulates available for deposition. The control samples that underwent boiling for 24 hours were expected to have significantly more CRUD growth than the shorter experiments, with all other parameters held constant, due to increased time for particulates to come in contact with the surface.

5.1.2 Micropost Samples

The 3 μm tall micropost samples at pitches of 25 μm were the most heavily crudded samples. It has been observed in several studies that increased contact area increases fouling, as previously discussed in section 2.1. The increased surface area means more particles will contact the surface through impaction. There may also be increased sticking probability due to the the posts "being in the way" and trapping particles. As the particles build up between the posts, the rougher surface they form makes it even easier for particles in the fluid to impact and stick to the particles on the surface, thus building up more in those regions. In the areas of the sample that had CRUD, there was a very thick layer, piling up as tall as the microposts themselves.

The 6 μm tall, 15 μm pitch micropost samples showed less CRUD than the 3 μm tall micropost samples. Though the former had a larger surface area, it also experienced a lower heat flux than the latter (Table 3.2). This result indicates that perhaps surface area is not the dominating effect on CRUD growth, but rather heat flux may be the most important factor. Further experiments would be needed to confirm this with better control over heat flux.

One area on the 6 μm tall micropost sample near one edge, shown in Figure 4-15, had particles that laid on top of the microposts and formed bridges between them, but had a clean surface underneath. Particles may have initially settled onto the surface in a way that promoted adhesion between particles on top of the microposts. Particles in the fluid would reach the particles on top of the micropost and adhere there rather than reaching the bottom of the surface. Due to the buildup of particles forming this top layer, a vapor film may have developed beneath it. This area of the sample may have experienced conditions of having a high local heat flux and higher temperatures due to the thermal resistance of the particles on the microposts. Bubbles usually move upward due to the buoyant force. However, fluid that evaporated underneath this umbrella of particles would be unable to escape vertically upward. Instead, they would be pushed to the sides before finding a place with no canopy of particles

blocking their path upwards to escape from. This may explain why there were no particles seen beneath areas with a top surface of particles, yet the areas next to them would have small particles both on top of the microposts and on the surface below. The vapor beneath the layer of particles on top pushes out any particles in its way as convection forces it outwards and upwards.

5.2 Effect of Heat Flux on CRUD Growth

The heat flux varied in each experiment despite using the same temperature setpoints and heating cycle times. The standard deviation of the heat flux was large, in part due to the low voltage output resulting in small level values recorded in the logomatic and in part due to the cycling of the heater. One of the 500 μm microcavity pitch sample had over twice as high of an average heat flux as the other 500 μm pitch sample (Table 3.2), and had slightly more CRUD but less large sediments on its surface. This agrees well with previous studies and industry experience that found higher heat flux resulted in more CRUD deposition due to increased subnucleate boiling [92, 7, 9]. One of the control samples that was boiled for 1 hour had a heat flux of 65.5 kW/m^2, which was over four times larger than the control sample it closely matched. It had larger sediments on its surface, but no noticeable changes in CRUD deposition.

The samples that experienced a temperature excursion would have experienced a much higher heat flux, which can cause a heat flux hysteresis effect. As wall superheat increases, the heat flux will increase along a certain path until the CHF is reached. However, when heat flux decreases, the path down the boiling curve may be different [50, 53]. Boiling sites may continue to stay active, so decreasing the heat flux will not necessarily decrease the temperature as much as expected. Boiling will continue to carry heat away efficiently below the original superheat needed to initiate boiling. Thus, samples that experienced a higher heat flux followed by a drop in heat flux may experience more boiling than samples that maintained a relatively constant heat flux.

The 30 μm microcavity pitch sample that experienced a temperature excursion up to 170°C had extensive CRUD growth (see Figure 4-7a), comparable to the 100 μm pitch samples. Even though the heat flux dropped back down to the sample temperature setpoint, the hysteresis effect could maintain more active boiling sites, resulting in a higher deposition rate. The average heat flux for this sample was 33.6 kW/m^2, which was double that of the other two 30 μm pitch samples.

The more interesting case is the 50 μm microcavity pitch sample that had a tem-

perature excursion up to 190°C. The average heat flux for this sample was 87.3 kW/m^2, which was almost four times the average heat flux of the other 50 μm pitch microcavity sample boiled under the same conditions. The maximum heat flux recorded was 238 kW/m^2, which was double the maximum heat flux of the 50 μm pitch microcavity sample in stable conditions. The sample that experienced the temperature excursion had very little CRUD growth and a distinct pattern of cleaner areas, shown in Figure 4-9b. The pattern can be explained by the bubble collapse mechanism mentioned earlier, and the cleaner surface, compared to other 50 μm pitch microcavity sample, can be explained by the higher heat flux. With a higher heat flux during the temperature excursion, combined with the hysteresis effect, the sample would have experienced more boiling during and after the excursion. Assuming the right conditions were present for the bubbles to collapse, the higher bubble nucleation rate would increase the chances of bubble collapse, leading to more frequent shockwaves that can push particles away from the nucleation sites. This would explain why we see a more distinct pattern of clean areas in the 50 μm pitch sample that experienced a temperature excursion. To really understand the effect of heat flux on CRUD growth in conjunction with induced microcavities or microposts, experiments must be carried out with more controlled heat fluxes.

5.3 Effect on Performance

The samples with lower pitch grids of microcavities showed the least amount of CRUD. Patterning fuel rods with grids of microcavities could limit the fouling layer that forms during a fuel cycle if the microcavity spacing is small enough and a condensation or cavitation effect can be produced. The bubble collapse that may have produced the modal phenomena observed in these experiments occurred around a threshold of 50 μm, though this may change in LWR conditions due to higher pressures, temperatures, heat flux, and fluid velocities. The sediments that are present on the samples in this experiment would likely not be an issue in a nuclear plant where the fuel rod is vertical and the coolant is circulating at a much higher velocity. Particles would be carried away by the coolant and filtered out by the purification system.

By decreasing the thickness or the amount of area covered by CRUD, the problems with higher corrosion rates, pressure drops, decreased heat transfer, activated products, and CIPS in nuclear plants will be mitigated. The microcavities could be made during the fuel rod fabrication process, such as by laser ablation, which can micromachine very hard materials [93]. Such self-cleaning fuel rods could reduce, or

get rid of altogether, the need for zinc injection or separate cleaning during reloading. If a pulsed ultrasound is still be required to induce the bubble collapse, having surfaces with regular arrays of microcavities would make cleaning easier. This self-cleaning mechanism could also be applied to other industries that suffer from fouling. Heat exchangers and other heated systems could be fabricated with regular arrays of microcavities that would promote cavitation.

Chapter 6

Conclusion

6.1 Key Results

The presence of induced defects, namely, systematic grids of microcavities and microposts, was found from this experiment to have potential for producing self-cleaning surfaces if optimized. The concept of induced defects was initially looked at for controlling vapor chimney formation in CRUD. However, what was observed instead was that the CRUD layer itself was more developed on some samples compared to others. In particular, microcavity pitch sizes of 50 μm and smaller under high heat flux conditions exhibited a modal pattern of clean and dirty areas. It was observed that the areas around the microcavities tended to be free of CRUD more often than not, indicating a force away from these induced defects.

Samples with microcavity pitches larger than 50 μm showed a trend of decreasing percentage of clean area and an increasing percentage of crudded area with increasing microcavity pitch. Samples that did not experience as much CRUD growth possessed larger sediments on their surfaces, perhaps due to agglomeration of the nickel and iron oxides in the coolant that settled out.

A thin ring of particles, less than a micrometer in width, was seen around most microcavities even when the surrounding areas were crudded, and it is suspected that the microcavities are where bubble nucleation preferentially occurs, and that CRUD deposition occurs near the edge of the bubble's attachment point to the surface.

The micropost samples experienced more CRUD growth than the control or microcavity samples, indicating they are not conducive to decrease fouling on heated surfaces. However, an interesting aspect was seen on one corner of a sample where an upper layer of CRUD formed on top of the microposts, but the surfaces directly underneath were kept clean. This may be due to vapor entrapment preventing deposition

in that area.

Using surface modification through induced microcavities could be a major development towards anti-fouling materials by creating self-cleaning surfaces. The applications of texturing heated surfaces with microcavities are numerous, from nuclear power plants to the food industry.

6.2 Future Work

The results of this experiment show a potential method for creating self-cleaning surfaces. To confirm the theory that nucleate boiling is promoted at microcavities, which then lead to the bubble collapse effect under the right conditions, a sample can be made that has a set of microcavities close together, but a large distance between the sets of microcavities. For example, rows of microcavities with horizontal pitches of 50 μm could be made with a vertical spacing of 1000 μm between each row. If the pattern of cleaner areas show up around the sets of microcavities, but a substantial amount of CRUD deposits fairly homogeneously between each set, it would prove that microcavities play a large role in where the modal pattern forms. Several different horizontal and vertical pitches can be used to determine the threshold for the cavitation effect. Long-term testing will determine the effectiveness of surface-texturing in preventing CRUD formation over time.

In order to verify the condensation or cavitation effect, several methods could be used. The local pressure could be controlled, for example by using oscillating acoustic waves. This is already done in cleaning applications. Condensation could be verified by decreasing the bulk coolant temperature. Optimizing this effect through the use of surface texturing and control of heat flux and local pressure could lead to many applications for anti-fouling surfaces. In addition, the micropost samples could be further examined to see if the phenomenon of cleaner surfaces under bridges of CRUD can be repeated and controlled. In this regard, it would also be beneficial to study whether the microposts help trap vapor.

These tests should be run under conditions as similar as possible to those experienced in LWRs. A test loop that can match the pressure, temperature, and flow conditions of a reactor could be used to examine CRUD growth over time. Zircaloy could replace silicon as the substrate material to observe the CRUD growth on actual cladding material and for examining the bonds between CRUD and Zircaloy. A vertical setup could be used to better match the configuration of fuel pins, and would also likely decrease sedimentation on the samples. Deaerating the coolant and using

actual H_3BO_3 and LiOH concentrations found in PWRs would result in a more accurate representation of the CRUD composition and precipitates in the porous layer that would be present in a PWR. Ideally, the bulk coolant temperature would stay in the subcooled region, but the sample vapor quality would be the same as a PWR during normal operations.

To examine the formation of vapor chimneys, sub-cooled boiling for longer will induce more CRUD growth, which will enable a more accurate measurement of vapor chimney size and density in the CRUD layer. Hydrophilic and hydrophobic surface modifications, which change the contact angle, could be examined for controlling vapor chimney formation or preventing CRUD growth.

For better control over the nucleate boiling conditions, the power to heater could be measured and a feedback loop could be used to control heating. A higher power would be needed to sustain film boiling. When this occurs, the power to the heater should be lowered to an appropriate level so that film boiling will be avoided but nucleate boiling continues.

Bibliography

[1] T.R. Bott. *Fouling of Heat Exchangers.* Elsevier, 1995. pp. 15-53.

[2] O.G. Palanna. *Engineering Chemistry.* Tata McGraw-Hill Education, 2009. pp. 291-294.

[3] S.N. Kazi. *Heat Exchangers - Basics Design Application*, chapter 19 Fouling and Fouling Mitigation on Heat Exchanger Surfaces, pages 507–532. 2012.

[4] R.V. Macbeth. Boiling on Surfaces Overlayed with a Porous Deposit: Heat Transfer Rates obtainable by Capillary Action. Atomic Energy Establishment, June 1971.

[5] D.A. Jones. *Principles and Prevention of Corrosion.* Macmillan, Inc., 1992.

[6] L.F. Melo, T.R. Bott, and C.A. Bernardo, editors. *Fouling Science and Technology.* NATO ASI, Series E. Kluwer Academic Publishers, 1988.

[7] J. Chen. On the Interaction between Fuel Crud and Water Chemistry in Nuclear Power Plants. Technical Report SKI Report 00:5, SKI, 2000.

[8] J.A. Sawicki. Analyses of fuel crud and coolant-borne corrosion products in normal water chemistry BWRs. *Journal of Nuclear Materials*, 419:85–96, 2011.

[9] IAEA. Review of Fuel Failures in Water Cooled Reactors. IAEA Nuclear Energy Series No. NF-T-2.1, 2010.

[10] A.T.R. Konings and A.T. Motta. *Comprehensive Nuclear Materials.* Elsevier, 2012.

[11] PWR Primary Water Chemistry Guidelines Committee. PWR Primary Water Chemistry Guidelines. Technical Report TR-105714, EPRI, 1999.

[12] I. Betova, M. Bojinov, P. Kinnunen, and T. Saario. Zn injection in Pressurized Water Reactors - laboratory tests, field experience and modelling. Technical Report VTT-R-05511-11, VTT, 2011.

[13] C. Pan. *Wick boiling in porous deposits with chimneys.* PhD thesis, University of Illinois at Urbana-Champaign, January 1986.

[14] J. Buongiorno. Can corrosion and CRUD actually improve safety margins in LWRs? *Annals of Nucleart Energy*, 63:9–21, JAN 2014.

[15] R. Adamson, F. Garzarolli, B. Cox, A. Strasser, and P. Rudling. Corrosion Mechanisms in Zirconium Alloys. Technical report, A.N.T. International, October 2007.

[16] Woods Hole Oceanographic Institution. Marine Fouling and Its Prevention, 1952.

[17] Environmental Laboratory. Environmental Laboratory, August 2014. http://el.erdc.usace.army.mil/.

[18] Conco Systems. South Texas Project Nuclear Power Plant Unit 1 Condenser, August 2014. http://www.concosystems.com/content/55.

[19] M.A. Kreider, G.A. White, and R.D. Varrin. A global fouling factor methomethod for analyzing steam generator thermal performance degradation. Technical report, Dominion Engineering, Inc., 1998.

[20] R.V. Macbeth. The effect of "Crud" deposits on frictional pressure drop in a boiling chimney. Technical Report AEEW-R767, Atomic Energy Establishment of Winfrith, 1972.

[21] G. Wang, W.A. Byers, M.Y. Young, J. Deshon, Z. Karoutas, and R.L Oelrich. Thermal Conductivity Measurements for Simulated PWR CRUD. In *ICONE21*, 2013.

[22] N. Cinosi, I. Haq, M. Bluck, and S. P. Walker. The effective thermal conductivity of crud and heat transfer from crud-coated PWR fuel. *Nuclear Engineering and Design*, 241(3):792–798, 2011.

[23] G. Wang, A. Byers, and M. Young. Simulated Fuel Crud Thermal Conductivity Measurements Under Pressurized Water Reactor Conditions. Technical Report 1022896, EPRI, 2011.

[24] L.S. Tong and Y.S. Tang. *Boiling Heat Transfer And Two-Phase Flow.* Taylor & Francis, 1997.

[25] MatWeb, July 2014. http://www.matweb.com/index.aspx.

[26] Special Metals, July 2014. http://www.specialmetals.com/home.php.

[27] CRC Handbook of Chemistry and Physics, July 2014. http://www.hbcpnetbase.com/.

[28] *Handbook of Stainless Steel.* Outokumpu, 2013. pp. 54-57.

[29] G. Wang. *Improved CRUD Heat Transfer Model for Dryout on Fuel Pin Surfaces at PWR Operating Conditions.* PhD thesis, Pennsylvania State University, 2009.

[30] J. Henshaw, J. McGurk, H. Sims, A. Tuson, and J. Dickinson, S. & Deshon. A model of chemistry and thermal hydraulics in PWR fuel crud deposits. *Journal of Nuclear Materials*, pages 1–11, 2006.

[31] S.C. Cheng, W.W.L Ng, and K.T. Heng. Measurements of boiling curves of subcooled water under forced convective conditions. *International Journal of Heat and Mass Transfer*, 21:1385–1392, 1978.

[32] C.C.V. Chan, P.R. Berube, and E.R. Hall. Relationship between types of surface shear stress profiles and membrane fouling. *Water Research*, 45:6403–6416, 2011.

[33] R. Sheikholeslami. Composite Fouling - Inorganic and Biological: A Review. *Environmental Progress*, 18:113–122, 1999.

[34] I.C. Escobar, E.M. Hoek, C.J. Gabelich, F.A. DiGiano, and Y.A.; et al. Le Gouellec. Committee report: recent advances and research needs in membrane fouling. *Journal - American Water Works Association*, 14:79–89, 2005.

[35] L.M. Gomes and A.L.A. Mesquita. On the prediction of pickup and saltation velocities in pneumatic conveying. *Brazilian Journal of Chemical Engineering*, 31, 2014.

[36] K.R. Goode, K. Asteriadou, P.T. Robbins, and P.J. Fryer. Fouling and Cleaning Studies in the Food and Beverage Industry Classified by Cleaning Type. *Food Science and Food Safety*, 12:121–143, 2013.

[37] V. Kochkodan, D.J. Johnson, and N. Hilal. Polymeric membranes: Surface modification for minimizing (bio)colloidal fouling. *Advances in Colloid and Interface Science*, 206:116–140, 2014.

[38] J. Gregory. *Particles in Water. Properties and Processes.* CRC Press, 2005.

[39] J. Gregory. Interaction of unequal double layers at constant charge. *Journal of Colloid and Interface Science*, 51:44–51, 1975.

[40] N.V. Churaev and B.V. Derjaguin. Inclusion of Structural Forces in the Theory of Stability of Colloids and Films. *Journal of Colloid and Interface Science*, 103:542–553, 1985.

[41] M.L; Zoeteweij, J.C.J. van der Donck;, and R. Versluis. Particle removal in linear shear flow: model prediction and experiental validation. TNO Science and Industry, July 2008.

[42] J.M. Hawkes. The Simulation and Study of Conditions Leading to Axial offset Anomaly in Pressurized Water Reactors. Master's thesis, Georgia Institute of Technology, December 2004.

[43] W. Wu and B.G. Jones. Simulation of bubble dynamics in sub-cooled boiling on fuel clad IN PWRS. In *Proceedings of ICONE10*, 2002.

[44] IAEA. Optimization of Water Chemistry to Ensure Reliable Water Reactor Fuel Performance at High Burnup and in Ageing Plant (FUWAC), 2011.

[45] W.A. Byers. Pressurized water reactor core crud mapping. In *Proceedings of the 18th International Conference on Nuclear Engineering*, 2010.

[46] E.J. Ruzauskas and R.A. Perkins. Fuel Surveillance at Dresden-2 After One Cycle of Noble Metal Chemical Application. Technical report, EPRI, 2002.

[47] Y. Solomon and J. Roesmer. Measurement of fuel element crud deposits in pressurized water reactors. *Nuclear Technology*, 29:166–173, 1976.

[48] P. Chen, W. Wu, and B. Jones. Investigation of surface microgeometry and the active nucleation cavities using AFM. *Nuclear Engineering and Design*, pages 2035–2041, 2009.

[49] V.P. Carey. *Liquid-vapor phase-change phenomena : an introduction to the thermophysics of vaporization and condensation processes in heat transfer equipmen.* Taylor and Francis, 2008.

[50] M. Poniewski and J. Thome. *Nucleate Boiling on Micro-Structured Surfaces.* Heat Transfer Research, Inc. (HTRI), 2008. Chapter 3 Enhancement of Boiling Heat Transfer: Techniques and Experimental Results.

[51] C. Jiabin, C. Zhenye, and L. Jifang. Boiling heat transfer on surfaces with artificial nucleation sites. *Journal of Chemical Industry and Engineering (China)*, 2:190–199, 1987.

[52] B. Shi, B.G. Jones, and C. Pan. Parametric study of boiling heat transfer in porous media, March 1996.

[53] B. Jones, J. McHale, and S. Garimella. The Influence of Surface Roughness on Nucleate Pool Boiling Heat Transfer. *Journal of Heat Transfer*, pages 1–14, 2009.

[54] P.L. Frattini, J. Blok, S. Chauffriat, J. Sawicki, and J. Riddle. Axial offset anomaly: coupling PWR primary chemistry with core design. *Nuclear Energy*, 32, 2001.

[55] A. Deligiannis. Comparative analysis of source term removal at Cook Nuclear Plant. Master's thesis, University of Illinois at Urbana-Champaign, 2009.

[56] A. Valero and C. Cortes. Ash fouling in coal-fired utility boilers. Monitoring and optimization of on-load cleaning. *Prog. Energy Combust. Sci.*, 22:189–200, 1996.

[57] W. Yuan and A.L. Zydney. Humic Acid Fouling during Ultrafiltration. *Environmental Science and Technology*, 34:5043–5050, 2000.

[58] I. ul Hag, N. Cinosi, M. Bluck, G. Hewitt, and S. Walker. Modelling heat transfer and dissolved species concentrations within PWR crud. *Nuclear Engineering and Design*, 241(1):155–162, 2011.

[59] A. Chanapai. ModModel of Crystallizatoin Fouling in Shell-and-Tube Heat Exchangers. Master's thesis, Imperial College London, 2010.

[60] W. Ebert and C.B. Panchal. Analysis of Exxon CCrud-oil-slip stream coking data. Technical report, Argonne National Laboratory, 1995.

[61] S. Dickinson, J. Henshaw, J.C. McGurk, and H.E. Sims. Modeling PWR Fuel Corrosion Product Deposition and Growth Process. Technical Report 1011743, EPRI, 2005.

[62] M.P. Short. Effects of Fluid Flow on 2D & 3D Coupled Microscale Simulations of Porous Boiling Deposits (CRUD) in PWRs, 2012.

[63] P. Bennett, B. Beverskog, and R. Suther. Halden In-Reactor Test to Exhibit PWR Axial Offset Anomaly. Technical report, EPRI, 2004.

[64] H. Heki, S. Komura, and E. Okamura. Ultrasonic cleaning method for tubes nuclear fuel assemblies and device therefor, September 23 1998. EP Patent 0,615,792.

[65] M. Andersson, K. Berntsson, P. Jonsson, and P. Gatenholm. Microtextured Sufraces: towards Macrofouling Resistant Coatings. *Biofouling*, 14:167–178, 1999.

[66] C.P. Dillon. Cleaning, pickling, and passivation of stainless steels. *Materials Performance*, 33:5, 1994.

[67] S.N. Kazi, G.G. Duffy, and X.D. Chen. Fouling and fouling mitigation on heated metal surfaces. *Desalination*, 288:126–134, 2012.

[68] H. O'Hanley, C. Coyle, J. Buongiorno, T. McKrell, L. Hu, M. Rubner, and R. Cohen. Separate effects of surface roughness, wettability, and porosity on the boiling critical heat flux. *Applied Physics Letters*, 103, 2013.

[69] C. Coyle, H. O'Hanley, B. Phillips, J. Buongiorno, and T. McKrell. Effects of hydrophobic surface patterning on boiling heat transfer and critical heat flux of water at atmospheric pressure. *Proceedings of the 2013 ASME Power Conference*, 2013.

[70] K. Natesan and R. Natarajan. Survey on Leaching of Coatings Used in Nuclear Power Plants: Letter Report. Technical report, Argonne National Laboratory, 2006.

[71] ASTM Subcommittee. *Manual on Maintenance Coatings for Nuclear Power Plants*. ASTM International, 1990. Chapter 7 Coating Materials.

[72] Y. Zhang, M. Ishimaru, V. Tamas, O. Takuji, C. Hardiman, H. Xue, Y. Katoh, S. Shannon, and W.J. Weber. Nanoscale engineering of radiation tolerant silicon carbide. *Physical Chemistry Chemical Physics*, 14:13429–13436, 2012.

[73] R.G. Munro and S.J. Dapkunas. Corrosion Characteristics of Silicon Carbide and Silicon Nitride. *Journal of Research of the National Institute of Standards and Technology*, 98:607–631, 1993.

[74] M. Kang. Effect of surface roughness on pool boiling heat transfer. *International Journal of Heat and Mass Transfer*, 43:4073–4085, 2000.

[75] L. Yan, Y.S. Li, and C.B. Xiang. Preparation of poly(vinylidene fluoride)(pvdf) ultrafiltration membrane modified by nano-sized alumina (Al2O3) and its antifouling research. *Polymer*, 7701-7706, 2005.

[76] W.A. Byers, D.V. Paramonov, M.B. Dzodzo, Z.E. Karoutas, and M.Y. Young. CRUD-resistant Nuclear Fuel Cladding, 2004.

[77] A.E. Bergles and M.C. Chyu. Characteristics of Nucleate Pool Boiling from Porous MetMetal Coatings. *Journal of Heat Transfer*, 104:279–285, 1982.

[78] H.J. Zhang and L. Chen. Pool boiling heat transfer on the sintered porous surfaces. In *Proceedings of the 4th Miami international symposium on multiphase transport particulate phenomena*, 1987.

[79] A.S. Toloei, V. Stoilov, and D.O. Northwood. A new approach to combating corrosion of metallic materials. *Applied Surface Science*, pages 242–247, 2013.

[80] C.A. Mack. *Field Guide to Optical Lithography.* SPIE Press, 2006.

[81] Omega. *C9000A Series Autotune Temperature Controller.*

[82] S. Skogestad. Probably the best simple PID tuning rules in the world. *Journal of Process Control*, 2001.

[83] M. Dunlap and J.E. Adaskaveg. Introduction to the Scanning Electron Microscope, 1997.

[84] R.D. Deslattes, E.G. Kessler Jr., P. Indelicato, L. de Billy, E. Lindroth, J. Anton, J.S. Coursey, D.J. Schwab, J. Chang, R. Sukumar, K. Olsen, and R.A. Dragoset. X-ray Transition Energies, July 2014. http://physics.nist.gov/XrayTrans.

[85] E. Samiei, M. Shams, M. Mahdi, R. Ebrahimi, and G. Ahmadi. Numerical Study on Surface Tension Effects on Cavitation Bubble Collapse in Spherical Acoustic and Nonspherical Rayleigh Collapse. In *7th International Conference on Multiphase Flow*, 2010.

[86] M. Chern, P. Hsu, Y. Cheng, P. Tseng, and C. Hu. Numerical Study on Cavitation Occurrence in Globe Valve. *Journal of Energy Engineering*, 139, 2013.

[87] R. Arndt. Cavitation in fluid machinery and hydraulic structures. *Ann. Rev. Fluid Mech.*, 13:273–328, 1981.

[88] V. Minsier and J. Proost. Shock wave emission upon spherical bubble collapse during cavitation-induced megasonic surface cleaning. *Ulstrasonics Sonochemistry*, 15:598–604, 2008.

[89] B. Kanegsberg and E. Kanegsberg, editors. *Handbook for Critical Cleaning: Cleaning agents and systems, Volume 2.* Taylor & Francis Group, 2011.

[90] L. Trefethen. Surface Tension in Fluid Mechanics. Encyclopaedia Britannica Educational Corp., 1967.

[91] R.P. Scardina. Water Treatment: Fundamentals and Practical Implications of Bubble Formation. Master's thesis, 2000.

[92] J. Deshon. PWR Axial Offset Anomaly (AOA) Guidelines, Revision 1. Technical report, EPRI, 2004.

[93] T. Chen and R.B. Darling. *Micromachining Techniques for Fabrication of Micro and nano-sizedo Structures.* InTech, 2012.

Appendix A

Code for Calculating Area of Clean Areas on Samples

```
function drawcirc
clc; % Clear the command window
close all; % Close all figures
imtool close all; % Close all imtool figures

% Read image file
imagename = input('Enter image file name: ','s');
Image=imread(imagename);
imshow(Image)

filename = input('Enter output file name: ','s');
fileID = fopen(filename,'w');

disp('Press Enter to continue');
cont = 1; % Continue asking for circles if 1
Diameter = [];
Points = [];
i = 0;
f = 0.071185; % Conversion factor for length into micrometers

hold on;
markerSize = 2; % Size of the center cross
lineWidth = 1; % Thickness of lines

function clickCenter
    try
        % Click on center of circle
        [xCenter, yCenter] = ginput(1);
        % Mark center
        a(i) = plot(xCenter, yCenter, 'r+', 'MarkerSize', markerSize, 'LineWidth',↙
lineWidth);
    catch
        clickCenter
        % Catch error with plotting
    end
end

function clickEdge
    try
        % Click on edge of circle
        [xEdge, yEdge] = ginput(1);
        % Calculate radius
        newRadius = sqrt((xEdge-xCenter)^2+(yEdge-yCenter)^2);
        % Draw circle
        center = [xCenter, yCenter];
        b(i) = viscircles(center,newRadius, 'EdgeColor', 'r');
    catch
       clickEdge
        % Catch error with viscircles if Enter is pressed again
    end
end

while cont == 1
    i=i+1;

    % Press Enter to continue each time to allow for moving around the image
```

```
    pause

    clickCenter % Call function clickCenter
    clickEdge % Call function clickEdge

    % Ask if circle should be kept
    message = sprintf('Continue?');
    button = questdlg(message, message, 'Yes', 'No', 'Delete', 'Yes');
    drawnow;    % Refresh screen to get rid of dialog box remnants.
    if strcmpi(button, 'Yes')
        Diameter(end+1) = 2*newRadius;
        newPoints = [xCenter,yCenter];
        Points = [Points; newPoints];
        % Add new circle's diameter and coordinates to arrays
    elseif strcmpi(button, 'No')
        Diameter(end+1) = 2*newRadius;
        newPoints = [xCenter,yCenter];
        Points = [Points; newPoints];
        cont = 0;
        % Add new circle's diameter and coordinates to arrays

    elseif strcmpi(button, 'Delete')
        delete(a(i));
        delete(b(i));
        % Delete center mark and circle on image
    end
%index = knnsearch(Points,Points,'K',2);

end

Diameter = Diameter*f; % Convert Diameter to microns
% Calculate area circled
Area = pi.*(Diameter/2).^2;
TotalArea = sum(Area);
% Calculate average diameter and the (sample) standard deviation
avgDiameter = mean(Diameter);
%stdDiameter = std(Diameter);
stdDiameter = std(Diameter,1);

% Print to output file
fprintf(fileID,'%13s\r\n','Diameter (um)');
fprintf(fileID,'%3.4f\r\n', Diameter);
fprintf(fileID,'\r\n%13s\r\n','Area (um)');
fprintf(fileID,'%5.4f\r\n',Area);
fprintf(fileID,'\r\n%16s \t %16s\r\n','avgDiameter (um)','stdDiameter (um)');
fprintf(fileID,'%3.4f \t %3.4f\r\n',avgDiameter,stdDiameter);
fprintf(fileID,'\r\n%14s\r\n','TotalArea (um)');
fprintf(fileID,'%5.4f\r\n',TotalArea);
fclose(fileID);

end
```